ORNL-6500

ornl

OAK RIDGE NATIONAL LABORATORY

MARTIN MARIETTA

# Experimental and Analytical Evaluation of Weldment Creep Strength Reduction Factors for Elevated-Temperature Structural Design

J. M. Corum
R. L. Battiste
W. R. Hendrich
Y. L. Lin
R. W. Swindeman





OPERATED BY
MARTIN MARIETTA ENERGY SYSTEMS, INC.
FOR THE UNITED STATES
DEPARTMENT OF ENERGY

Printed in the United States of America
Available from the U.S. Department of Energy
Office of Scientific and Technical Information
P.O. Box 62, Oak Ridge, Tennessee 37830

## DISCLAIMER

**APPLIED TECHNOLOGY**



ORNL-6500
Dist. Category UC-538T
and 540T

Engineering Technology Division

# EXPERIMENTAL AND ANALYTICAL EVALUATION OF WELDMENT CREEP STRENGTH REDUCTION FACTORS FOR ELEVATED-TEMPERATURE STRUCTURAL DESIGN

J. M. Corum
R. L. Battiste Y. L. Lin
W. R. Hendrich R. W. Swindeman

Date Published: September 1988



Prepared by
OAK RIDGE NATIONAL LABORATORY
Oak Ridge, Tennessee 37831
operated by
MARTIN MARIETTA ENERGY SYSTEMS, INC.
for the
U.S. DEPARTMENT OF ENERGY
under Contract No. DE-AC05-840R21400

CONTENTS

# EXPERIMENTAL AND ANALYTICAL EVALUATION OF WELDMENT CREEP STRENGTH REDUCTION FACTORS FOR ELEVATED-TEMPERATURE STRUCTURAL DESIGN

J. M. Corum
R. L. Battiste Y. L. Lin
W. R. Hendrich R. W. Swindeman

## ABSTRACT

The long-term creep-rupture and fatigue strength of liquid-metal reactor plant components operating at elevated temperatures is a major concern of structural designers, plant regulators, and design code bodies. Because of this concern, new explicit weldment strength criteria in the form of creep and fatigue strength-reduction factors were recently introduced into the American Society of Mechanical Engineers Code Case N-47, which governs the design of elevated-temperature nuclear plant components in the United States. This report provides some of the background and logic for these factors and their use, and it describes the results of a series of four long-term creep-rupture tests of simple welded structures and the associated inelastic failure analyses. The structures (welded plates and cylinders) were made of 316 stainless steel base metal and 16-8-2 weld filler metal. The mechanical properties of the various zones of the weldments were well characterized and used in the analyses. Comparisons of the analytical predictions with the test results showed reasonable agreement, thus adding to an understanding of the nature and cause of creep-rupture failure in weldments. Overall, the results provide further substantiation of the validity of the strength-reduction factor approach for ensuring adequate life in elevated-temperature nuclear component weldments.

---

## 1. INTRODUCTION

The structural integrity of weldments in elevated-temperature construction has long been a concern, particularly for nuclear components where a higher level of life assurance is required and the service life is long. Yet until 1987, the *American Society of Mechanical Engineers (ASME) Boiler and Pressure Vessel Code Case N-47*, which governs construction of elevated-temperature Class 1 nuclear components, contained only minimal weldment design guidance based on actual weldment properties. In 1987, efforts of the Code groups and the Department of Energy (DOE)

advanced reactor materials and structures programs resulted in including weld creep-strength and fatigue-strength-reduction factors in Case N-47-26.[1] These factors significantly improve the overall elevated-temperature design methodology for welded components.

Actual plant experience has shown that the concern for the structural integrity of welded components subjected to elevated-temperature service is well founded. Thermal fatigue has led to weldment cracking in a number of liquid-metal reactor components. For example, the French Phenix liquid-metal fast breeder reactor (LMFBR), although extremely successful overall, was initially plagued with several problems of weldment cracking.[2,3] These problems included cracking at welds joining piping tees and valves to piping runs and cracking in intermediate heat exchanger welds. In each case, the cause was identified as fatigue or creep-fatigue resulting from the repeated thermal transient loadings. It has been stated that these problems "cost the power station many months of unavailability, and constituted a considerable loss of earning power."[3] A second example is the British Dounreay Fast Reactor (DFR), which developed a leak in a primary circuit pipe weld.[4] The stated cause was fatigue, and, again, the reactor had to be shut down for repairs. Liquid-metal reactors in the Soviet Union have reportedly also experienced weldment failures. Recently, elevated-temperature failures have begun to occur in some fossil plant welded pipe. These have appeared after many years of elevated-temperature operation and have been associated with creep rupture.

Although lessons regarding such things as weld placement, composition, and procedures were learned from these incidents, the need for explicit, experimentally based design rules is clear. The Nuclear Regulatory Commission (NRC) recognized this deficiency during the licensing review of the Clinch River Breeder Reactor Plant (CRBRP) for a construction permit.[5] Early weldment cracking, particularly in components subjected to repeated thermal transient loadings, was identified by the NRC as the foremost structural integrity concern, and a confirmatory test program was to have been required to determine the safety margins of weldments in elevated-temperature components.[6]

The design factors recently introduced into Case N-47 should help to allay the NRC concerns. Furthermore, recently completed creep-rupture and fatigue tests of welded structures at Oak Ridge National Laboratory (ORNL) add to the understanding of the behavior of welded structures and provide further substantiation of the validity of the weldment strength-reduction factors adopted by the *ASME Code*. Completion of planned thermal ratchetting failure tests of welded pipe at DOE's Energy Technology Engineering Center (ETEC) will provide more prototypic test data for confirming the validity of the design factors.

This report, which is a companion to a similar report covering weldment fatigue design rules and tests,[7] provides some of the background, logic, and experimental validation of the Code creep-rupture strength-reduction factors that are used in both the primary stress limits and creep-fatigue rules of Case N-47. The report details creep-rupture failure tests and the inelastic failure analyses of four well-characterized structural weldment specimens (see Fig. 1). These specimens were fabricated from the DOE reference heat of 316 stainless steel and 16-8-2 stainless steel filler metal.* Two tests of axially welded flat plate specimens (at two different axial stress levels) and two tests of circumferentially welded pipe, or tube, specimens (again at two different axial stress levels) were performed. The tests were designed to examine (1) the maximum principal stress oriented parallel to the weld and (2) the maximum principal stress oriented perpendicular to the weld. The resulting test data were compared with (1) the inelastic failure analysis results to provide a better understanding of weldment creep failures and (2) the Code allowable stresses and weldment strength-reduction factors to provide additional validation of the Code design rules.

Chapter 2 of this report describes the background and logic of the Code creep-rupture factors, and it summarizes the body of structural weldment creep-rupture tests (as contrasted with the weld metal creep-rupture test data on which the factors are based) used to substantiate the validity of the design approach using the factors. These include

*This material combination was chosen because it is a prime candidate for the primary system components of liquid-metal reactors.

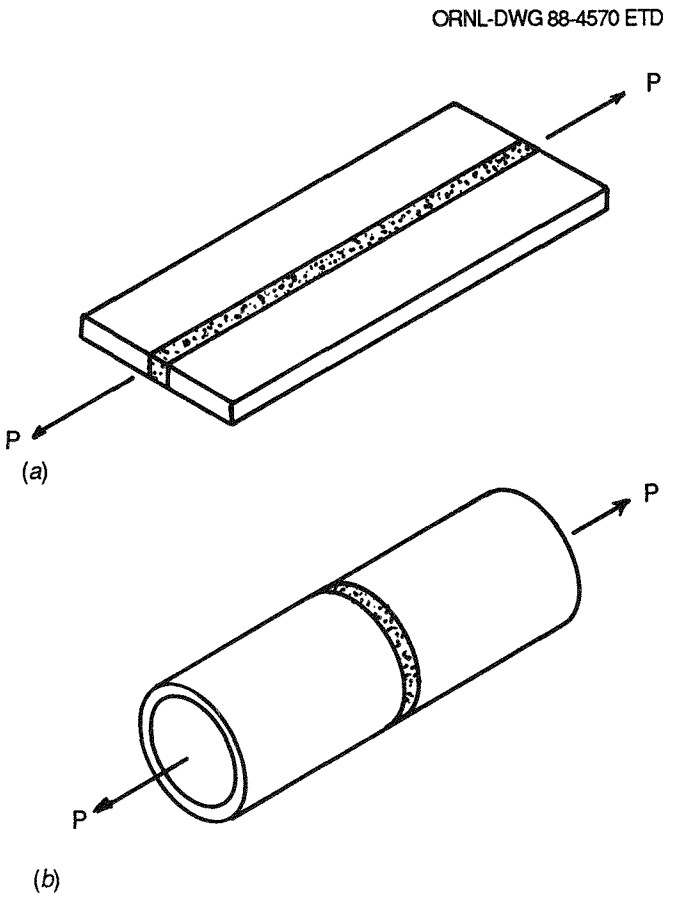


Fig. 1. Structural weldment types used in creep-rupture tests.

DOE-funded tests previously performed at ORNL on plates and cylinders of 304 stainless steel welded with 308 weld metal as well as DOE-funded tests on similar plates performed by the Westinghouse Advanced Reactors Division.

Chapter 3 describes the four 316/16-8-2 weldment specimens and the test program. The inelastic failure analyses, including the weldment mechanical properties data and the constitutive and failure models used, are described in Chap. 4. Chapter 5 summarizes the test results, and they are compared with the analytical predictions in Chap. 6. Finally, Chap. 7 contains a brief summary of what was done and why, and it lists conclusions relative to weldment behavior and the Code design rules.

## 2. BACKGROUND OF WELDMENT BEHAVIOR AND CREEP-RUPTURE FACTORS

It will be instructional to begin this discussion with a consideration of the variation of properties that can occur through a weldment [from the deposited weld metal (W) through the fusion line (FL) and heat-affected zone (HAZ) to the unaffected base metal (BM)]. Figure 2 depicts a typical multipass weldment and schematically shows the kind of property variations that can occur. Although the initial tensile yield stress of as-deposited W is usually about twice that of annealed BM in stainless and ferritic steels, the relative creep strengths depend more strongly on the heat-to-heat variations that exist in W and BMs. In the example shown, the W creep-rupture strength is significantly below that of the BM. With different heats of base and weld materials, the strength might be more nearly equal, or the W might even be stronger. With 316 stainless steel BM welded with 16-8-2 W, the average ratio of W creep-rupture

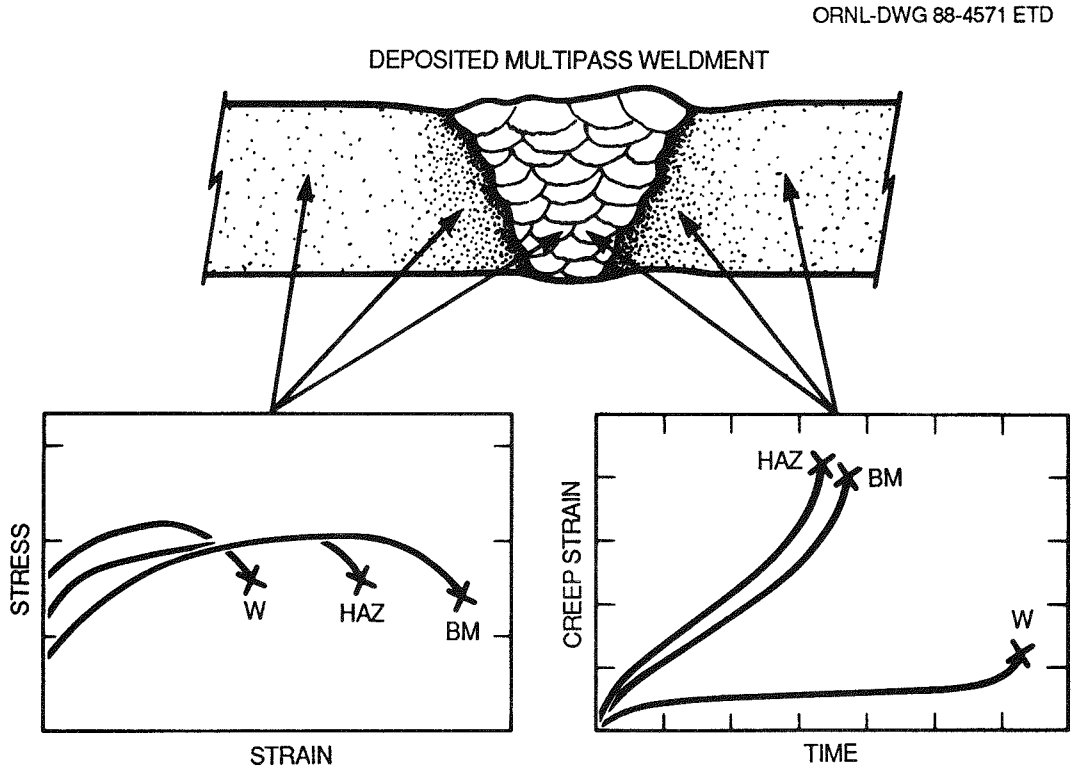


Fig. 2. Typical variation of tensile and creep properties through a weldment.

strength to base metal creep-rupture strength varies between 0.91 and 0.97 at 593°C (1100°F), depending on the rupture time.

The key point is that because of the variation in both deformation and failure properties, the creep-rupture strength of a weldment does not depend just on the creep-rupture strengths of the constituent materials. Consider, as an example, the axially stressed flat plate with an axial weld in Fig. 1. If the plate is initially loaded beyond the yield strength of the base metal, the stress in the weld metal will be higher than in the base metal, and the weld metal should therefore fail first, even if it has the same rupture strength as the base metal. On the other hand, if a lower initial load, below yield, is applied to the plate and the weld creeps more than the HAZ and base material, then the stress in the weld will reduce with time whereas that in the surrounding HAZ will increase. Even if the creep-rupture strengths are all equal, the HAZ material should experience early failure.

Considering the complexity of weldment behavior and the strong influence of relative material variability, the ASME high-temperature code groups concluded that adequate weldment life can best be ensured through the basic safety margins on allowable stress and the use of simple weld strength-reduction factors. In Case N-47, the primary time- and temperature-dependent stress limit $S_t$ is less than or equal to 2/3 $\sigma_{rmin}$, where $\sigma_{rmin}$ is the expected minimum creep-rupture strength of the base metal. At weldments, the allowable stress limit $S_t$ is specified to be the lower of the tabulated values for the base metal or 0.8 $\sigma_{rmin} \times R$, where R is the appropriate ratio of the weld metal creep-rupture strength to the base metal creep-rupture strength.

The appropriate R values for the various allowable weld filler metal/base metal combinations are listed in tables in Case N-47. As an example, the R factor table for 316 stainless steel welded with 16-8-2 filler metal is reproduced below. For that example, the factors remain relatively high over the entire time-temperature range. For another example, however, the factors for 316 welded with 316 drop below 0.5 for the higher temperatures and longer times.

**TABLE I-14.10 B-2 STRESS RUPTURE FACTORS FOR TYPE 316 STAINLESS STEEL WELDED WITH SFA 5.22 EXXXT-G (16-8-2 CHEMISTRY); SFA 5.4 E 16-8-2; AND SFA 5.9 ER 16-8-2**

| Temp °F | 10 hr | 30 hr | 100 hr | 300 hr | 1000 hr | 3000 hr | 10,000 hr | 30,000 hr | 100,000 hr | 300,000 hr |
|---|---|---|---|---|---|---|---|---|---|---|
| 850 | 1.00 | 0.96 | 0.91 | 0.91 | 0.91 | 0.90 | 0.89 | 0.88 | 0.87 | 0.86 |
| 900 | 1.00 | 0.94 | 0.88 | 0.82 | 0.81 | 0.80 | 0.77 | 0.76 | 0.74 | 0.72 |
| 950 | 1.00 | 0.93 | 0.86 | 0.86 | 0.85 | 0.83 | 0.83 | 0.81 | 0.79 | 0.78 |
| 1000 | 1.00 | 0.93 | 0.90 | 0.90 | 0.90 | 0.89 | 0.87 | 0.87 | 0.85 | 0.85 |
| 1050 | 0.92 | 0.92 | 0.92 | 0.92 | 0.92 | 0.92 | 0.92 | 0.93 | 0.90 | 0.86 |
| 1100 | 0.91 | 0.91 | 0.93 | 0.94 | 0.94 | 0.96 | 0.96 | 0.96 | 0.97 | 0.96 |
| 1150 | 0.91 | 0.91 | 0.93 | 0.95 | 0.95 | 0.96 | 0.98 | 0.99 | 0.99 | 1.00 |
| 1200 | 0.89 | 0.89 | 0.90 | 0.92 | 0.93 | 0.97 | 0.99 | 1.00 | 1.00 | 1.00 |

Note: $°C = (°F - 32) \times 0.5556$

*Source*: Case N-47-26, *Class 1 Components in Elevated Temperature Service, Section III, Division 1*, Cases of ASME Boiler and Pressure Vessel Code, American Society of Mechanical Engineers, New York, February 1987.

To help determine the Code's rules on weldment design rules, the DOE High-Temperature Structural Design Program at ORNL carried out an analytical parameter study based on consideration of the relative variability of weld- and base-metal properties.[8] The goal was to provide insight into the stress, strain, and failure behavior of weldments and to provide guidance on the use of creep-rupture strength-reduction ratios for primary stress limits, which is the approach subsequently written into the Code. The parameter study consisted of numerous inelastic failure analyses of the two welded geometries that were shown in Fig. 1 (an axially welded flat plate and a circumferentially welded tube). Average properties of 304 stainless steel were used for the base metal. For the weld metal, the yield strength varied from a factor of 0.75 to 2.0 times the base metal yield; the creep rate varied by a factor of 0.05 to 20.0 times the base metal rate; and the creep-rupture strength (stress) varied from 0.65 to 1.55 that of the base metal value. These are realistic, expected ranges. In addition to numerous analyses with varying weld metal properties, the effect of weld thickness was investigated using the tube model. Supplemental analyses were also performed to examine the effects of stress state, stress level, and cyclic loading conditions in conjunction with property variations.

When compared with the all-base-metal structure results, variations of weld properties generally caused degradation of deformation and failure behavior either in the weld metal or in the base metal adjacent to

the weld interface. Also, increasing weld thickness resulted in reduced weld strength. But the most important finding was that the calculated strength-reduction factors were reasonably consistent with the R values now in Case N-47, even though the latter are simply the ratio of uniaxial weld metal creep-rupture strength to base metal strength.

Further substantiation of the overall adequacy of the Code limits came from an ORNL compilation and examination of the results of creep-rupture tests of structural weldments. Data for three of the basic Case N-47 materials were collected: 304 and 316 stainless steels and 2 1/4 Cr-1 Mo steel. In addition to welded plate and tube tests performed at ORNL[9-11] and welded plate tests performed at Westinghouse,[12,13] data in the open literature from Sweden,[14] the United Kingdom,[15] and Japan[16] were used, as were some foreign exchange data that, because of agreements, cannot be referenced here. Altogether, 40 pertinent structural weldment creep-rupture test results were located and assessed. The various specimen types employed are depicted in Fig. 3. Key points regarding these

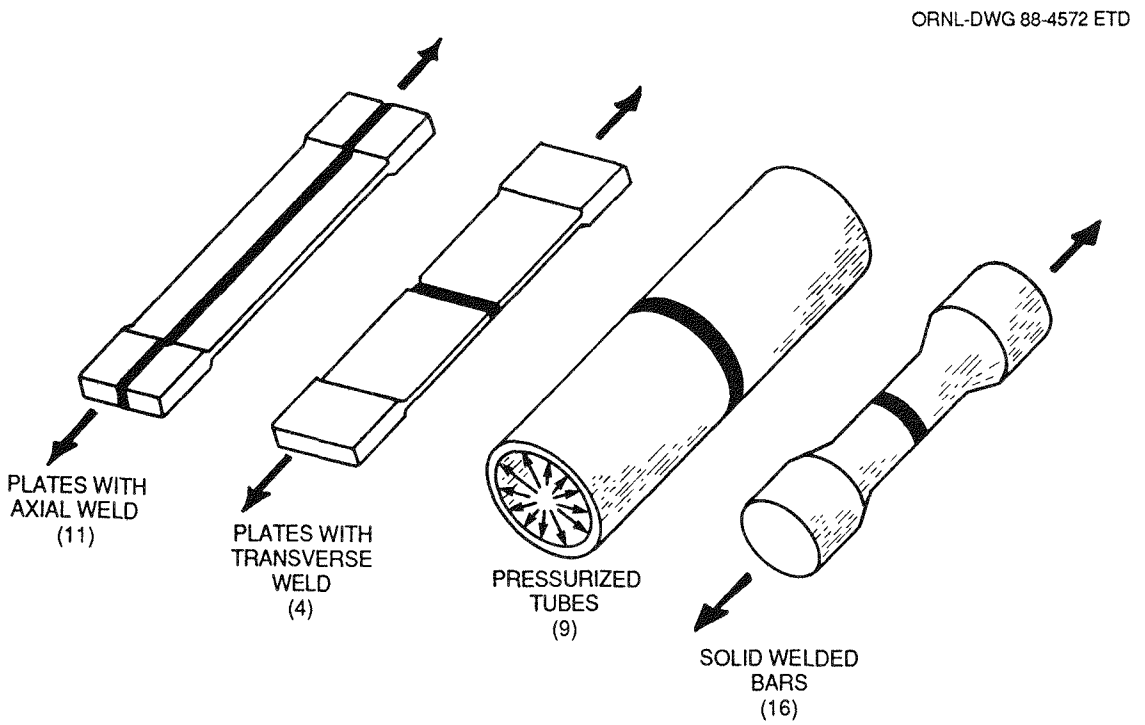


Fig. 3. Test specimens and loadings used in creep-rupture tests of structural weldments. The numbers in parentheses are the numbers of the various tests.

tests are listed below:

- three base metals are represented,
- the specimens were designed specifically to provide a variety of stress states and to capture behavioral features of weldments,
- several prototypic weld metals and processes were used,
- both as-welded and postweld heat-treated specimens were tested, and
- the test temperatures ranged from 510 to 600°C (950 to 1112°F).

The structural weldment test results were compared with the Code Case N-47 expected minimum creep-rupture strengths of the corresponding base metals, and the results are plotted two different ways in Figs. 4 and 5. Figure 4 shows the ratio of the measured structural weldment creep-rupture time to the N-47 minimum time to rupture. The base metal minimum stress to rupture appears to be the lower bound of the weldment data, and the margin between the data and this lower bound increases with increasing rupture life. The same trend is exhibited in Fig. 5, in which the ratio of the measured stress to rupture to the minimum expected base metal creep-rupture strength is shown.

These results are encouraging. However, the data points plotted in Figs. 4 and 5 represent complete specimen rupture, whereas the Code rules are intended to guard against cracking. The plate weldment creep-rupture tests performed at Westinghouse provide some insight into initial cracking vs complete rupture. Figure 6 shows results for plates with both axial and transverse welds. The base material in these tests was 304 stainless steel, and the weld metal was 308 stainless steel with controlled residual elements (CREs). For these results, the nominal stress to produce initial cracking appears to be about 90% of that to produce rupture in a given time. For other structural configurations and materials, this factor could be different. However, it was concluded by the Code groups that the Case N-47 $S_t$ allowable based on two-thirds of the expected minimum base metal creep-rupture strength, together with the R factors to account for lower weld metal creep-rupture strength, are adequate to guard against weldment cracking without excessively eroding the ability of the design margin to cover other uncertainties.

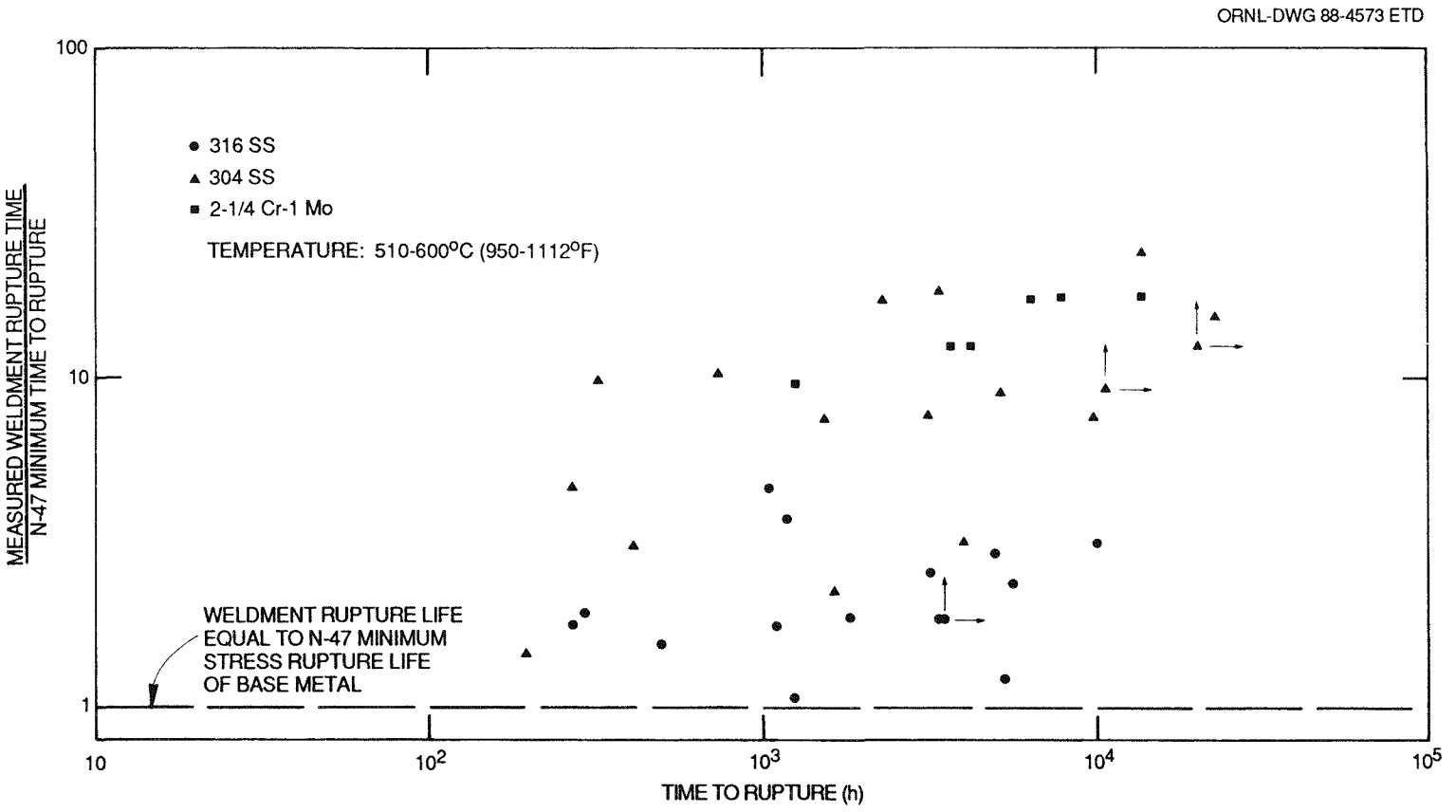


Fig. 4. Comparison of structural weldment test results with expected minimum time to rupture of base metal.

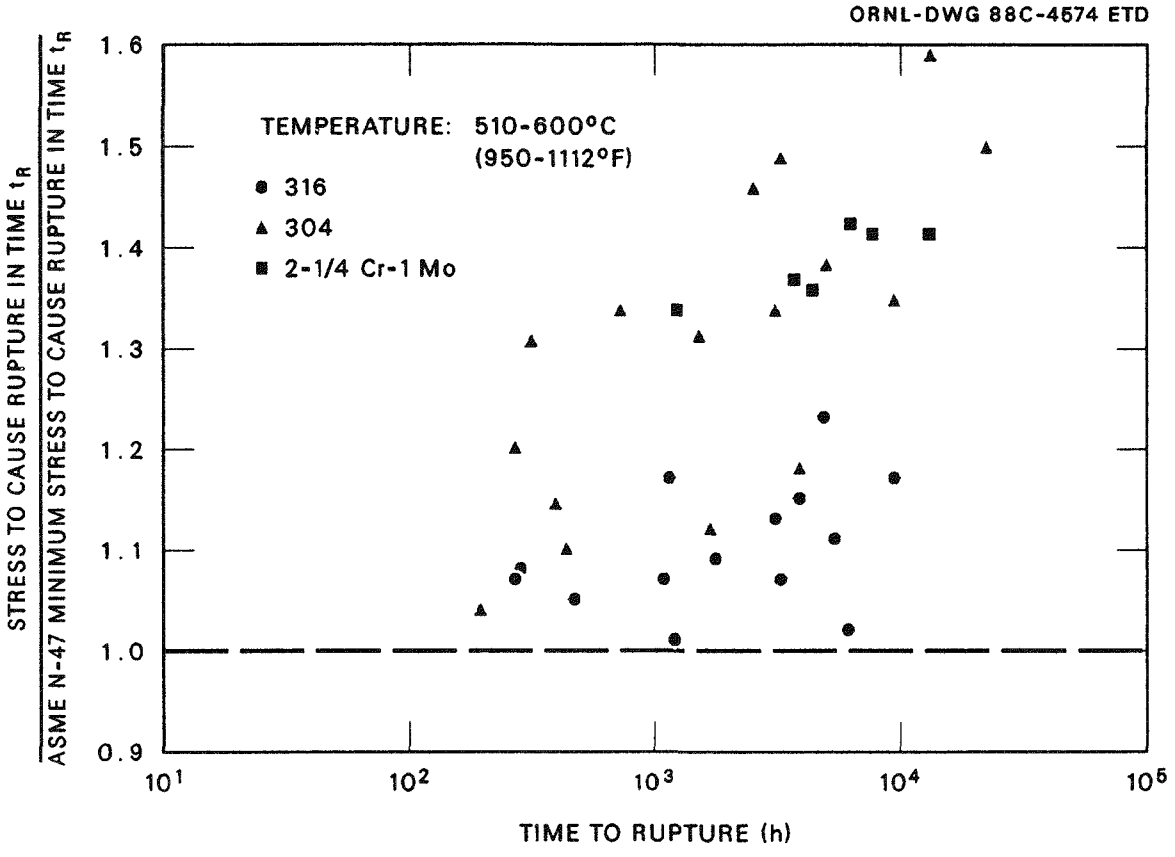


Fig. 5. Comparison of structural weldment test results with expected minimum stress to rupture of base metal.

These conclusions are based on limited data. The purpose of the four tests described in the subsequent chapters of this report was to obtain additional data, including material characterization and analysis results, from carefully performed tests on the weldment — 316 stainless steel welded with 16-8-2 filler metal — of most current interest concerning liquid-metal reactors. The carefully obtained data and analysis predictions that will be described in subsequent chapters strengthens the understanding of weldment creep-rupture behavior and the adequacy of the Code factors discussed in this chapter.

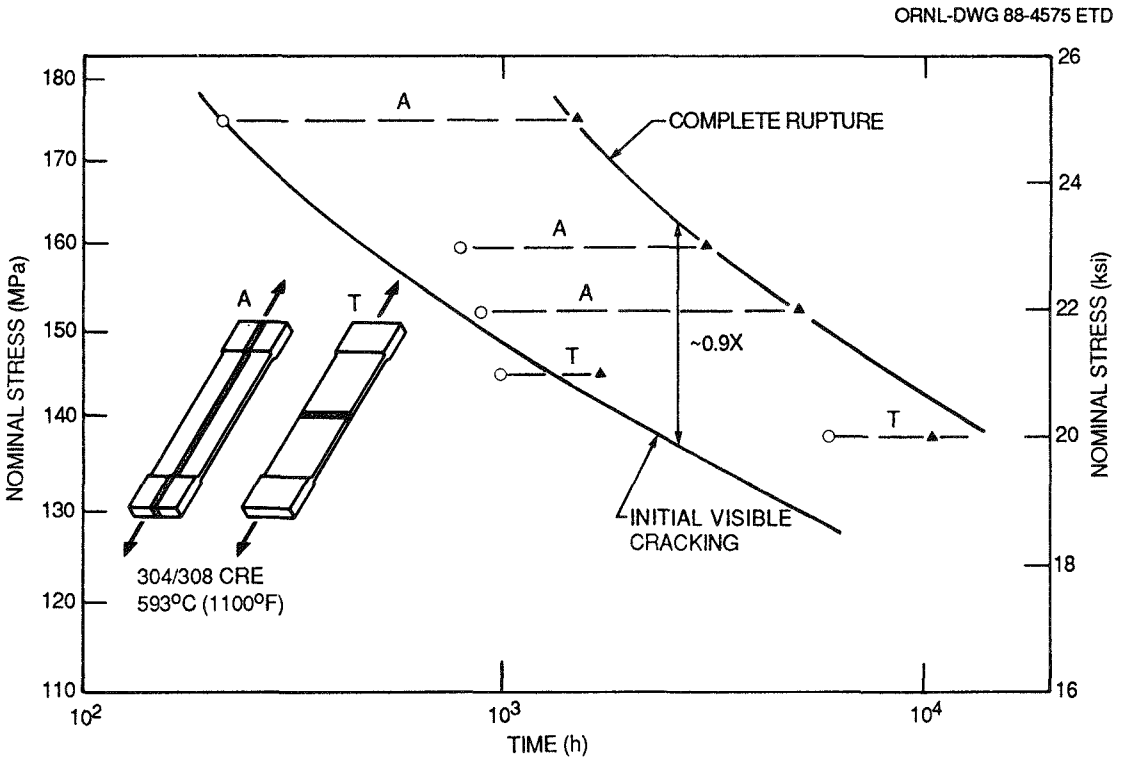


Fig. 6. Comparison of initial cracking with complete rupture for plate weldment tests performed at Westinghouse.[12,13]

# 3. DESCRIPTION OF SPECIMENS AND TEST PROGRAM

## 3.1 Overview

The creep-rupture tests were performed on axially loaded specimens of two types: (1) axially welded plates and (2) circumferentially welded pipes. The plate geometry was selected to achieve a weldment test in which the maximum principal stress is parallel to the weld. In the plate, the weld- and base-metal components are in parallel and are thus subjected to different axial stresses, depending on the variation and interaction of the properties of the component materials. The pipe geometry, while being a realistic structure, was not intended to represent any particular component feature other than one in which the principal stress is normal to the weld. This geometry was selected primarily for simplicity of concept, fabrication, and analytical modeling. In the pipe, the weld- and base-metal components are in series and are thus subjected to the same nominal axial stress. The behavior of the pipe reflected the properties of the individual components (base and weld metal), with the interaction being confined to a narrow zone where a mismatch of properties caused distortion in the deformation field.

Four structural weldment creep failure tests, two plates and two pipe tests, were performed (see Fig. 7). The welded plate creep test 5 (WPCT-5) was conducted at a constant stress of 221 MPa (32 ksi). The welded plate creep test 7 (WPCT-7) involved a step change in stress from 152 MPa (22 ksi) to 171 MPa (24.8 ksi) at 4400 h into the test. The creep-rupture stress levels for the welded cylinder creep tests 1 and 2 (WCCT-1 and -2) were 221 MPa (32 ksi) and 193 MPa (28 ksi), respectively. The test temperature for all four tests was 566°C (1050°F).

All four test specimens were fabricated from 316 stainless steel base metal (reference heat 8092297) with 1.02-mm-diam (0.04-in.) 16-8-2 filler metal wire (Arcos Corporation heat Y3018R). Either the normal gas tungsten arc process or the hot wire gas tungsten arc process was used to prepare the various weldments. The base metal for all four structures was solution annealed before welding. No further heat-treatment was performed after welding; thus, the structures were tested with the weld metal in the as-deposited condition.

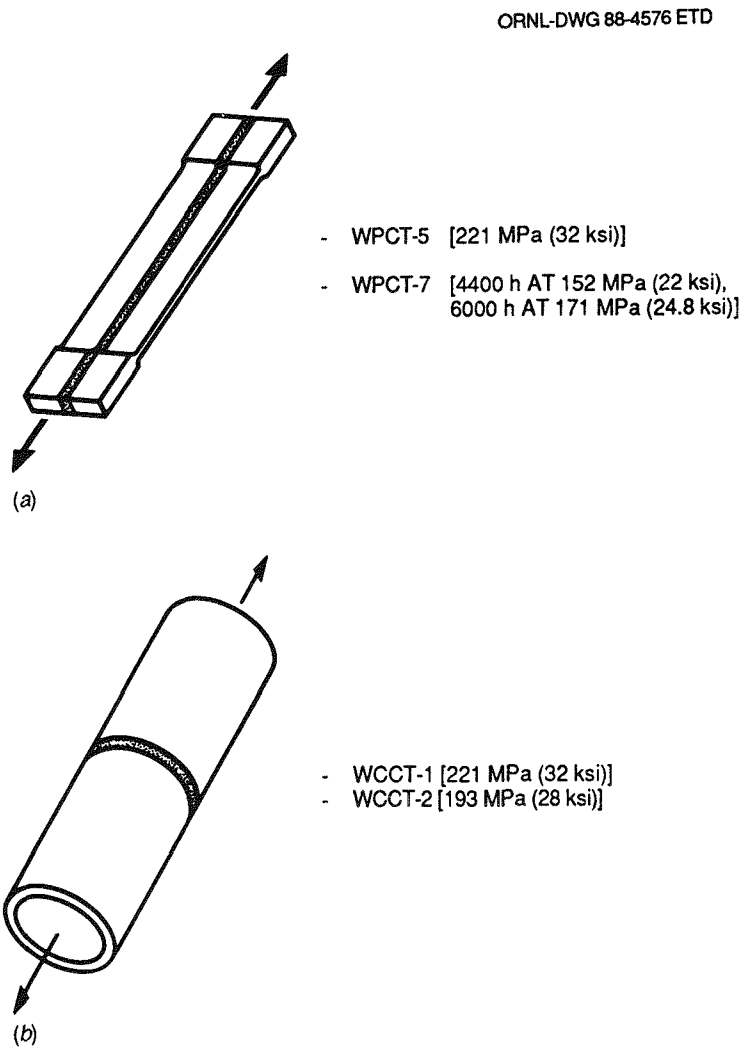


Fig. 7. Four failure tests of 316/16-8-2 structural weldments.

## 3.2 Specimen Descriptions

The flat-plate weld blanks for the WPCT-5 and -7 specimens were fabricated using 25.4-mm (1-in.) 316 stainless steel plate, reference heat 8092297 (see Fig. 8). The base metal blanks were solution annealed before welding by heating to 1093°C (2000°F) in an inert atmosphere at a heating rate of ~256°C/h (460°F/h), held at 1093°C for 1 h, then rapid cooled to below 593°C (1100°F) with forced air cooling. The plate base metal blanks were then machined with square sides, and a backing plate was used to start the weld so that the deposited weld had a nominally rectangular cross section. Realistically, the weld was not a perfect

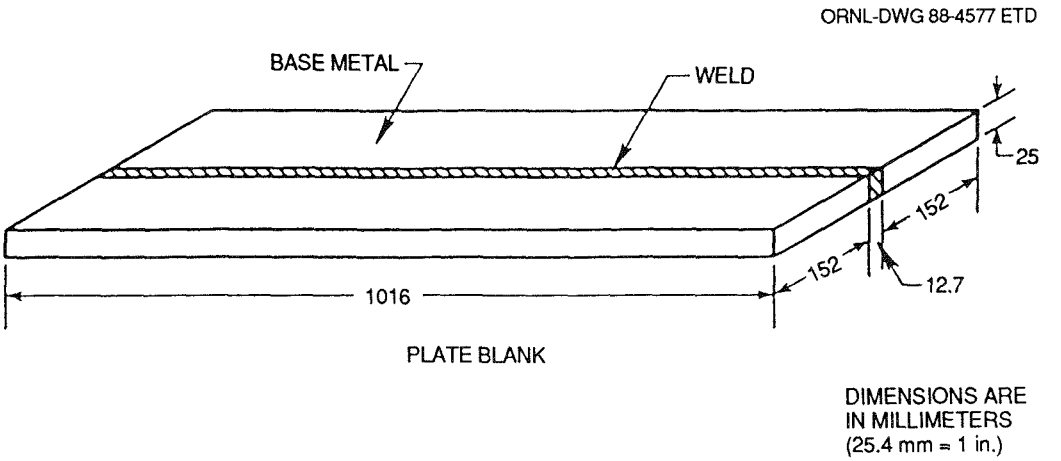


Fig. 8. Weld blank configurations for flat-plate weldment specimens (25.4 mm = 1 in.).

rectangle but approximated one closely enough for the purpose of analysis. Following manual root passes, the 16-8-2 weld material was machine deposited using the hot wire gas tungsten arc process. The average heat input was ~3,300 kJ/mm (84,000 kJ/in.).

Figure 9 shows a photograph of the finish machined WPCT-5 specimen. The overall specimen length and width were 749 mm (29.5 in.) and 178 mm (7 in.), respectively. The grip end thickness was 19 mm (0.75 in.). The gage length was 152 mm (6 in.). The gage width and thickness were 101.6 mm (4.0 in.) and 9.53 mm (0.375 in.) respectively. The specimen was machined using the center of the weld as the reference axial centerline of the specimen. The surface finish within the gage length was 1.6 μm (63 μin.) or better.

The geometry of the WPCT-7 specimen is shown in Fig. 10. The specimen was similar to WPCT-5. The thickness was 9.53 mm (0.375 in.) over the entire specimen, and the width was 101.6 mm (4 in.) in the reduced area gage length. The specimen failed in the grips after 4400 h of testing at 152 MPa (22 ksi). New improved grips were then electron-beam-welded to the specimen. The specimen was then remachined to 6.35 mm (0.25 in.) thick and 76.23 mm (3 in.) wide in the gage length. The machining eliminated any surface cracks that might have formed in the first phase of testing.

ORNL PHOTO 7628-81

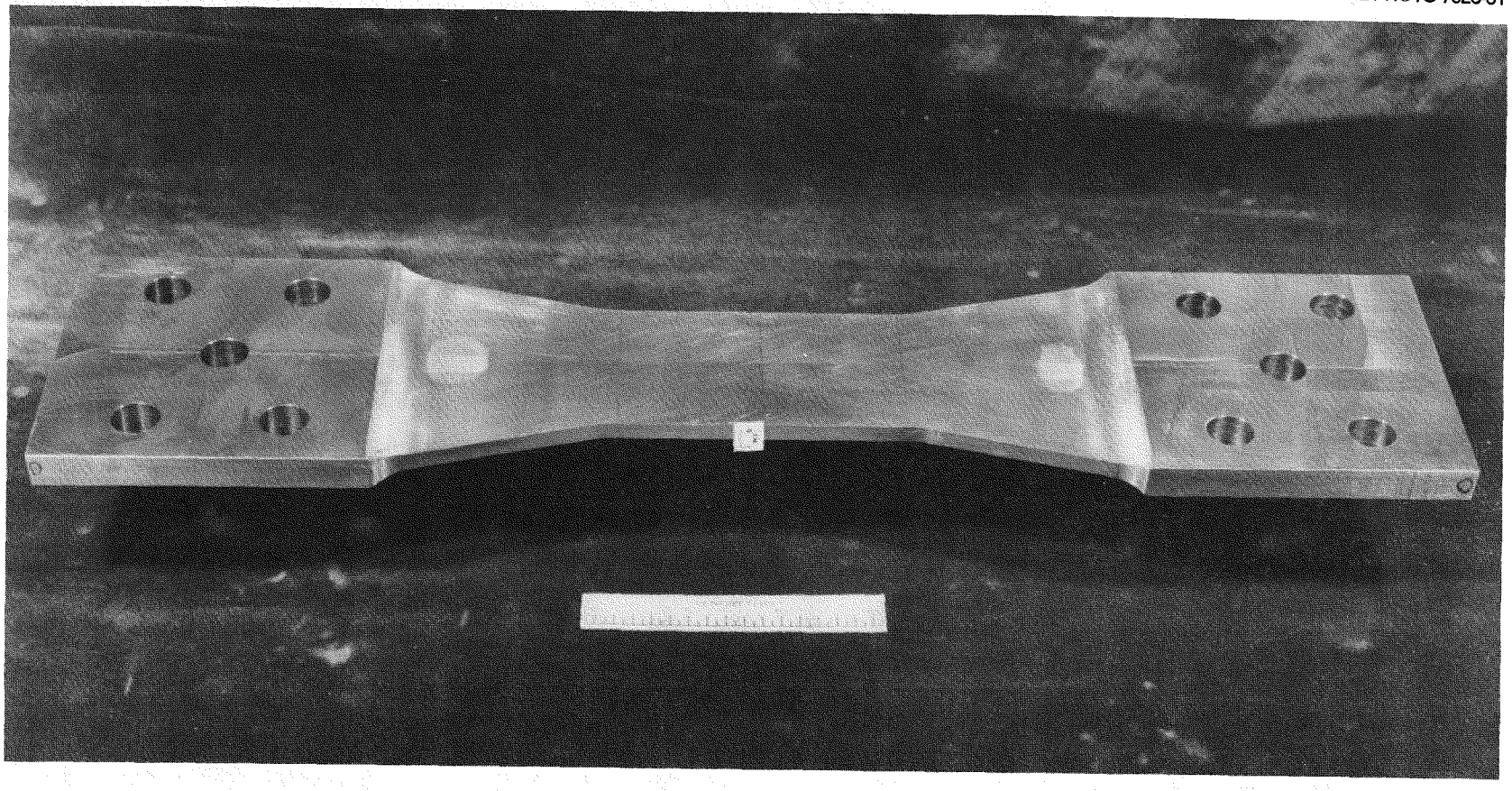

Fig. 9. Photograph of the welded plate creep test specimen (WPCT-5).

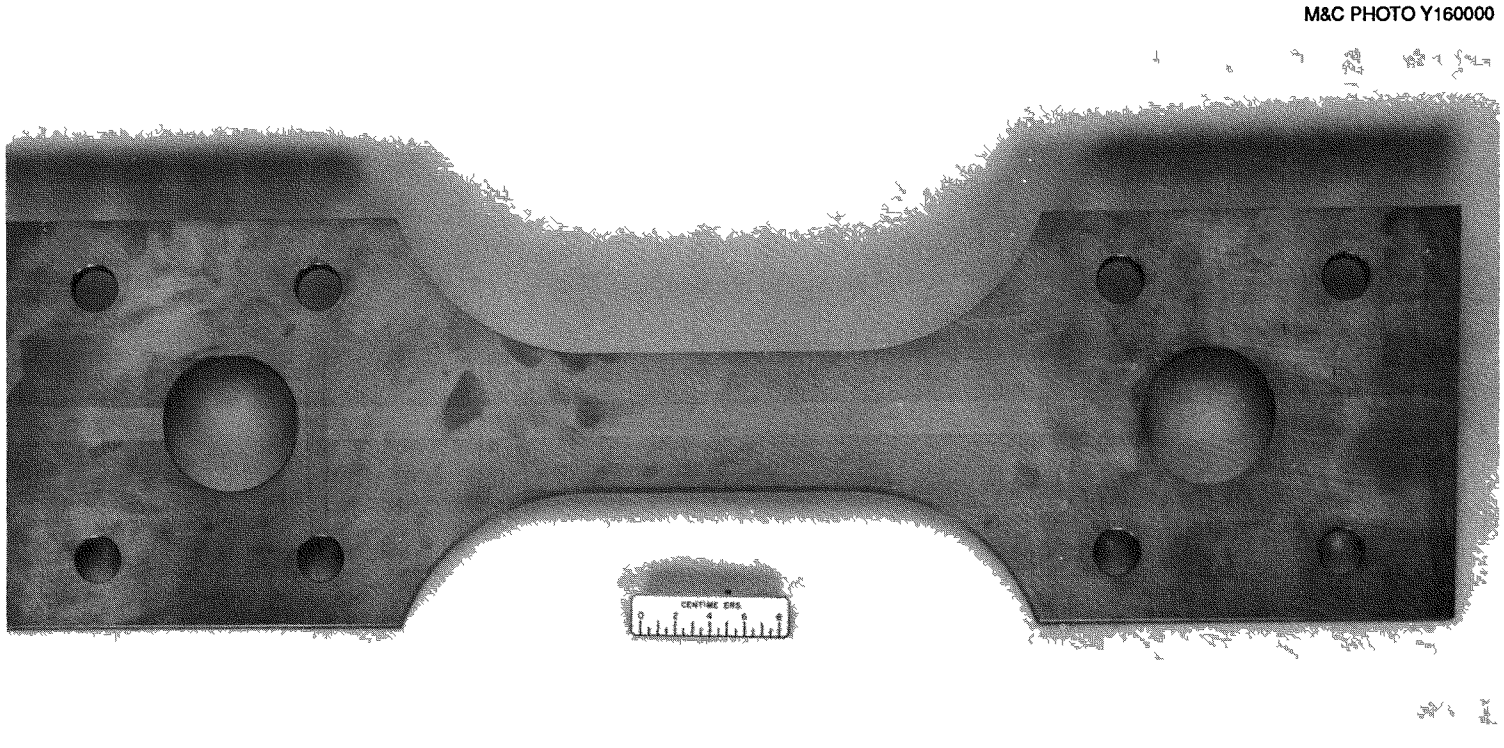


Fig. 10. Large composite creep specimen, typical of WPCT-7.

A schematic of the welded cylinder creep test specimen and grips is shown in Fig. 11. Figure 12 is a photograph of the WCCT-1 specimen. The base material for the specimen was 316 stainless steel, reference heat 8092297. The product form was 102-mm-nominal-diam, Sched.-160 pipe. The base metal was solution annealed before welding in a manner identical to that for the blanks for the plate test specimens except that the hold time at 1093°C was 30 min instead of 1 h. The average wall thickness in the gage length was 518 mm (0.204 in.) for both specimens. The average outside diameters for WCCT-1 and -2 were 102.1 mm (4.021 in.) and 104.0 mm (4.095 in.), respectively. The 16-8-2 weld material was machine deposited using the normal gas tungsten arc process. Preparation for each weld consisted of a single, 15° included-angle, V groove with a 6.35-mm (0.25-in.) root opening. Three welds were included in the test section of each specimen to address weld-to-weld variability.

## 3.3 Specimen Instrumentation

The instrumentation of WPCT-5 consisted of five HITEC high-temperature capacitance strain gages, six two-element foil gage rosettes, and ten thermocouples, as shown in Fig. 13. The foil gages were used to check proper alignment (minimum bending) of the specimen when it was initially mounted in the test facility. Also, the gages were used to ensure that specimen design features resulted in proper strain responses and distributions. A description of the high-temperature capacitance gage system is contained in Ref. 17. Four of the capacitance-type gages were positioned along the axial centerline of the specimen and were oriented axially. Two of these centerline gages were mounted back-to-back on opposite sides and centered on the transverse centerline of the specimen. The third centerline gage was located at one end of the specimen gage length [76.2 mm (3.0 in.) from the transverse specimen centerline], with no part of the gage length in the transition or taper region. The fourth centerline gage was mounted midway along the taper [139.7 mm (5.5 in.) from the transverse specimen centerline] at the same end of the specimen as the third gage. All four centerline gages were of the

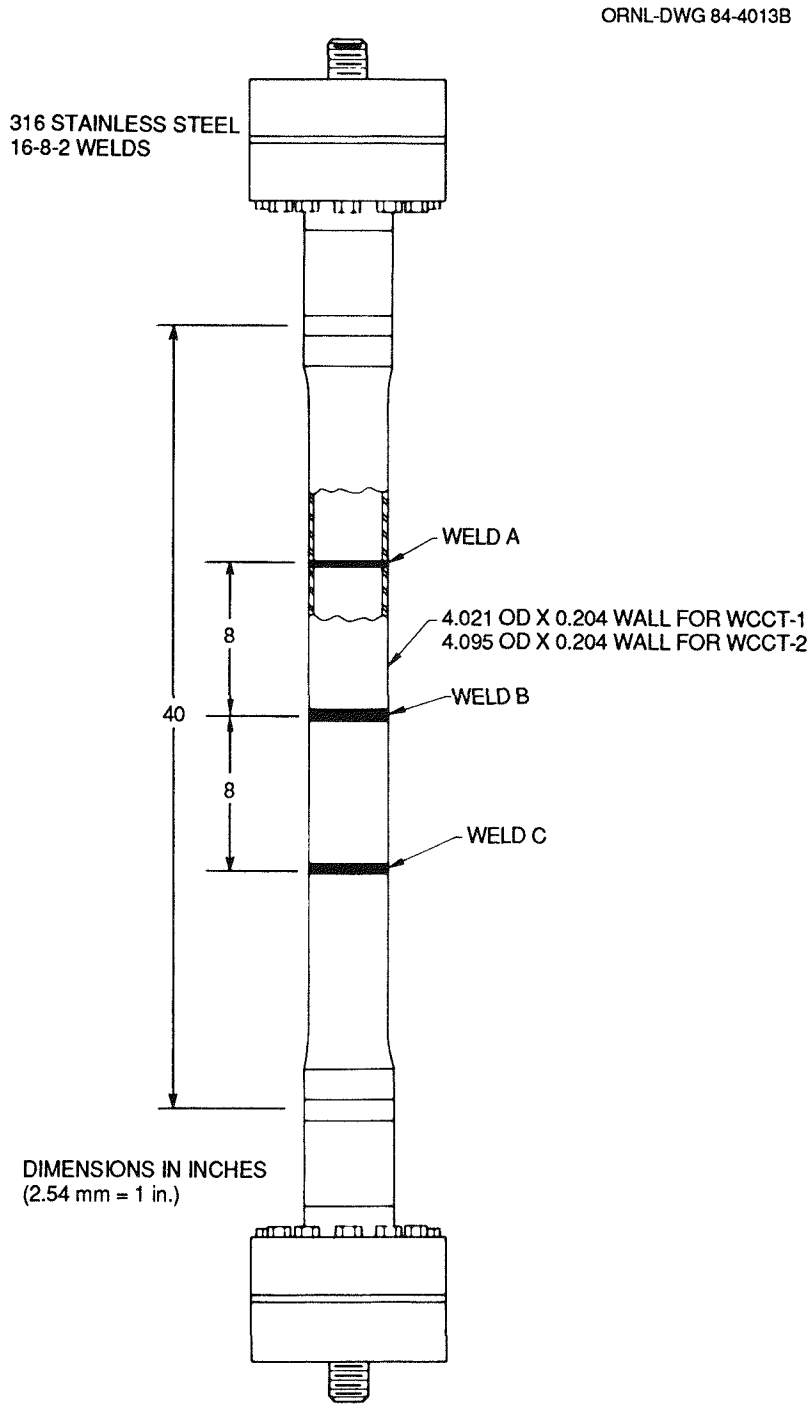


Fig. 11. Welded cylinder creep specimens and associated grips (25.4 mm = 1 in.).

ORNL PHOTO 7002-84

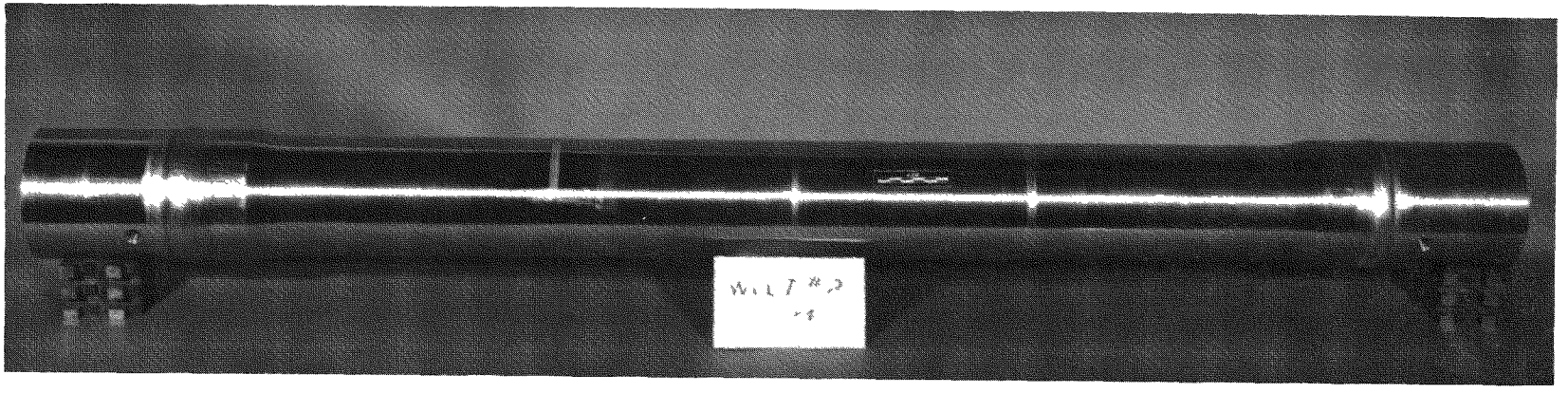

Fig. 12. Photograph of welded cylinder creep test specimen.

ORNL PHOTO 5496-88

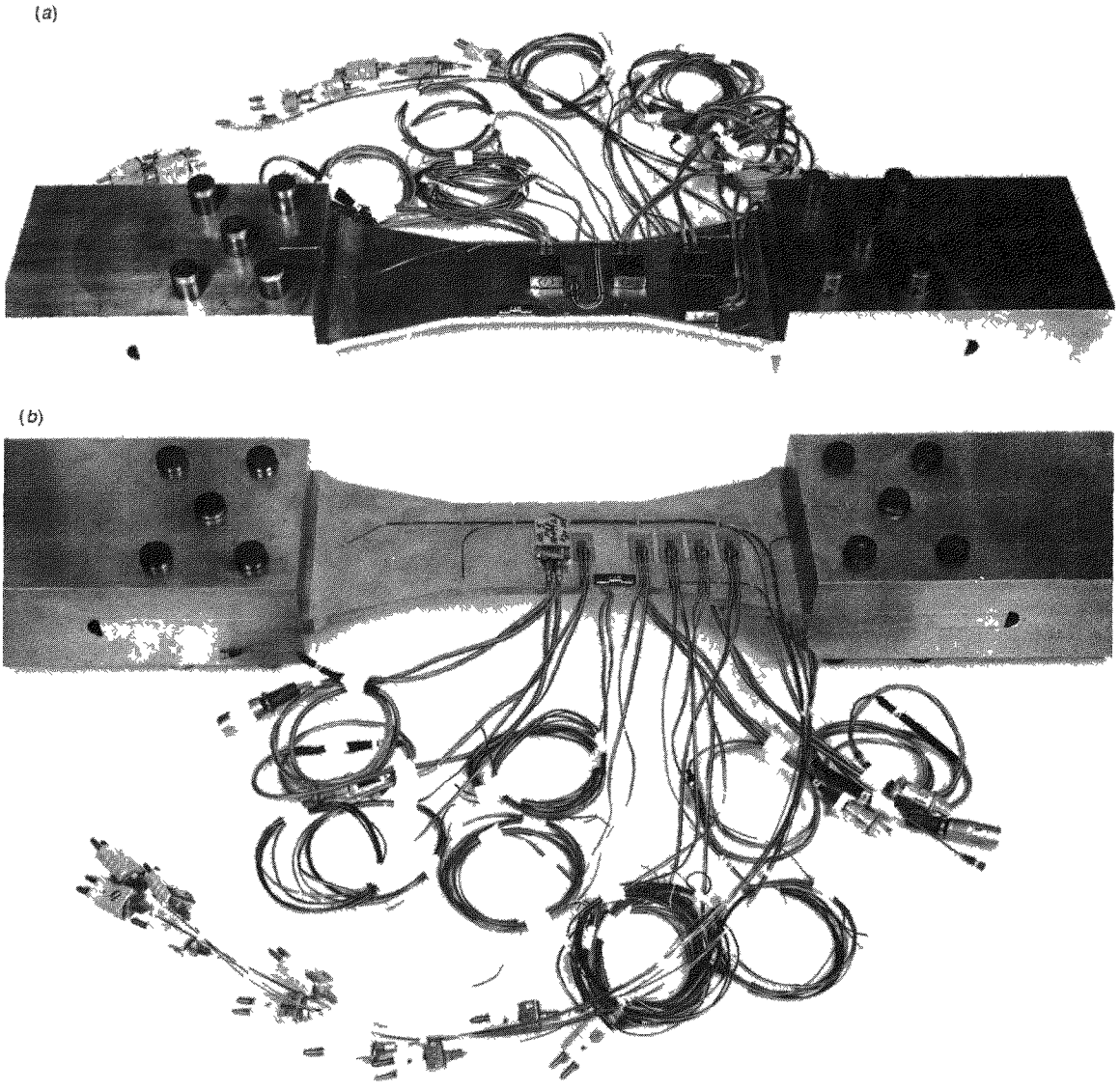


Fig. 13. Type 316/16-8-2 weldment specimen WPCT-5 instrumented for testing.

6.35-mm (0.25-in.) gage-length type and were installed with shims, resulting in an effective gage length of 3.18 mm (0.125 in.). The fifth gage was positioned 38.1 mm (1.5 in.) from the axial centerline and at the same axial location as the fourth gage. This 25.4-mm (1-in.) gage was oriented transversely.

The ten Chromel-Alumel (Type K) thermocouples were positioned in the taper and gage-length regions. These thermocouples were used to ensure

an even temperature distribution. An MTS 445-kN (100-kip) load cell was used throughout the test to measure and control load.

The instrumentation for WPCT-7 consisted of one axial extensometer and nine thermocouples, similar to the instrumentation shown in Fig. 14. The extensometer was developed in-house. The measurement devices were dial indicators. The gage length was 15.24 cm (6 in.). The nine Chromel-Alumel thermocouples were used to obtain an even temperature distribution. Also, bending was minimized by using foil gages to guide specimen alignment before test initiation.

A schematic of the instrumentation used on WCCT-1 and -2 is shown in Fig. 15. The nominal instrumentation consisted of 10 HITEC strain gages, 12 Chromel-Alumel (Type K) thermocouples, and one MTS 445-kN (100-kip) load cell. Only ten thermocouples (TC-2 through TC-11) were used on WCCT-1. Each strain gage had a nominal gage length of 6.35 mm (0.250 in.), but three were installed with shims to effectively decrease gage length and increase range by a factor of 2. Two were biased by the manufacturer for tensile strain only. Two were mounted circumferentially rather than axially. Specific information is listed in Table 1.

Table 1. Nominal characteristics of strain gages for weldment cylinder creep test WCCT-1 and -2

| Gage No. | Effective gage length [mm (in.)] | Effective strain limits (%) | Angle between gage axis and specimen axis (deg) |
|---|---|---|---|
| A1 | 6.35 (0.25) | −8, +8 | 0 |
| A2 | 6.35 (0.25) | −8, +8 | 0 |
| A3 | 6.35 (0.25) | −8, +8 | 0 |
| AB1 | 6.35 (0.25) | 0, +16 | 0 |
| AB2 | 6.35 (0.25) | −8, +8 | 90 |
| AB3 | 6.35 (0.25) | 0, +16 | 0 |
| B1 | 3.18 (0.125) | −16, +16 | 0 |
| B2 | 3.18 (0.125) | −16, +16 | 0 |
| B3 | 3.18 (0.125) | −16, +16 | 0 |
| B4 | 6.35 (0.25) | −8, +8 | 90 |

CYN PHOTO 3708

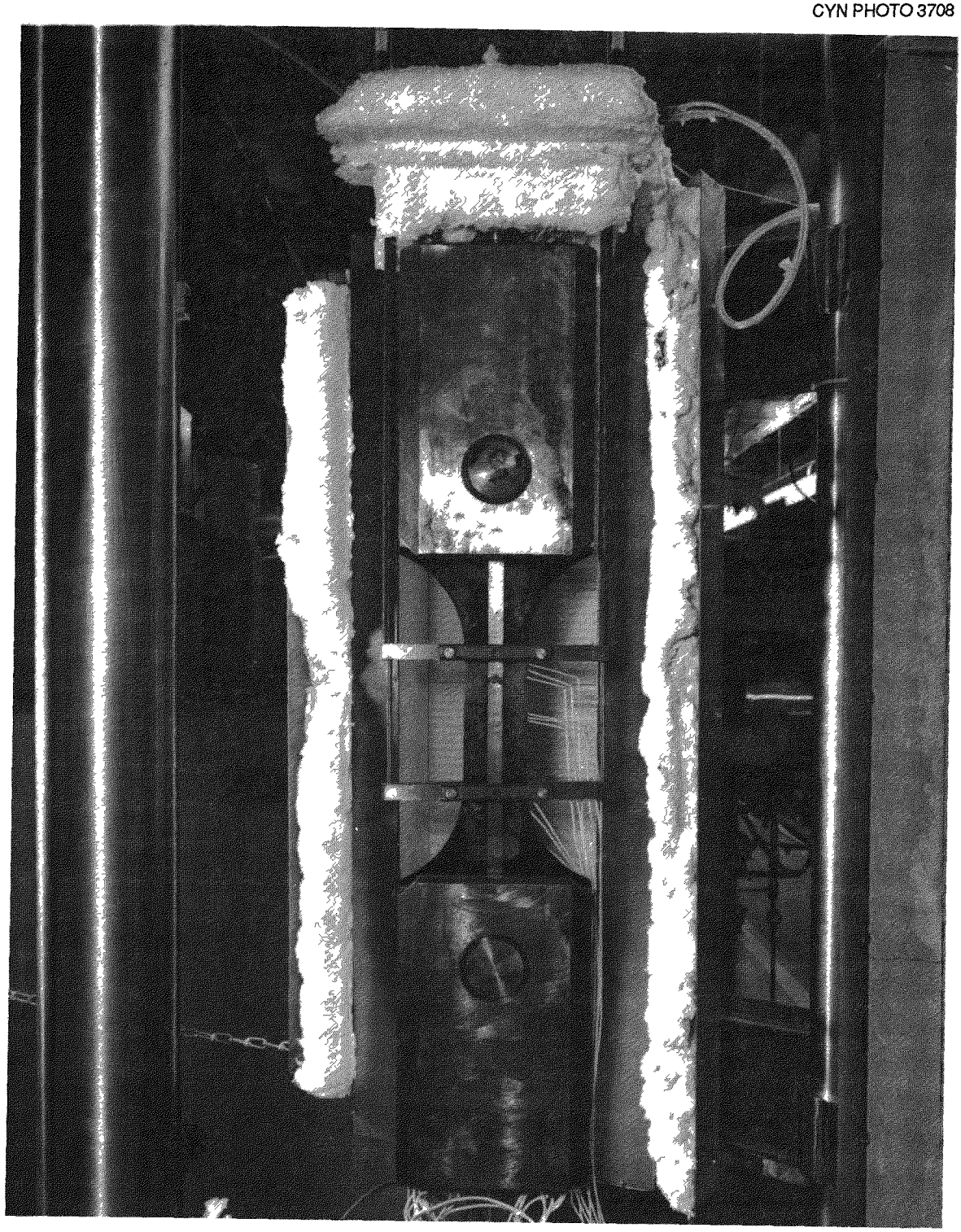

Fig. 14. Instrumentation typical of that used on WPCT-7.

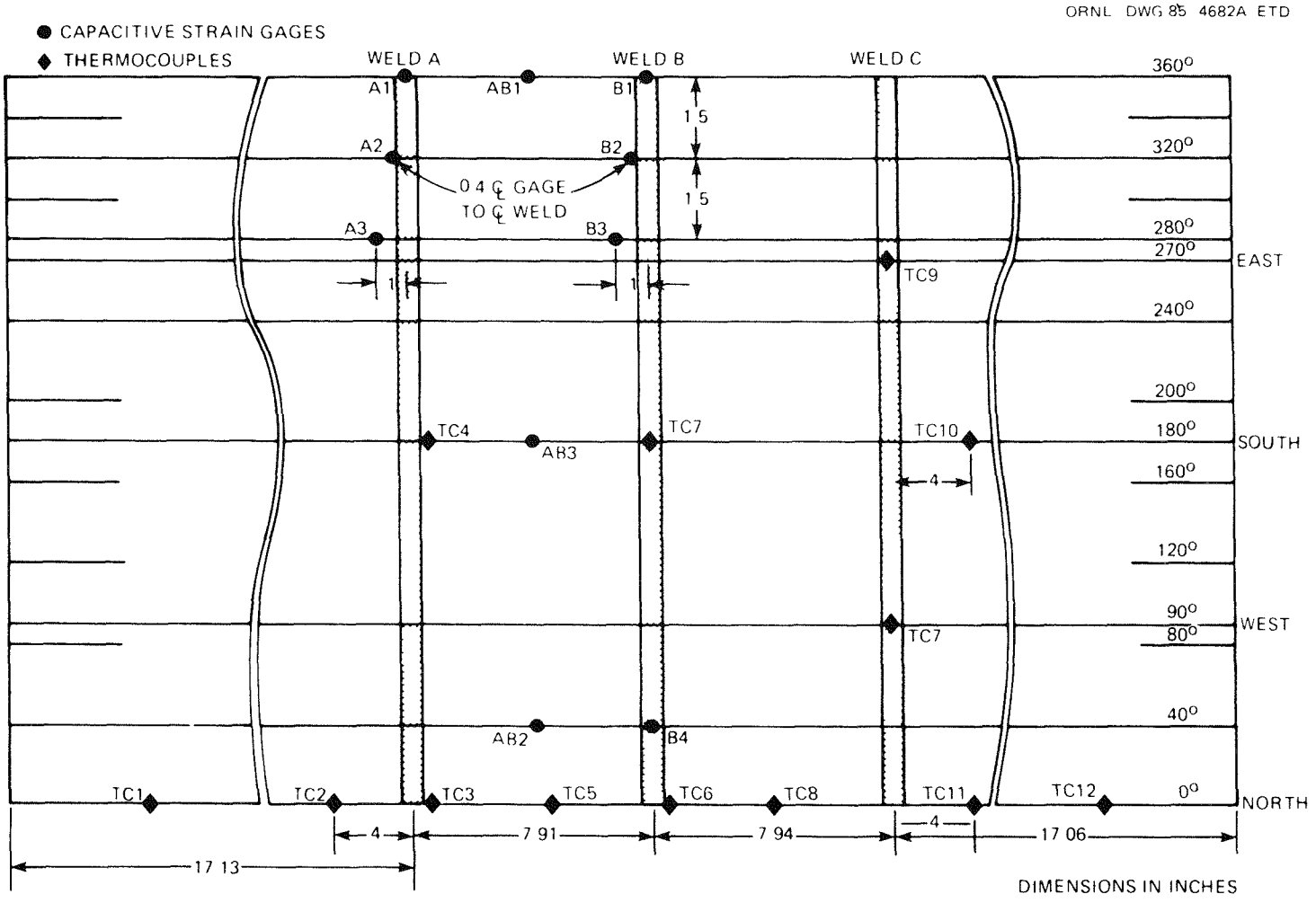


Fig. 15. Instrumentation location schematic for welded cylinder creep tests WCCT-1 and -2 (1 in. = 25.4 mm).

## 3.4 Loading Histories

The same basic facility was used for tests WPCT-5, WCCT-1, and WCCT-2. The main component of the facility (shown in Fig. 16) was a four-post MTS Uniaxial Test Machine Model 311.21. The maximum capacity of the machine was 490 kN (110 kip). An MTS Model 442 controller and a locally developed ramp generator were employed as the control system. A 20.7-MPa (3000-psi) hydraulic power supply was used to provide pressure to the load frame.

Two heating systems were used for those three tests. An in-house designed rectangular furnace was used for test WPCT-5. Lindberg flat resistance heating units (Model 50736) were used, and the control system used one temperature controller and five autotransformers to provide proportional zone control. The heating system for tests WCCT-1 and -2 consisted of a Hevi-duty clam-shell furnace with an independent temperature controller for each of four control zones. The furnace had a 20.3-cm (8-in.) inside diameter and was split into a top and bottom zone. Two guard heaters were used at the specimen ends to obtain a uniform temperature profile along the specimen length.

A data acquisition system (DAS) was used to collect, store, and process data for tests WPCT-5, WCCT-1, and WCCT-2. The structural test DAS was a Hewlett-Packard (HP) model 9603A, which used a HP 2117F computer with 256 K bytes of memory. The software system was the HP disk-based, real-time executive system RTE-IVB. The programming language was Fortran. An ORNL-developed DAS program facilitated efficient data reduction. Raw voltage data were recorded in real time on magnetic tape and on HP disks. Preliminary data analyses were performed and displayed on site using a graphics terminal. Final detailed analyses were performed on the IBM 3033 computers at the ORNL Computing Center.

The DAS was capable of scanning, digitizing, and recording dc voltage signals for 240 separate sensor signals at a maximum scan rate of approximately two scans per second. One of the two scan modes, high-speed or averaging, was automatically chosen and executed by the data acquisition operating program when a scan sequence was requested. The high-speed scan mode was executed when a period of <1 min was specified

ORNL PHOTO 7219-84

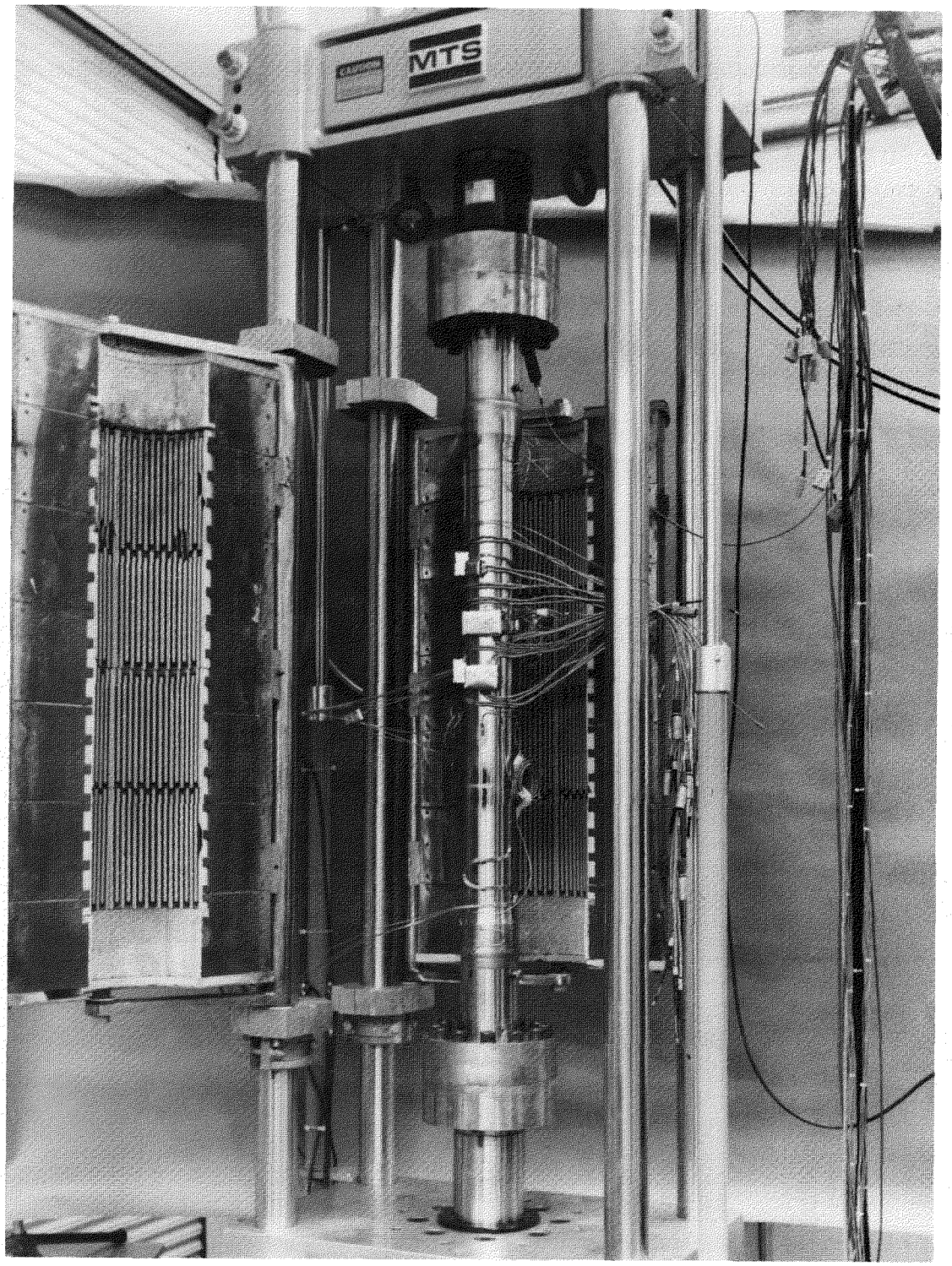


Fig. 16. Weldment creep facility photograph with WCCT-1 specimen installed.

(during load changes); the averaging mode was executed when a period of ≥1 min (during load hold periods) was specified. The averaging scan mode improved the system accuracy by quickly taking and then averaging ten scans to form a single sensor value.

The facility for testing WPCT-7 used a 200-to-1 dead weight knife-edge lever system to apply a constant load to the specimen. A photograph of the load frame and typical specimen furnace is shown in Fig. 17. The temperature furnace and control system were similar to the system described above for test WPCT-5.

The load histogram for the welded plate creep test WPCT-5 is shown in Fig. 18. Crack inspections were performed at test durations of 1190, 1955, 2388, 3567, and 6965 h, following histogram points 6, 10, 14, 22, and 34, respectively. Plantwide power outages caused the loss of load at histogram points 2 and 25. The load was removed at point 29 to repair an uninterruptable electrical power supply that allows orderly shutdown in the event of power outages. The unloading at point 17 occurred because of a problem with the hydraulic power supply. The specimen was subjected to a constant load of 213 kN (48 kips) corresponding to an axial stress of 221 MPa (32 ksi). The load changes were accomplished at a constant rate of 7.1 kN/s (1.6 kips/s). The indicated temperature over the reduced width gage length of the specimen was maintained at 565.5 ± 2.5°C (1050 ± 5°F) throughout the test, except for shutdowns for crack inspections and power outages. The test ended because of specimen separation with 7190 h of total test time at the hold period stress (histogram point 37).

The WPCT-7 plate specimen was subjected to a constant load of 146.7 kN (33 kip) corresponding to an axial stress of 152 MPa (22 ksi). The test temperature was 565.5°C (1050°F). The test was interrupted at 4400 h of hold time caused by failure in the grip area. As previously explained, the specimen was repaired by electron-beam-welding new ends on the specimen and machining the specimen to an improved design. The test was continued at an axial load of 84.5 kN (19 kip) corresponding to an axial stress of 171 MPa (24.8 ksi) for 6000 h and terminated with only minimum cracking.

CYN PHOTO 3479

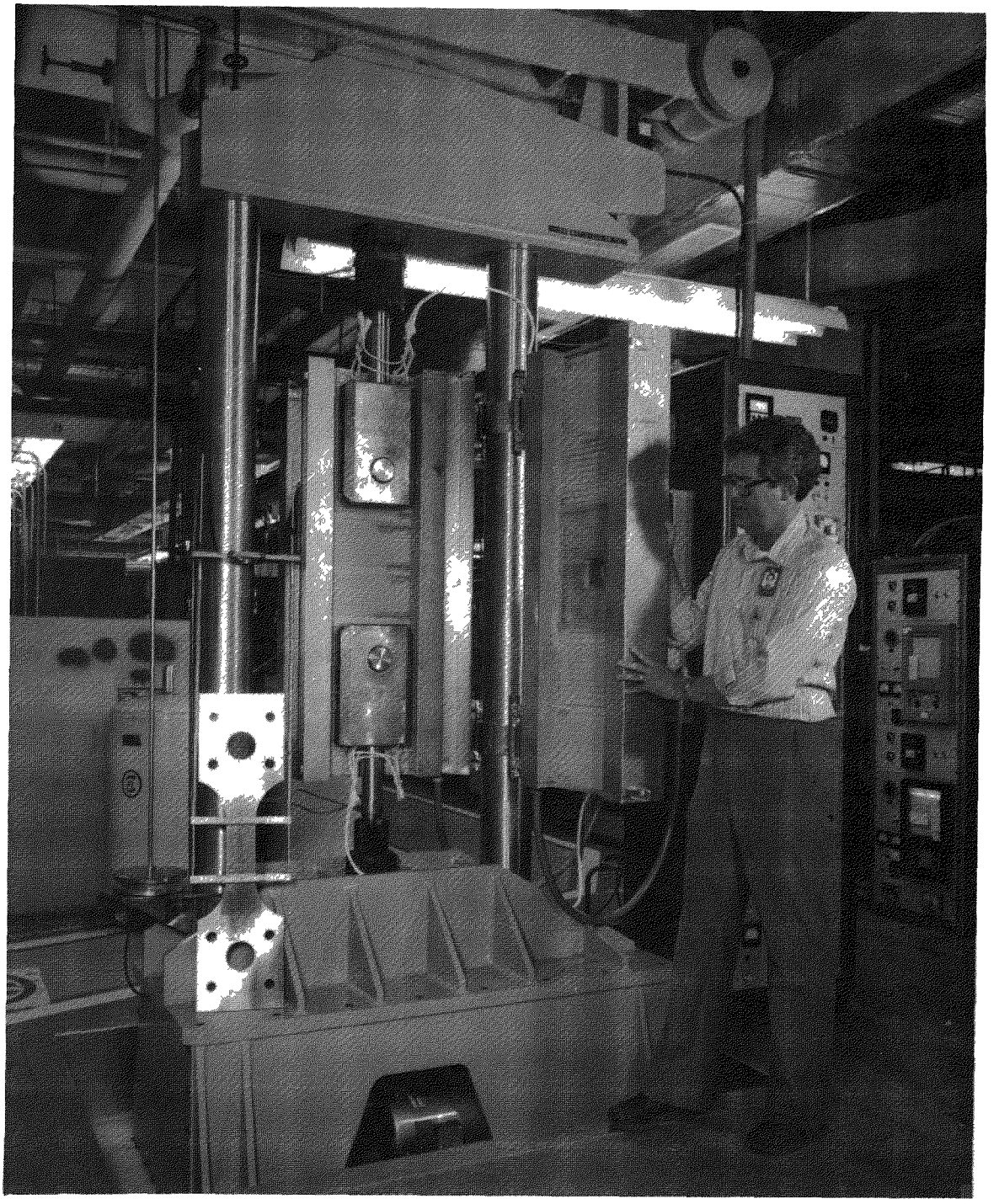

Fig. 17. Photograph of the weldment creep facility used in the WPCT-7 test.

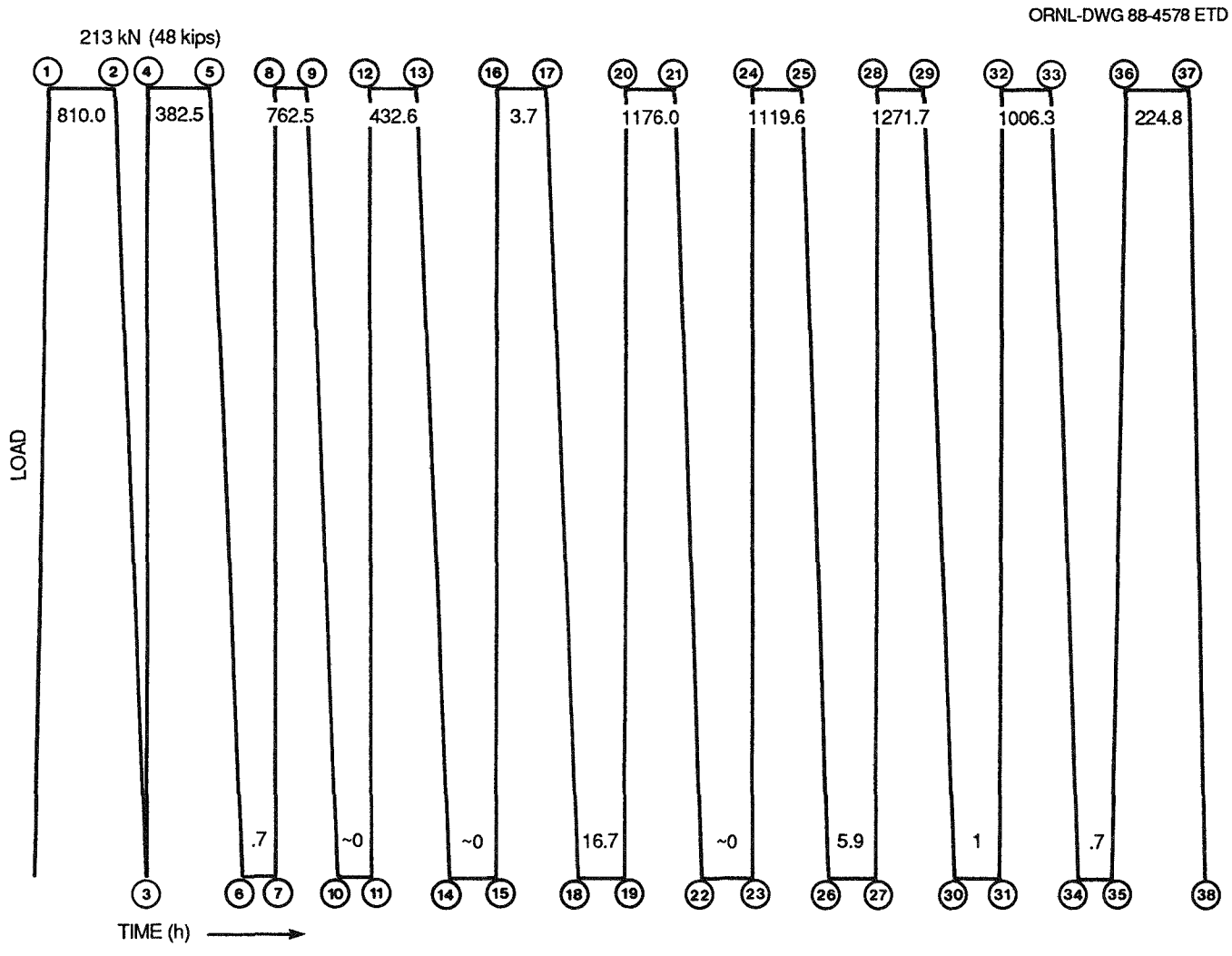


Fig. 18. Axial load histogram for the welded plate creep test WPCT-5.

The temperature and load histograms for test WCCT-1 are shown in Fig. 19. The temperature over the center 61 cm (24 in.) of the specimen was maintained at 565.5 ± 4°C (1050 ± 8°F) throughout the test duration, except for shutdowns for crack inspection. Those inspections occurred after histogram points 3 and 9. Nontest time at temperature was minimized except for 71 h between points 7 and 8. The specimen was subjected to a constant load of 347 kN (78 kips) corresponding to an axial stress of 221 MPa (32 ksi). The loading and unloading steps were accomplished at a linear rate of 11.6 kN/s (2.6 kips/s). The initial loading was prematurely halted at ~311 kN (70 kips) for 6.5 min and then continued. An accidental instantaneous overload of more than 445 kN (100 kips) and unloading occurred after histogram point 6. The exact amount of the

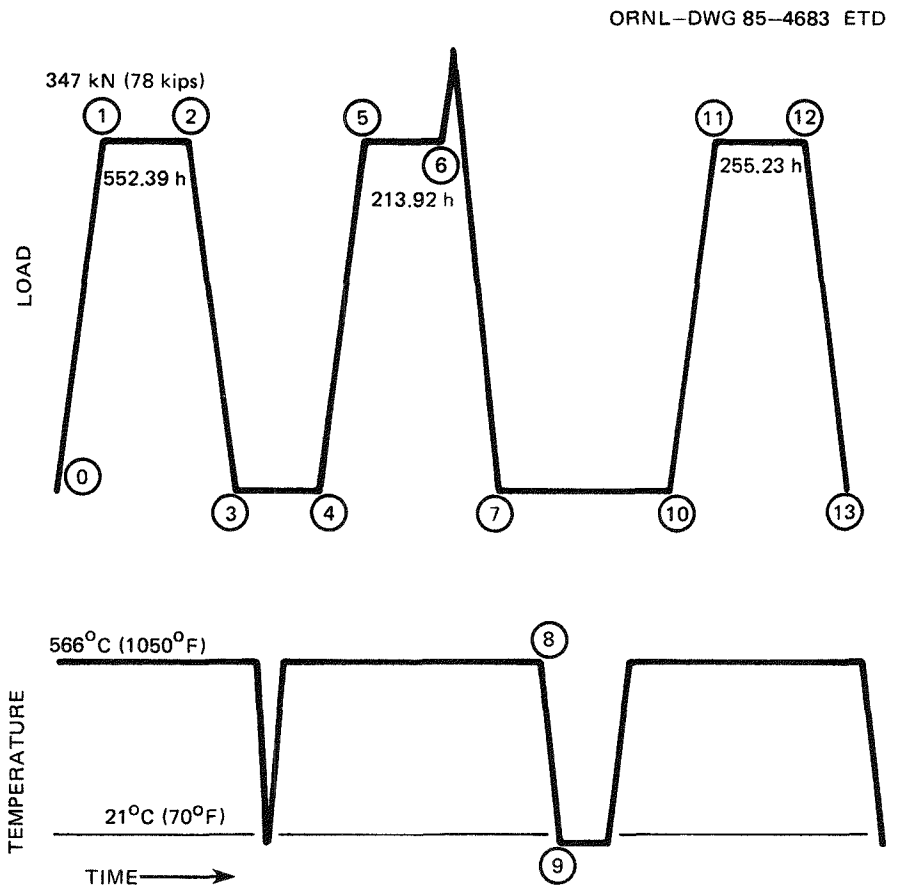


Fig. 19. Axial load and temperature histograms for welded cylinder creep test WCCT-1.

overload could not be determined. The problem was corrected, and the test was continued to specimen separation.

The load histogram for test WCCT-2 is shown in Fig. 20. Crack inspections were performed at nominal test durations of 502, 1002.6, 2010.2, 3985.8, and 8085.2 h, following histogram points 3, 7, 15, and 31, respectively. A plantwide power outage caused the loss of load at histogram point 10, and the load was removed at point 18 to repair an oil leak at the hydraulic pump. The unloadings at histogram points 23 and 27 were necessary to repair the hydraulic power supply. The shutdown at point 23 was extended to a total of ~6 months at room temperature because of a local construction project and repair of two uninterruptable power supplies. The specimen was subjected to a constant load of 311 kN (70 kips), corresponding to an axial stress of 193 MPa (28 ksi). The load changes were accomplished at a constant rate of 10.2 kN/s (2.3 kips/s). The indicated temperature over the central 61 cm (24 in.) of the specimen was maintained at 565.5 ± 4°C (1050 ± 8°F) throughout the test, except for shutdowns for crack inspections, the power outage, and one prolonged temperature excursion caused by a heater element burnout and the over-compensation of the adjoining heating zone. The excursion occurred between 7167 and 7942 h, and the maximum temperature reached was 593°C (1100°F). The affected region was centered around weld "B," specifically thermocouples TC-5, -6, -7, and -8 (see Fig. 15).

## 3.5 Inspection Procedure

In situ field metallographic examinations were performed for tests WPCT-5, WCCT-1, and WCCT-2 at periodic intervals to observe crack development processes. These processes are described later in this report. The examination procedure is fully reported in Ref. 18 but, briefly, consists of the following. The surface regions of interest (welds) were polished with a technique that minimized metal smearing. Each region was etched with aqua regia (50 mL hydrochloric acid, 10 mL nitric acid, and water) to reveal grains, grain boundaries, and cracks. The surface was then replicated by means of room-temperature-vulcanized (RTV) rubber. High-magnification optical microscopy was used to photograph the rubber

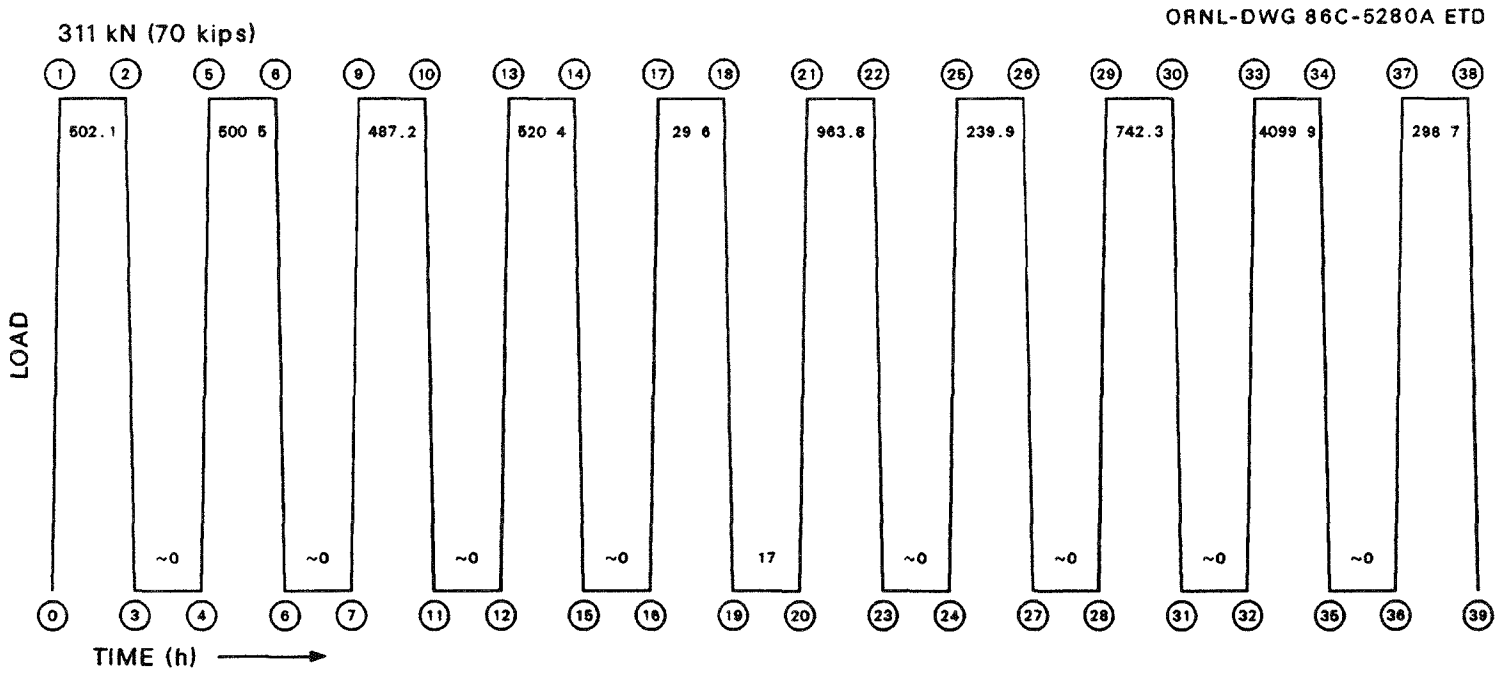


Fig. 20. Axial load histogram for welded cylinder creep test WCCT-2.

replicates or plastic positive replicates of the RTV negatives. Direct photography of dye-penetrant inspections was also performed once the cracks were large.

# 4. INELASTIC FAILURE ANALYSES

In a previous study of type 304/308 CRE stainless steel plate weldments[11] it was found that a bimetallic model, consisting of weld metal and base metal only, failed to predict accurately the deformation and failure of the weldment. Detailed mechanical property tests of specimens taken across the weldments revealed a continuous variation of properties. A multiple-zone model, consisting of weld metal, fusion line, HAZ, and base metal, was therefore developed for inelastic weldment analyses. By assigning different material properties to each zone to capture the variability, this structural model predicted deformations, time to failure, and character of failure of the weldments that were in good agreement with the experimentally measured plate weldment data.

The multizone model was also used in the analyses of a type 304/308 of CRE welded beam under pure bending loading.[19] Again, the prediction of deformations was good. Because of these successful applications, the multizone model was used in all of the analyses reported here.

## 4.1 Constitutive Model

A constitutive model is a set of mathematical statements or equations describing material behavior under time-varying multiaxial loads. The analytical procedures and constitutive model used in this study were consistent with those recommended in NE standard F 9-5T (Ref. 20). They represent the current state-of-art extensions from classical plastic and creep theories for inelastic material response predictions. Some ad hoc rules recommended in the standard were also adopted whenever their applications were considered appropriate. These included (1) $\alpha_{ij}$-reset procedures to prevent unrealistic movement of the yield surface in multiaxial stress space under completely reversed-cyclic loadings, and (2) a procedure to change the isotropic hardening parameter $\kappa$ according to accumulated inelastic strain.

## 4.2 Failure Model

For creep-rupture failure predictions, the linear time fraction damage accumulation criterion was used. According to this criterion, the damage at any time t is

$$D = \sum \frac{\Delta t_i}{T_{d_i}} ,$$

where $\Delta t_i$ is the duration and $T_{d_i}$ is the creep-rupture time at the equivalent stress level, $\sigma_i$. Note that according to the linear time fraction criterion, the component fails (cracks) when the creep damage value D reaches 1.0.

Because the creep-rupture time curves are usually obtained from uniaxial creep-rupture tests, an appropriate multiaxial strength model must be used to compute an equivalent uniaxial stress $\sigma_e$ for a multiaxial stress state. Several classical strength models such as the von-Mises effective stress, Tresca maximum shear stress, and Rankine maximum stress are well known and often used. In this study, however, the recently developed ORNL multiaxial strength model[21,22] was used. According to this model, the equivalent uniaxial stress $\sigma_e$ is defined as

$$\sigma_e = \frac{3}{2} S_1 \left(\frac{2\ \bar{\sigma}}{3\ S_1}\right)^a \exp\left[b\left(\frac{J_1}{S_s} - 1\right)\right] ,$$

where $S_1$ denotes the maximum deviatoric stress, $J_1$ is the first invariant of the stress tensor, $\bar{\sigma}$ denotes the von-Mises effective stress, and $S_s$ is given by

$$S_s = \sqrt{\sigma_1^2 + \sigma_2^2 + \sigma_3^2} ;$$

$\sigma_1$, $\sigma_2$, and $\sigma_3$ are the principal stresses.

Parameters *a* and *b* are material constants. They represent, in a broad sense, the sensitivities of the fracture process in a material to shear distortion and hydrostatic stress, respectively. The values for *a* and *b* used in this evaluation were 1.0 and 0.24, respectively, which are

found to be universal values applicable to 304 and 316 stainless steel and Inconel.[22]

## 4.3 Weldment Materials Data

### 4.3.1 Specimen selection

The mechanical properties characterization data needed for the constitutive and failure models for the 316/16-8-2 weldments were acquired through testing tensile specimens cut from typical weldments. Figure 21 indicates the location for each of the specimens used to develop the four-zone weldment model. Weld and base specimens contained only those materials. The fusion line specimens contained a mix of weld and base materials. The gage length of the HAZ specimens was composed entirely of base material, but the welding process had the potential to change significantly the material properties. As depicted in Fig. 21, the weld was made with parallel walls rather than being a V-shaped weld. This configuration was selected to simplify the analysis, but it also helped to isolate regions for the mechanical property tests. About 24 specimens

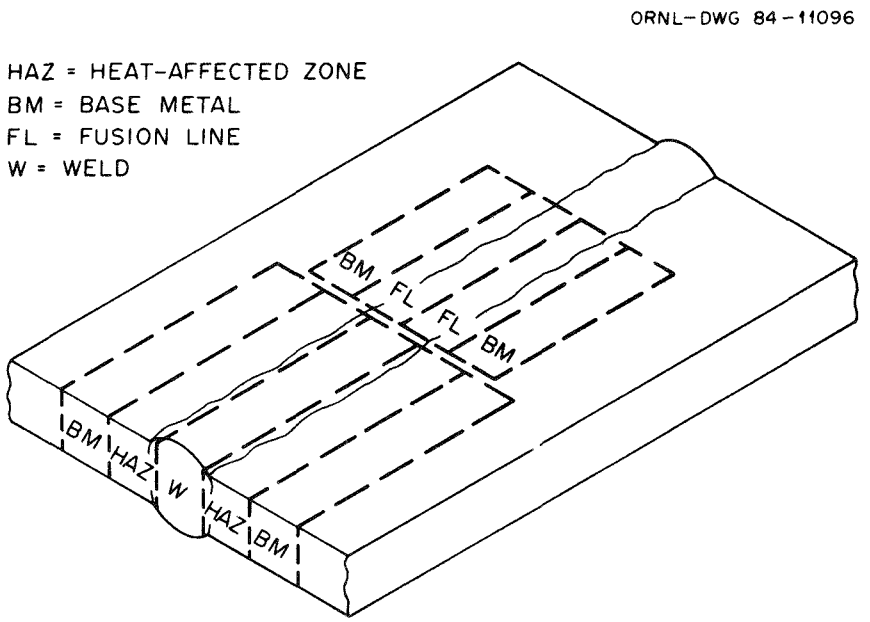


Fig. 21. Mechanical properties specimen locations relative to 316/16-8-2 weldment.

were successfully tested to provide a good basis for predicting the creep damage and inelastic strain encountered during the structural tests. Table 2 summarizes the mechanical properties that were actually used to characterize each structural zone in the analyses.

Table 2. Material properties used for each weldment zone

| Structural zone | Categories | | | | | |
|---|---|---|---|---|---|---|
| | Elastic modulus | Poisson's ratio | Yield stress | Plastic modulus | Damage | Creep strain |
| Weld | BM | BM | W | W | W | W |
| Fusion line | BM | BM | FL | BM | FL | FL |
| HAZ | BM | BM | HAZ | BM | HAZ | HAZ |
| Base metal | BM | BM | BM | BM | BM | BM |

### 4.3.2 Bilinear stress-strain representations

Typical stress-strain curves for weld metal, fusion line, HAZ, and base metal are shown in Fig. 22. From curves such as these, the yield stress and plastic modulus were determined for each of the weldment zones. The weld metal and fusion line specimens exhibited more than twice the yield strength of the base metal specimens. These data were not recorded in such a way that the elastic modulus could be evaluated accurately. Consequently, the base metal elastic modulus was used for all the zones. Because better data were lacking, the Poisson's ratio was also held constant for all four of the weldment zones. While the yield stress and plastic modulus are quite important, the remainder of the linear material property variations from base material values were considered relatively unimportant. These data are summarized in Table 3 for the 316/16-8-2 stainless steel materials used in the weldment tests.

### 4.3.3 Creep strain representations

The tensile specimens were held at a constant temperature of 565.5°C (1050°F) at various levels of stress, and the creep strain was recorded.

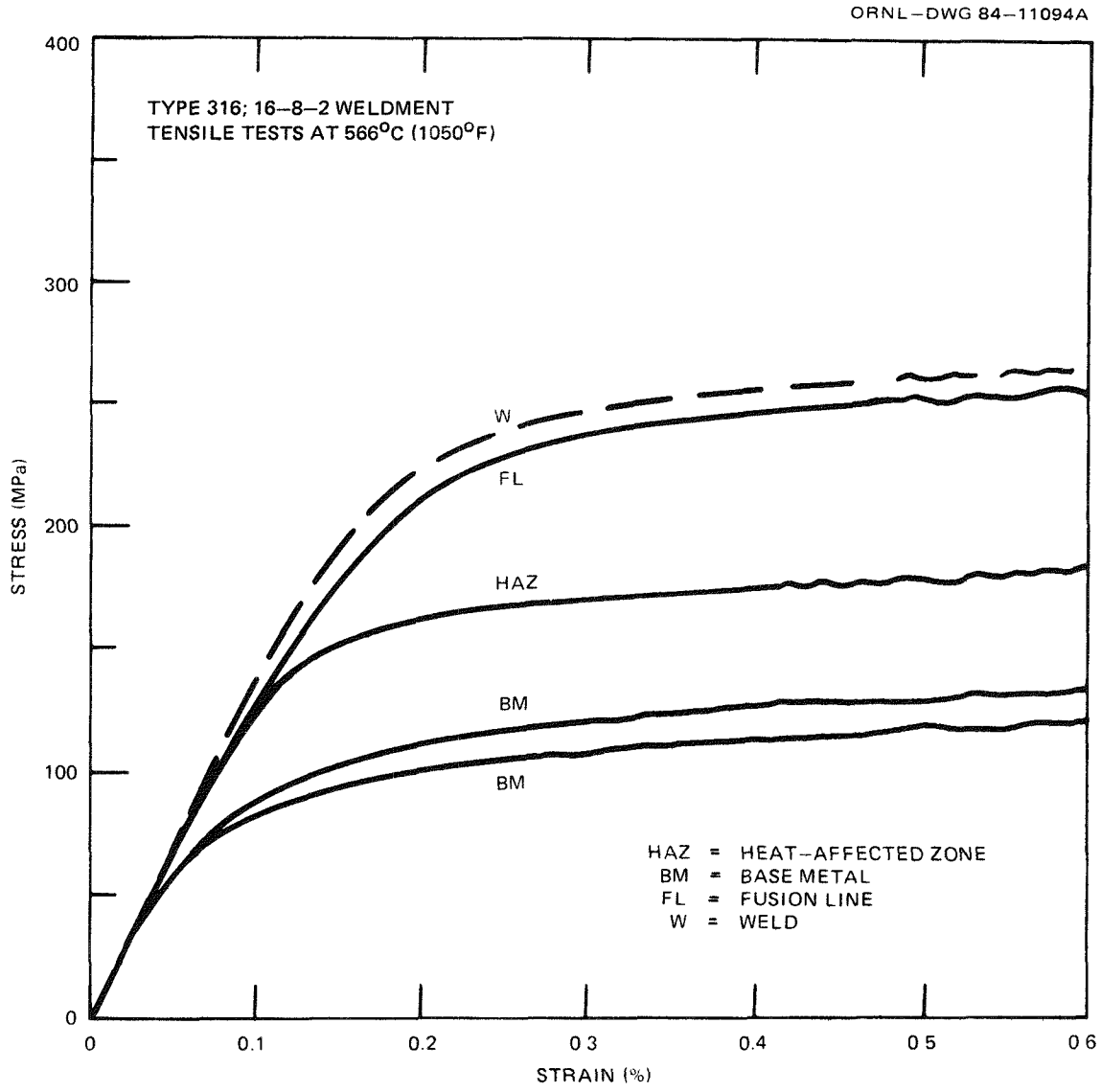


Fig. 22. Typical stress vs strain curves for each of the four weldment zones (6.895 MPa = 1 ksi, 566°C = 1050°F).

Table 3. Material property values for each weldment zone[a]

| Structural zone | Yield stress (psi) | Plastic modulus (psi) | Elastic modulus (psi) | Poisson's ratio |
|---|---|---|---|---|
| Weld | 39,700 | 2.53E5 | 21.17E6 | 0.307 |
| Fusion line | 38,800 | 2.30E5 | 21.17E6 | 0.307 |
| HAZ | 26,000 | 2.30E5 | 21.17E6 | 0.307 |
| Base | 18,000 | 2.30E5 | 21.17E6 | 0.307 |

[a]1 psi = 6895 Pa.

Figure 23 shows typical creep strain for each zone of the weldment with a constant stress of 171 MPa (24.8 ksi). Because this figure shows only the creep strains, the initial values are zero, but the total strains would include the initial loading strains shown in Fig. 22. Note from Fig. 23 that the base metal exhibits much more creep strain than the weld metal and that the fusion line metal behaves much like the weld metal. The HAZ metal creep curve falls in between the weld and base metal.

As references, longitudinal and transverse weldment specimen creep curves are also shown in Fig. 23. The transverse weldment creep strain is dominated by the strain in the base material, whereas the longitudinal weldment strain is dominated by the weld metal characteristics. This result is expected because in the transverse weldment each material is loaded in series, and the weak link (base material) thus provides the main contribution to the weldment creep strain.

The noncyclic strain hardening creep equation (No. 12) in the PLACRE computer code[23] was selected to represent each material. Because the

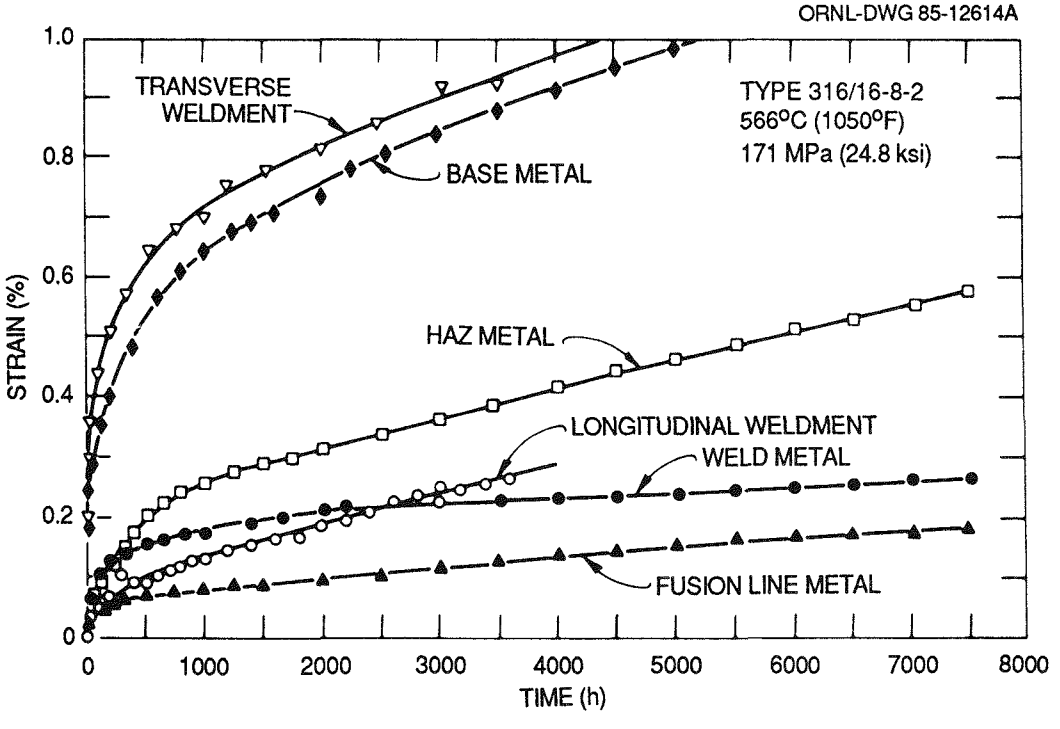


Fig. 23. Typical creep strain vs time curves for weldment zones and for longitudinal and transverse weldments.

test temperatures of the specimens and weldments were the same, the creep equation reduces to the following:

$$\varepsilon^{CR} = \underbrace{A(\sigma)[1 - e^{-R(\sigma)t}]}_{\text{Primary creep}} + \underbrace{K(\sigma)t}_{\text{Steady-state creep}} \qquad (1)$$

where

$$A(\sigma) = C_1 \, \sigma^{C_2} \, , \qquad (1a)$$

$$R(\sigma) = C_3 \, e^{C_4 \sigma} \, , \qquad (1b)$$

$$K(\sigma) = C_5 \, [\sinh (C_6 \sigma)]^{C_7} \, . \qquad (1c)$$

Specimen data were reduced for each zone, as illustrated in Fig. 24. The primary creep portion of the equation involved the determination of $A(\sigma)$ and $R(\sigma)$, as described in Eqs. (1*a*) and (1*b*). The value of A was

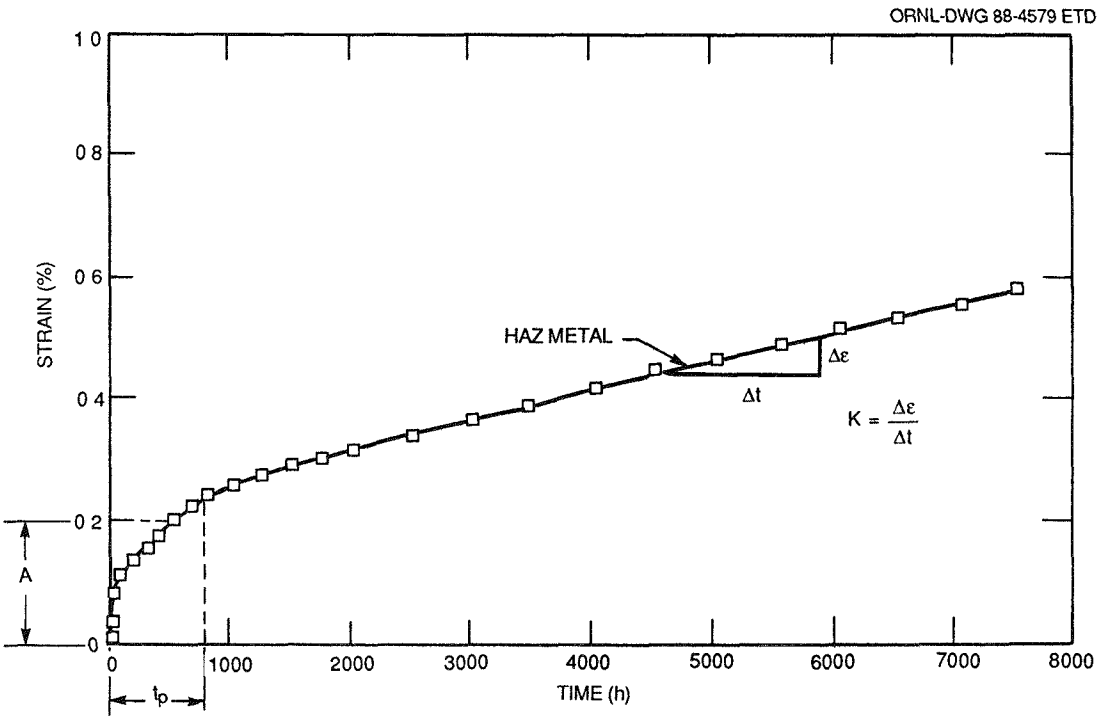


Fig. 24. Illustration of key creep equation parameters.

tabulated for each specimen by extrapolating the steady-state portion back to the beginning of the creep test.

Figure 25 presents the data base used to determine the A(σ) variation. Some engineering judgment was used to interpret these data because the slope of the curve was adopted from other 316 stainless steel reference data and the curve was positioned to "best fit" the data even though a least-squares fit would have resulted in a significantly different curve. Again, engineering judgment was exercised in that the slope

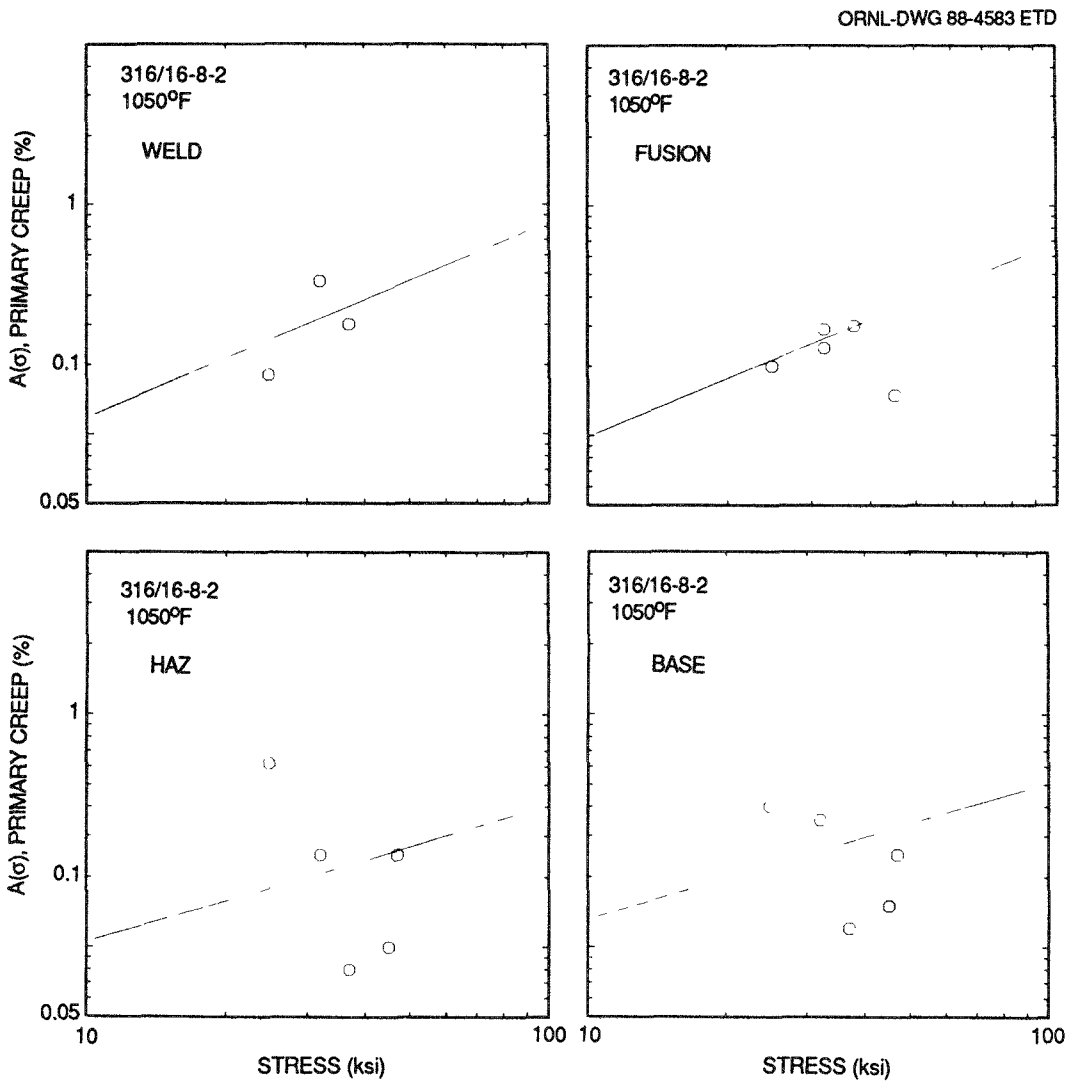


Fig. 25. Primary creep data fit to A(σ) creep equations for the four structural zones (1 ksi = 6.895 MPa, 1050°F = 566°C).

of the fusion line data was made equal to the weld data slope, and the slope of the HAZ region was set equal to the slope of the base metal curve. As can be seen from Fig. 23, primary creep is significant only for base metal; it is relatively insignificant for the other zones. Figure 26 shows a comparison of the A(σ) curves for each material zone, and Table 4 provides a summary of the coefficients for the creep equations, including all seven constants for primary and steady-state creep. The time $t_p$ in Fig. 24 was defined as the time for which 99% of the primary creep had been achieved. Thus, the exponential portion of the primary creep would take on the value of 1% so that

$$0.01 = [1 - e^{-Rt_p}] ,$$

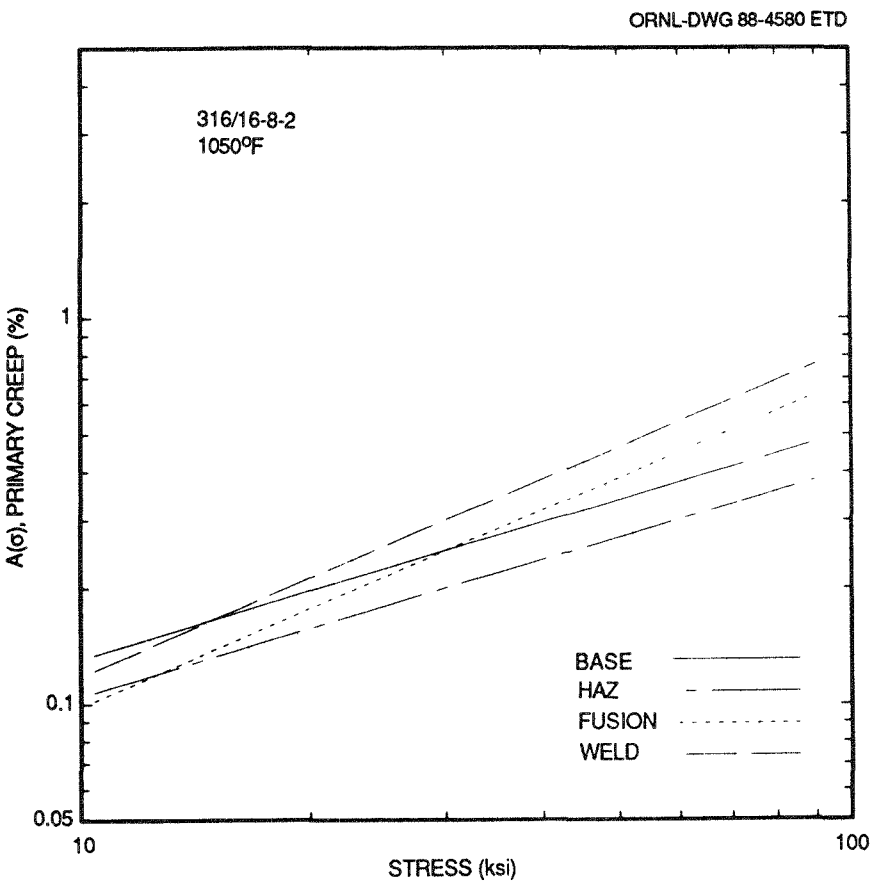


Fig. 26. Comparison of primary creep coefficients A(σ) for each zone (1 ksi = 6.895 MPa, 1050°F = 566°C).

Table 4. Coefficients for PLACRE creep equation
No. 12 for 316/16-8-2 at 565.5°C (1050°F)

| Structural zone | Primary | | | | Steady-state creep | | |
|---|---|---|---|---|---|---|---|
| | $C_1$ | $C_2$ | $C_3$ | $C_4$ | $C_5$ | $C_6$ | $C_7$ |
| Weld | 0.1683-3 | 0.847 | 0.1221-5 | 0.2879 | 0.53718-11 | 0.18179 | 2.5084 |
| Fusion line | 0.1402-3 | 0.847 | 0.1120-4 | 0.2096 | 0.19335-7 | 0.04328 | 6.8507 |
| HAZ | 0.270-3 | 0.589 | 0.2634-4 | 0.2005 | 0.27584-6 | 0.41112 | 5.0659 |
| Base metal | 0.3375-3 | 0.589 | 0.9509-5 | 0.2174 | 0.14209-6 | 0.05250 | 3.7590 |

and the R coefficient was computed for each time $t_p$ measured from the specimen data.

A least-squares fit was made on the R coefficient for each set of weldment zones to compute the coefficients $C_3$ and $C_4$ that make up the exponential relationship in Eq. (1*b*). Figure 27 shows the fit of $R(\sigma)$ with the data for each weldment. The $t_p$ values were more easily obtained from the creep curves so that much less scatter existed for these coefficients. A comparison of the $R(\sigma)$ equations is shown in Fig. 28, and a

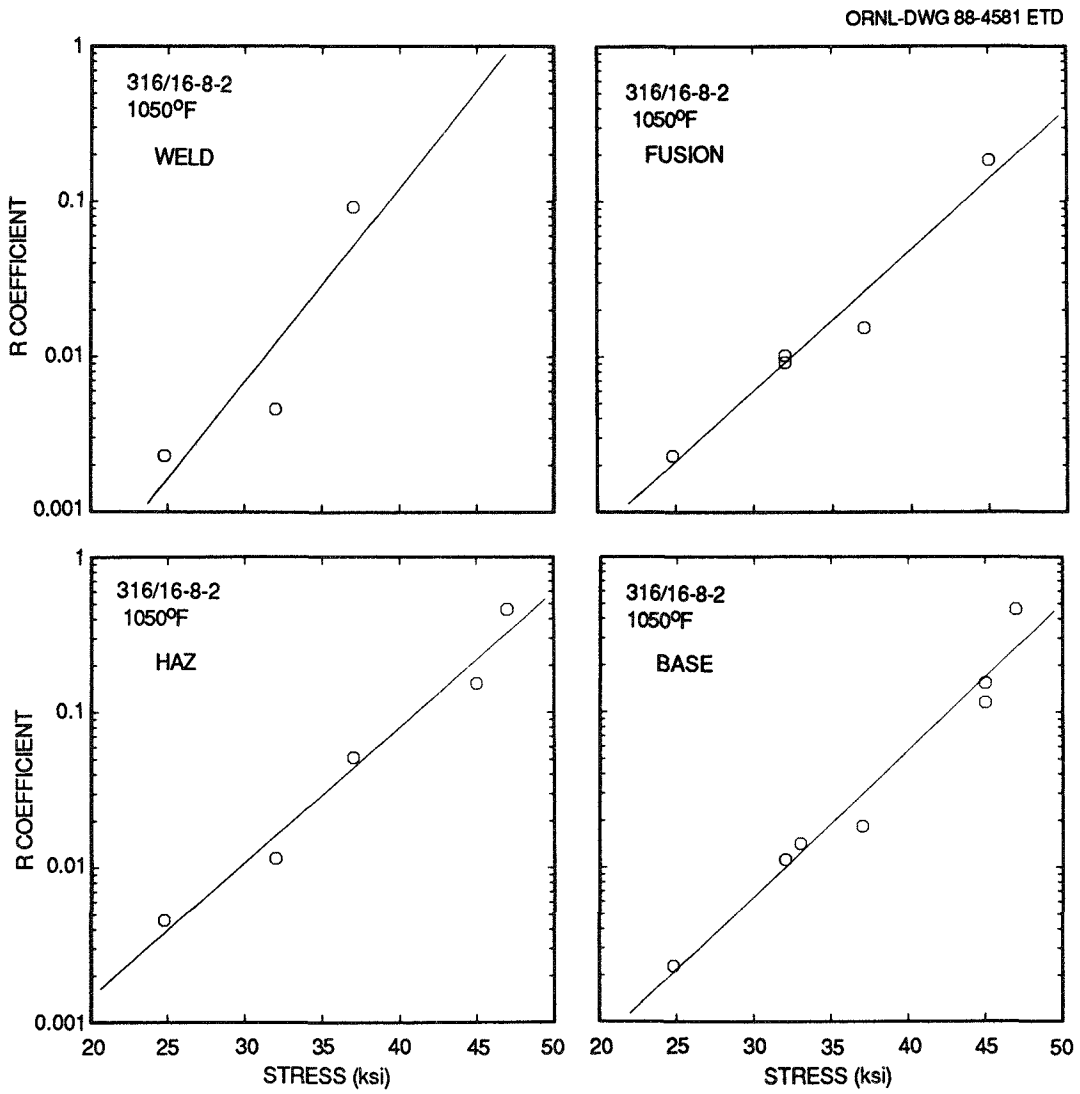


Fig. 27. Primary creep decay coefficient fit to specimen data (1 ksi = 6.895 MPa, 1050°F = 566°C).

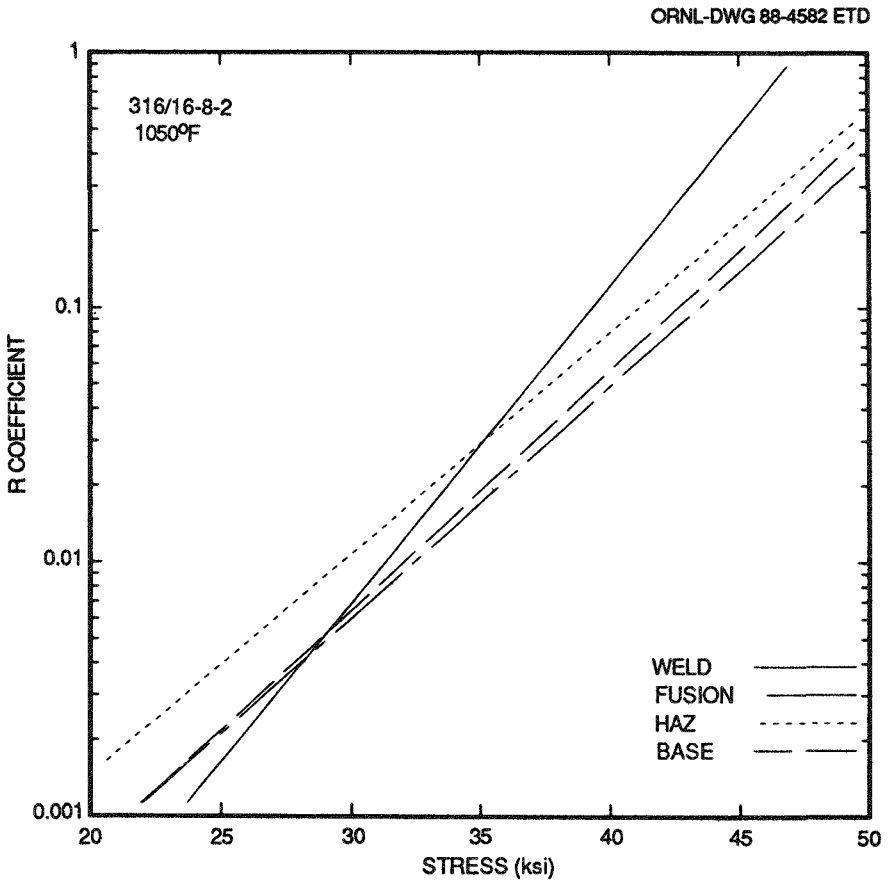


Fig. 28. Comparison of primary creep decay coefficient R(σ) for each zone (1 ksi = 6.895 MPa, 1050°F = 566°C).

summary of $C_3$ and $C_4$ is contained in Table 4. Figure 28 shows again that the weld material is unique from the other zones and that the HAZ and base curves are very similar.

The steady-state portion of the creep strain curve is more important than the primary portion because most of the creep strain is accumulated during the steady-state portion. Although the slope of the specimen creep strain curves had some variation dependent upon what time period was chosen, in general, the slope was well defined and not significantly different with time. The slope of each specimen creep strain curve was determined as shown in Fig. 24 and then plotted as a funtion of stress level. Figure 29 compares the least-squares fit of Eq. (1*c*) to the specimen data; a very good fit to these data is indicated. Figure 30

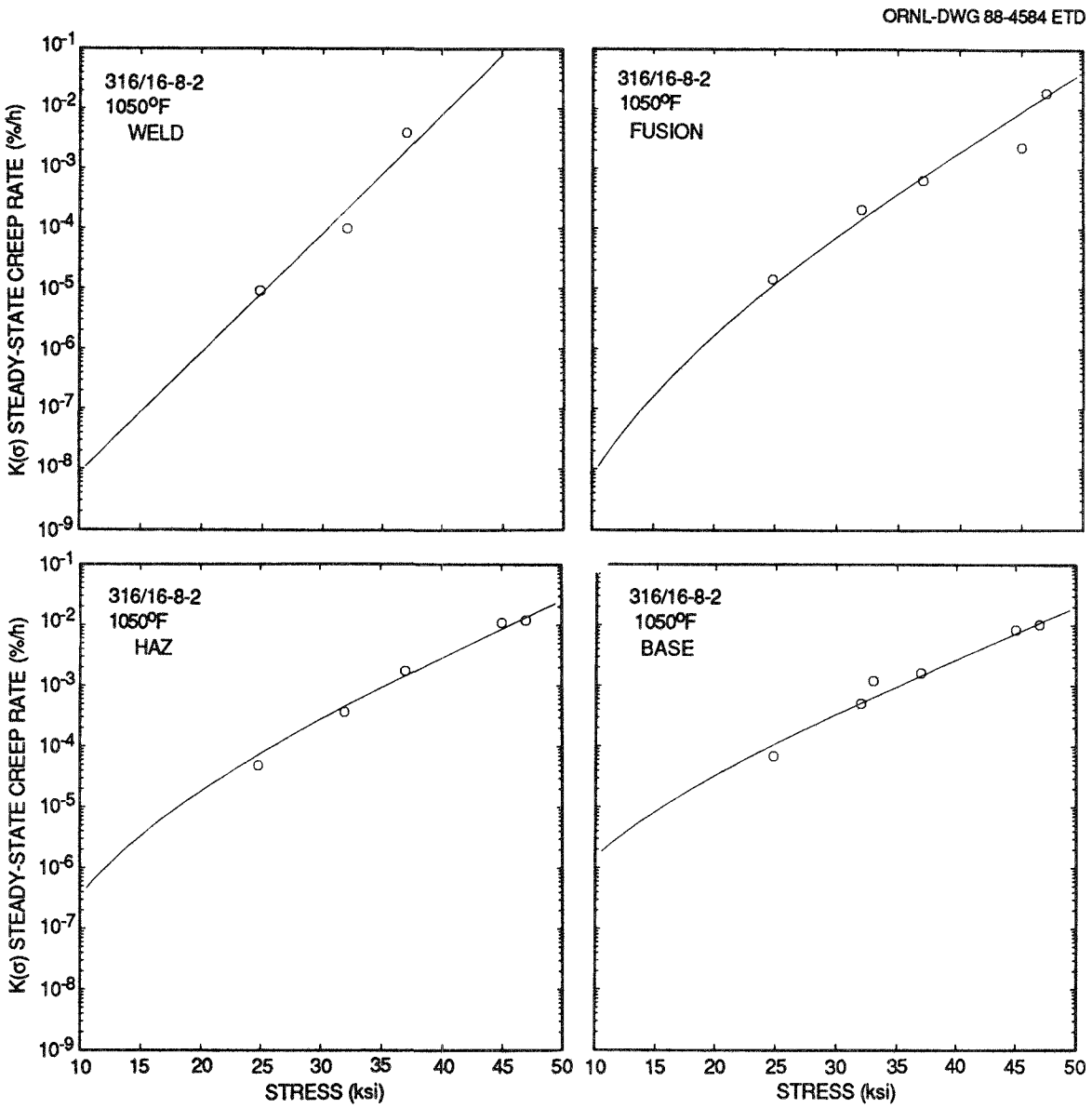


Fig. 29. Steady-state creep rate coefficients fit to specimen data (1 ksi = 6.895 MPa, 1050°F = 566°C).

presents a comparison of the creep equations for each weldment zone and indicates a crossover at around 241 MPa (35 ksi) so that while weld metal would creep at a relatively slow rate for low stress values, it would have a relatively higher creep rate at high stress levels. For the longitudinal weldment structures, this phenomena had a large influence on the load distribution between structural zones. Table 4 summarizes the values of $C_5$, $C_6$, and $C_7$ used to plot the curves in Fig. 30.

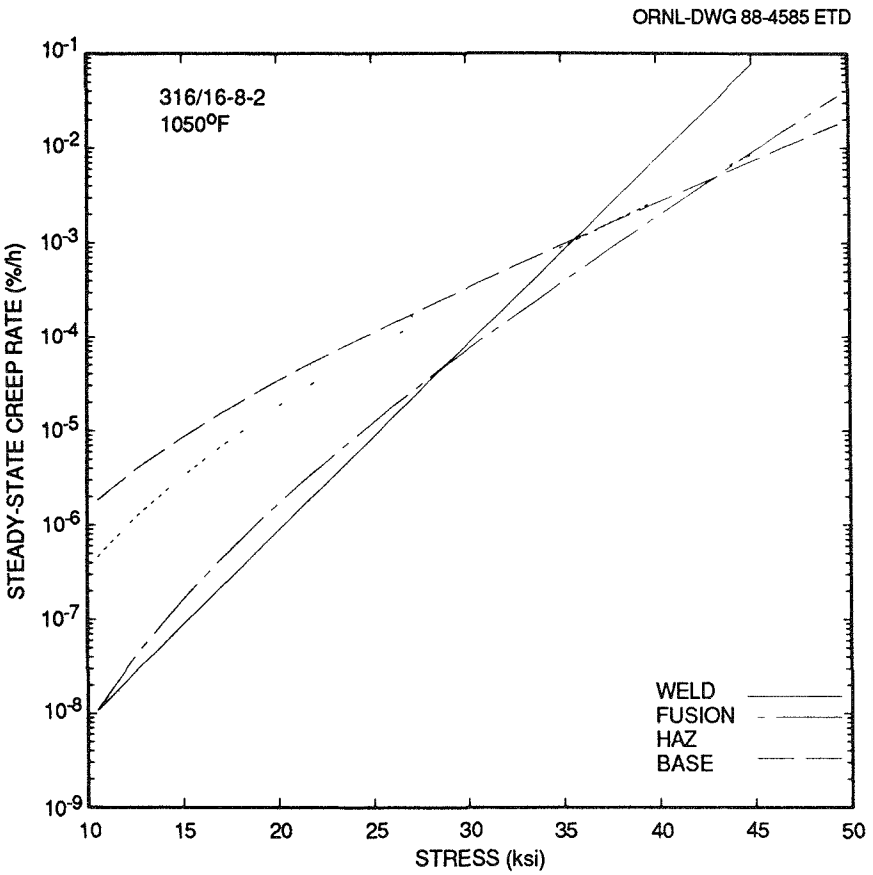


Fig. 30. Comparison of steady-state creep rate equations for each structural zone (1 ksi = 6.895 MPa, 1050°F = 566°C).

### 4.3.4 Creep-rupture representations

Time to rupture was recorded for each specimen and plotted for each structural zone. As previously mentioned, the linear damage evaluation was used in the weldment analyses, with creep damage being calculated from the following:

$$D_C = \int_0^t \frac{dt}{t_r} = \sum \frac{\Delta t}{t_r(\sigma)} \quad , \tag{2}$$

where $\Delta t$ is the increment of time that the structural zone is subjected to a given stress level. Thus, the rupture time to stress relationship was required to evaluate the creep damage.

Figure 31 gives a plot of each set of rupture data, and the near linearity of the data on the log log plot suggested that a power law representation would be best for the relationship. The curves in Fig. 31

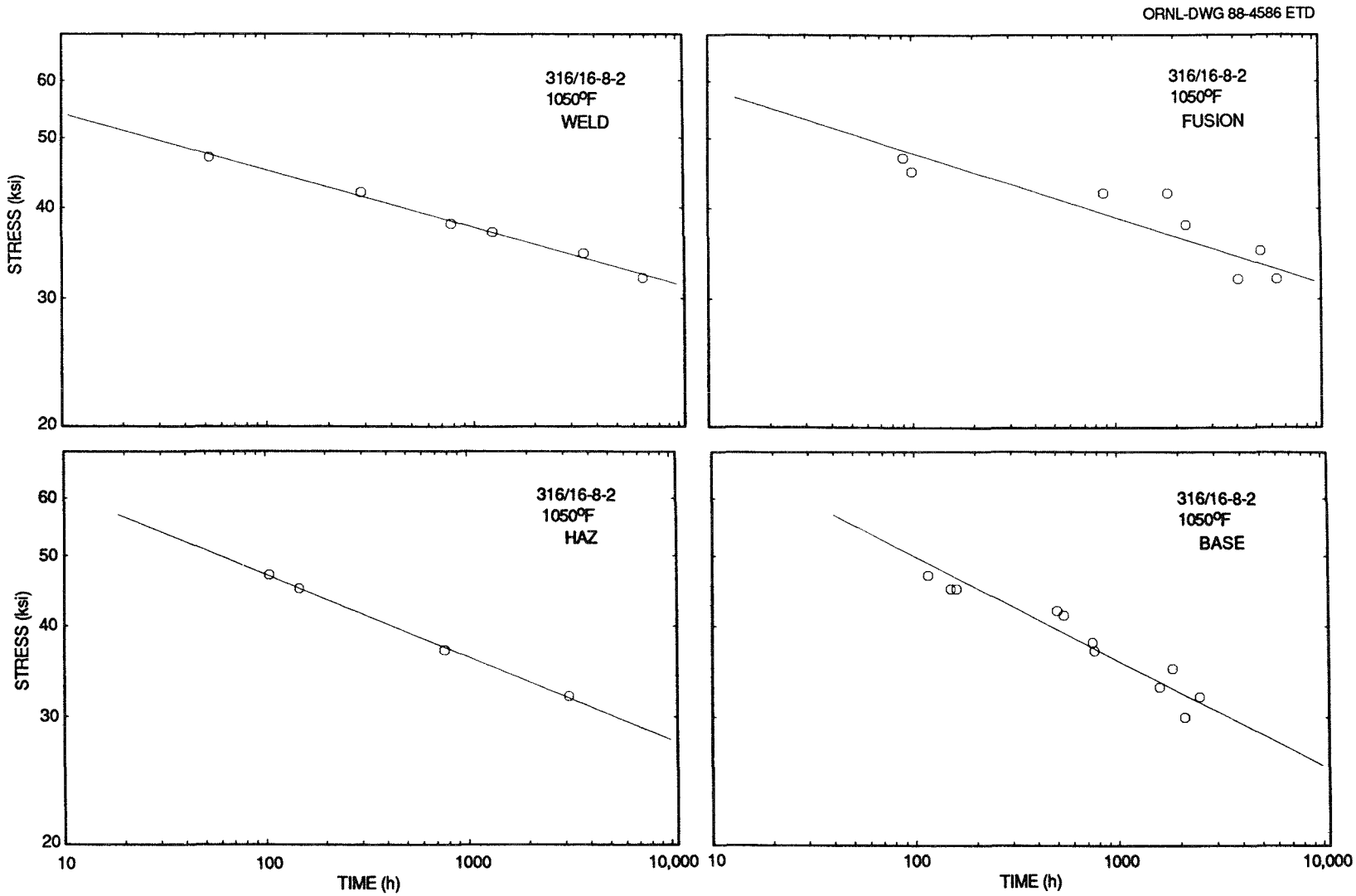


Fig. 31. Creep-rupture curves fit to specimen data (1 ksi = 6.895 MPa, 1050°F = 566°C).

are of the following form:

$$t_r = K\,\sigma^b \,, \tag{3}$$

or

$$\sigma = \left(\frac{t_r}{K}\right)^{1/b} \,.$$

Table 5 provides K and b for each zone, and Fig. 32 provides a comparison

Table 5. Creep damage equation constitutive equation coefficients [see Eq. (3)]

| Structural zone | K | b |
|---|---|---|
| Weld | 1.0328E23 | −12.705 |
| Fusion line | 8.4669E20 | −11.273 |
| HAZ | 5.5748E16 | −8.8176 |
| Base metal | 6.5415E13 | −6.9589 |

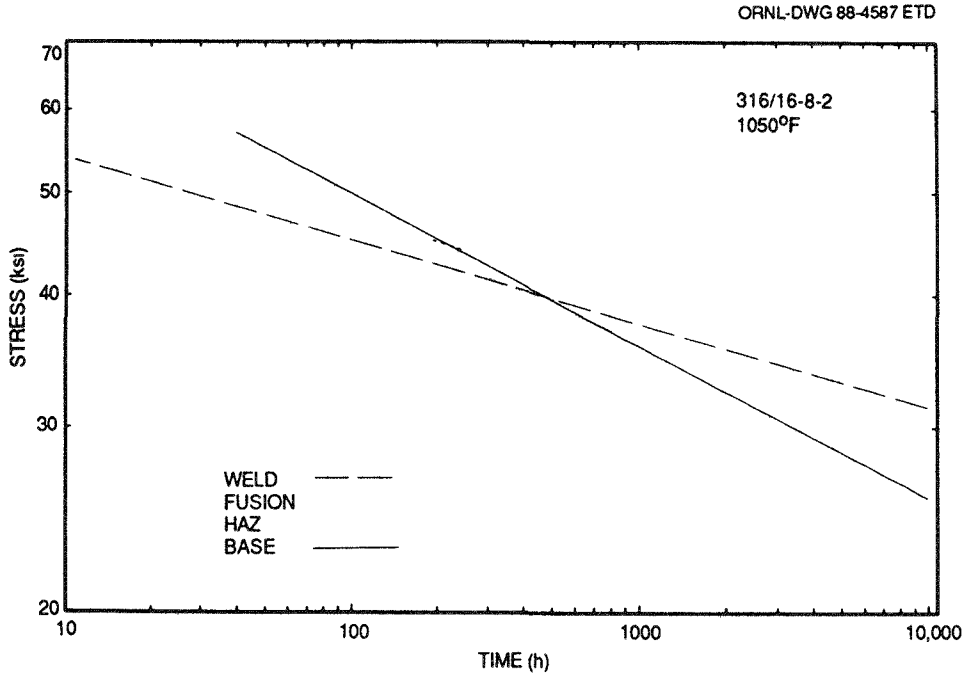


Fig. 32. Creep-rupture curves for each structural zone (1 ksi = 6.895 MPa, 1050°F = 566°C).

of these relationships. Again, the base and HAZ are more nearly the same, as are the weld and fusion line properties.

## 4.4 Finite-Element Code and Models

The inelastic structural analyses of the four weldment specimens were performed with the ORNL in-house research finite-element program, PLACRE,[23] which carries out creep calculations by an incremental initial strain method and plastic calculations by an iterative tangent stiffness method. This code provides an element library for detail modeling of one- and two-dimensional plane stress, generalized plane strain, and axisymmetrical structural problems. In addition, it has built-in convergent tolerance limits during iterative-incremental solution processes to relieve the user's burden of choosing proper values by trial-and-error. For large, complicated analyses, some of the convergent constraints can be relaxed by manual input for reducing computer time and costs.

### 4.4.1 Plate model

The analysis procedures used were those specified in NE standard F 9-5T (Ref. 20). The large deformation capability[24] of the computer code PLACRE was used to capture the nonlinear strain behavior of the specimen at the large deformations that were accumulated. For the analysis of WPCT-5 and -7, the experience gained with the 304 stainless steel plate analyses[11] was used to select a four-element model to represent adequately the various zones of material. A three-node constant strain rectangular element was used as illustrated in Fig. 33. This element provided a two-dimensional plane stress solution with the x-y plane being the plane of the plate.

The four-zone weldment model contained zones for the weld metal, the fusion line metal, the HAZ, and the base metal, as described in Sect. 4.3.1. The material characterization equation and coefficients presented in Sect. 4.3 were used in the PLACRE analysis to determine the appropriate stress distribution in each weldment zone and accounted for the differences in elastic, plastic, and creep characteristics of each zone at

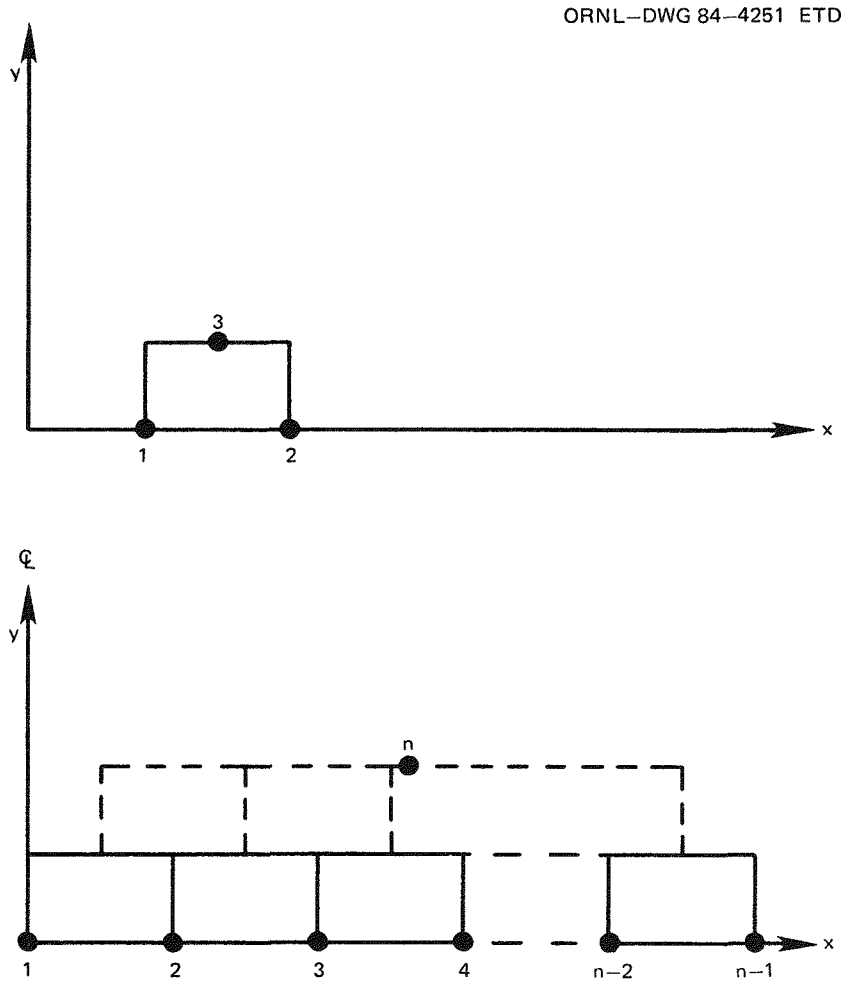


Fig. 33. Illustration of three-node element type and arrangement of elements used to model the long plate structures.

the test temperature and load level. These differences in zone properties caused a redistribution of load on each zone so that the strain of the four zones would be the same. Strains for each phase of the loading were predicted and are presented in Sect. 6.1.1 for the plate tests.

### 4.4.2 Cylinder model

Because of geometrical symmetry, only a portion of the test specimen section, from the centerline of the weld metal to the center of a base metal section, was modeled as shown in Fig. 34. The model consisted of 663 nodes and 1164 3-node constant strain-ring elements. The nodal

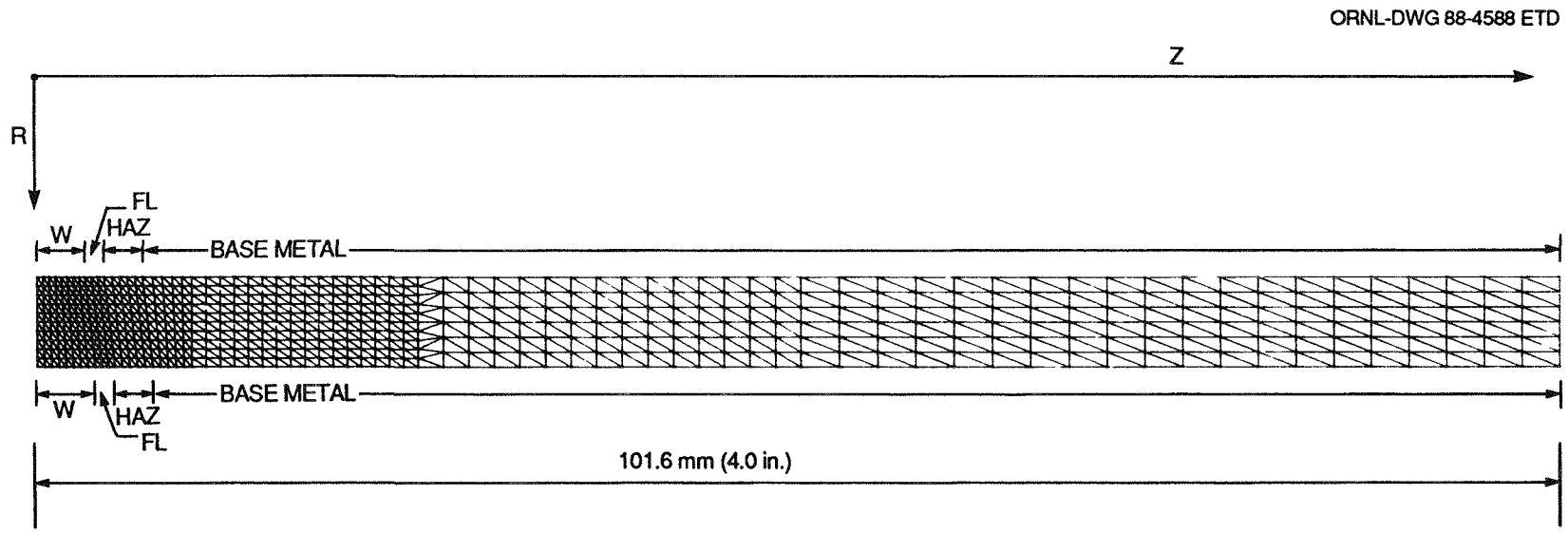


Fig. 34. Finite-element model for WCCT-1 and -2 tube weldments showing boundaries of various zones.

points on the Z = 0 boundary were fixed, but free radial displacements were allowed. The nodes at the right end boundary were constrained to have the same longitudinal displacement Z with no rotation permitted.

A word of caution must be raised concerning the cylinder analyses. In a previous ORNL study of dissimilar metal weldments, an elastic singularity or near singularity was found on the cylinder surface at the junction of dissimilar property zones.[25,26] As the finite-element mesh was made smaller and smaller, the calculated stresses grew correspondingly larger. The previous study was concerned with thermal loadings. The extent to which the present analyses, which involve plasticity and creep and no thermal loads, might be affected, if at all, has not been investigated.

# 5. SUMMARY OF TEST RESULTS

The observed times to various stages of specimen cracking are summarized in Table 6 for all four tests. These stages are (1) first cracks, (2) visible 790-μm (0.031-in.) cracks, and (3) final rupture. The rupture times are direct measurements, whereas most of the remaining times are derived by various interpolation techniques from the results of the periodic crack inspections. These data points are our best estimates.

Table 6. Time (h) to cracking and rupture for the four structural weldment tests[a]

| | WPCT-5 | WPCT-7 | WCCT-1 | WCCT-2 |
|---|---|---|---|---|
| First cracks | | | 552 (HAZ) | 502 (HAZ) |
| 1/32-in. crack[b] | 860 (FL/HAZ) | <10,400 (FL/HAZ) | 776 (HAZ)[c] | 2,015 (HAZ)[c] |
| Rupture | 7,190 | | 1,022 (BM) | 8,384 (BM) |

[a]Location of cracks on ruptures are denoted in parentheses.

[b]Visible cracking was somewhat arbitrarily defined as a crack 1/32 in. (790 μm) long.

[c]Unaffected base metal regions were not inspected at or before these times.

Figure 35 shows the cracking pattern that had developed after 1900 h in the WPCT-5 test. This photograph and the results of the 1190-h inspection reveal cracks in the base metal originating in the fusion zone and oriented perpendicular to the weld–base metal interface. The average crack length in the gage length region after 1190 h of testing was ~1.35 mm (0.0531 in.). With successive inspections, the rate of crack growth (length) decreased with increasing time, indicating that the cracks tend to relieve the locally high stresses. The width of the cracks and the number of cracks, however, increased with accumulated time and axial strain. Also, new cracks appeared progressively along the tapered section of the specimen with increasing test duration. The crack size and crack density decreased with increasing cross-sectional area (decreasing stress) in the taper areas. Gross macrocracking was observed all along the weld–base metal interface zone by the time of the inspection at 6965 h (Fig. 36). Rupture occurred near one end of the reduced test section (see Fig. 36) after 7190 h of testing.

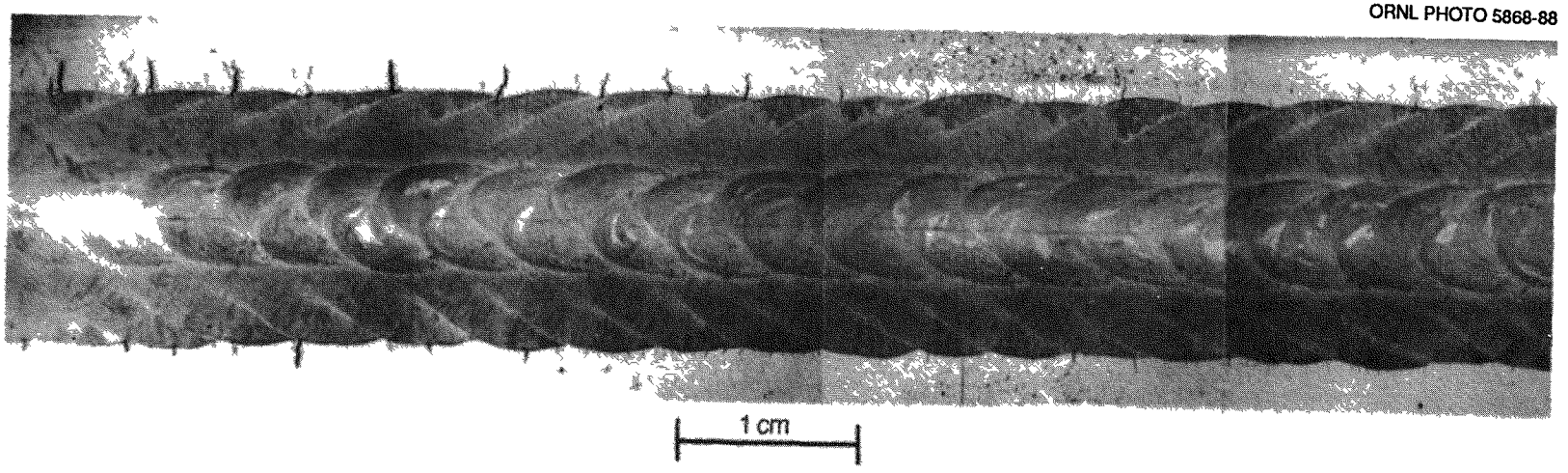


Fig. 35. Results from surface replication of specimen WPCT-5 after 1955 h of testing.

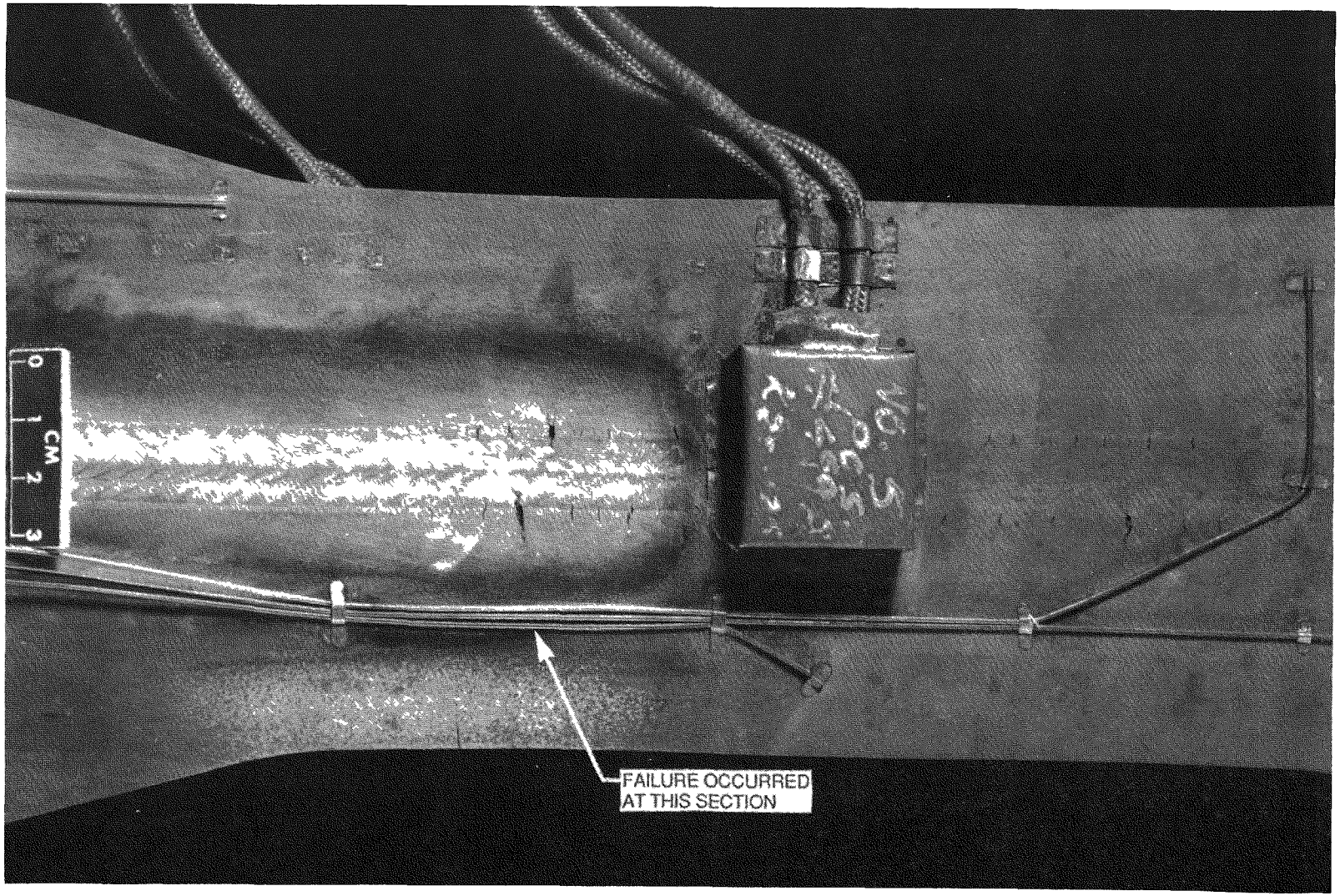


Fig. 36. Surface of plate weldment specimen WPCT-5 after 6965 h of testing.

The weldment plate creep test WPCT-7 displayed a similar, but much less extensive, cracking pattern by the end of the 10,400-h test (see Fig. 37). Two macrocracks, both 6.22 mm (0.245 in.) long, developed at one end of the gage length. These two cracks do not appear to be representative of the entire specimen gage length and thus may be caused by extraneous factors [bending moment applied to the specimen when the grips broke, repair process after grip breakage, a weld flaw (porosity) at that point, or a region of increased stress caused by the geometry width transition]. The much more uniform crack pattern along the length of the weld had an average crack length of ~1370 μm (0.054 in.). Therefore, the time to visible cracking [790 μm (0.031 in.)] is less than the 10,400 h listed in Table 6. The lack of any inspection between 9,400 and 10,400 h of testing to assess crack growth prevents making a more quantitative estimate of the time to visible cracking.

Cracking in the HAZ was detected at the first inspection of the WCCT-1 test. These cracks averaged 100 μm (0.004 in.) long after 552 h of testing. The HAZ cracks had grown to lengths of 760 μm (0.030 in.) by the 766-h inspection (see Fig. 38). The specimen broke in the base metal near the beginning of the transition region at one end of the uniform thickness gage length after 1022 h of testing.

A plot of the circumferential HAZ crack growth vs time for weld "C" (see Fig. 11) of the WCCT-2 specimen is shown in Fig. 39. Cracking in the HAZ was detected during the first inspection at 502 h. The crack length of 100 μm (0.004 in.) did not change appreciably with inspections at 1003 and 2010 h. Crack width increased slightly, revealing more defined cracks. The crack length increased to more than 400 μm (0.016 in.) by the inspection at 3986 h and to more than 510 μm (0.020 in.) by the inspection at 8085 h (see Fig. 40). Circumferential cracks in the weld-metal were 130 μm (0.005 in.) long at this last inspection.

Posttest examination revealed cracking in the HAZ of all three welds of WCCT-2, and in fact, cracking was more extensive in weld "A." Figure 41 shows a crack originating in the outside surface of the HAZ and propagating almost through the thickness. Figure 42 shows the final rupture of WCCT-2 after 8384 h of testing. The rupture location was ~6.99 cm

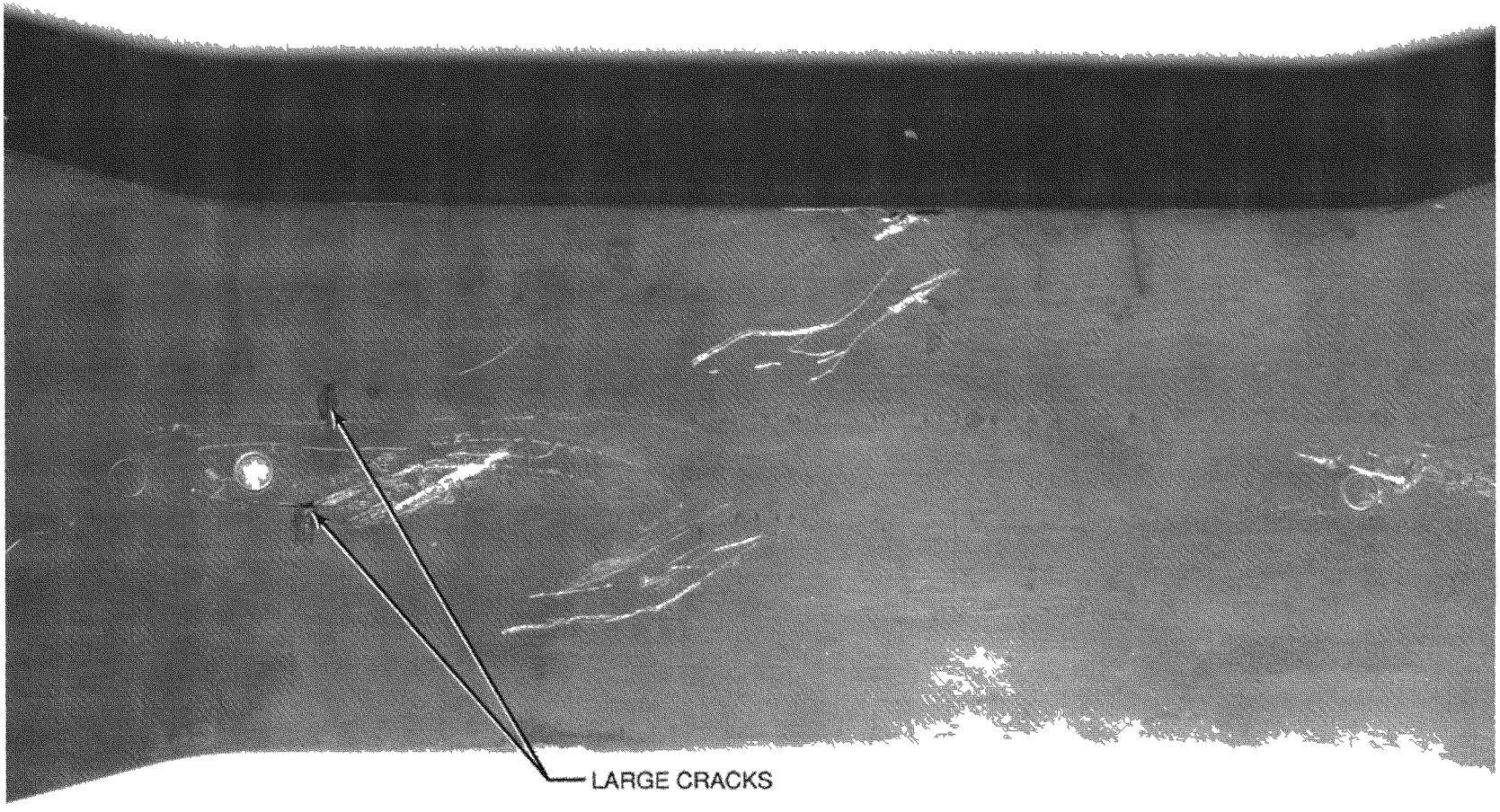


Fig. 37. Surface of plate weldment specimen WPCT-7 after 10,400 h of testing.

M&C Photo Y200657

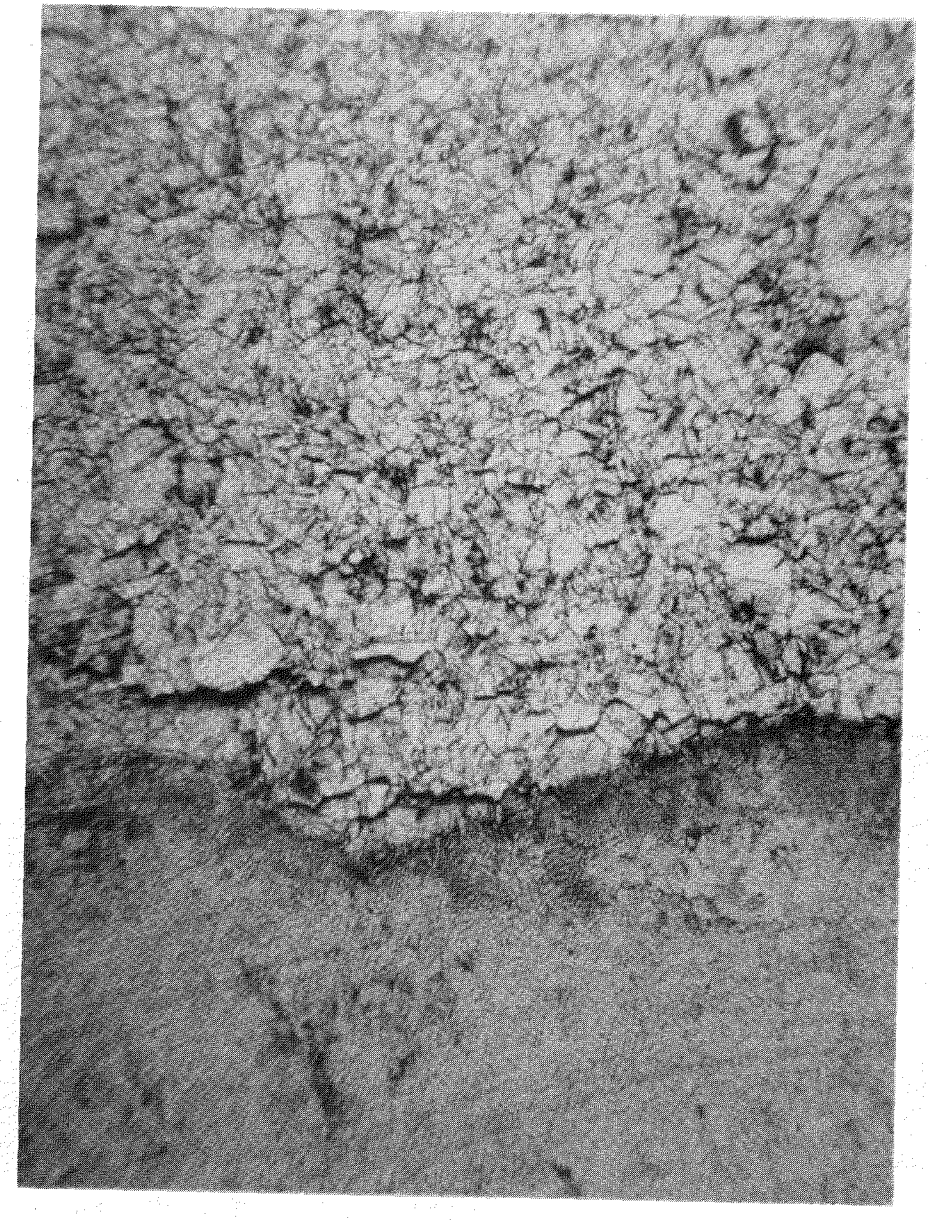

Fig. 38. Results from the surface replica inspection of specimen WCCT-1 after 766 h of testing.

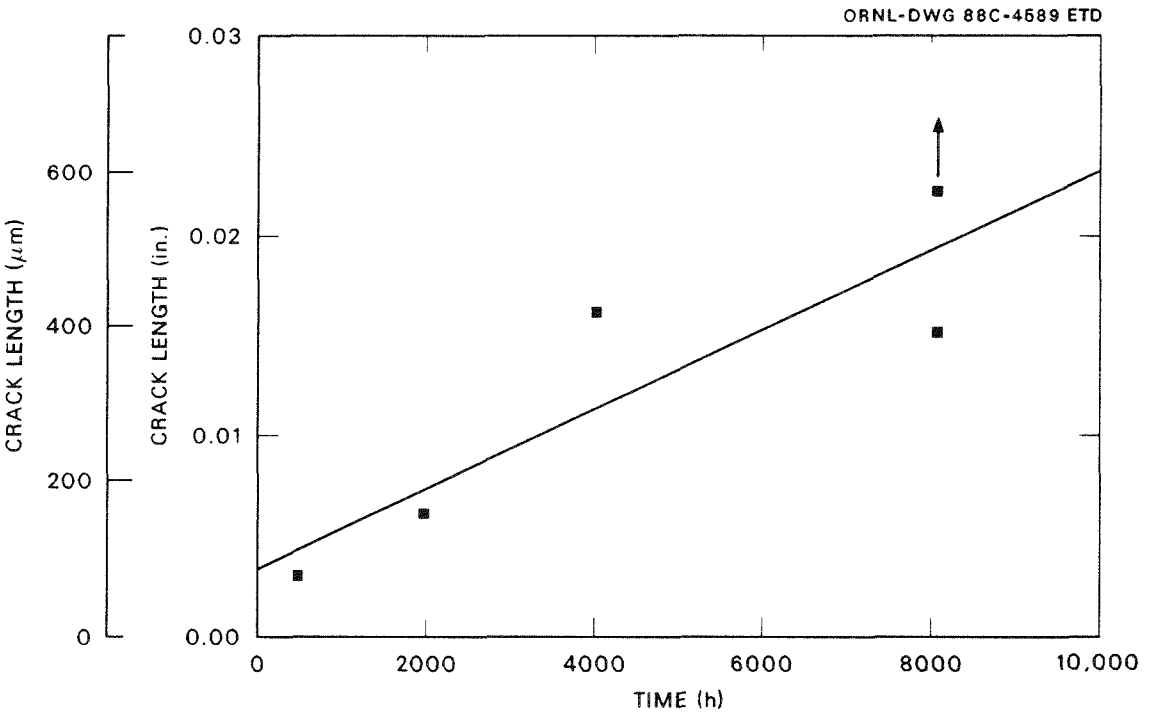


Fig. 39. Circumferential HAZ crack-growth results for weld "C" of specimen WCCT-2.

(2.75 in.) from the beginning of the radius at one end of the gage length of the specimen.

The creep-rupture curves of stress vs time for the base metal, HAZ, fusion line, and weld metal for the test specimen welds are plotted in Fig. 43, along with the Code Case N-47 minimum expected base-metal creep-rupture strength, ($\sigma_{rmin}$); weld-metal strength ($\sigma_{rmin} \times R$); and allowable stress, $S_t$. The points of visible cracking and rupture for the four structural tests are then shown superposed on these curves. Note that all of the visible cracking points and one of the rupture points falls below the curves for the individual component materials, illustrating the metallurgical notch effect of the weld. Table 7 provides the ratios of the predicted base metal rupture times, from Fig. 43, to the observed visible cracking and rupture times of the four structural test specimens.

The Code $S_t$ curve is well below the observed points of initial cracking. In this case, the R ratios are not sufficiently low to affect the $S_t$ curve in the region shown. Thus the $S_t$ curve shown in Fig. 43 would govern both base metal and weldment.

M&C Photo Y209394

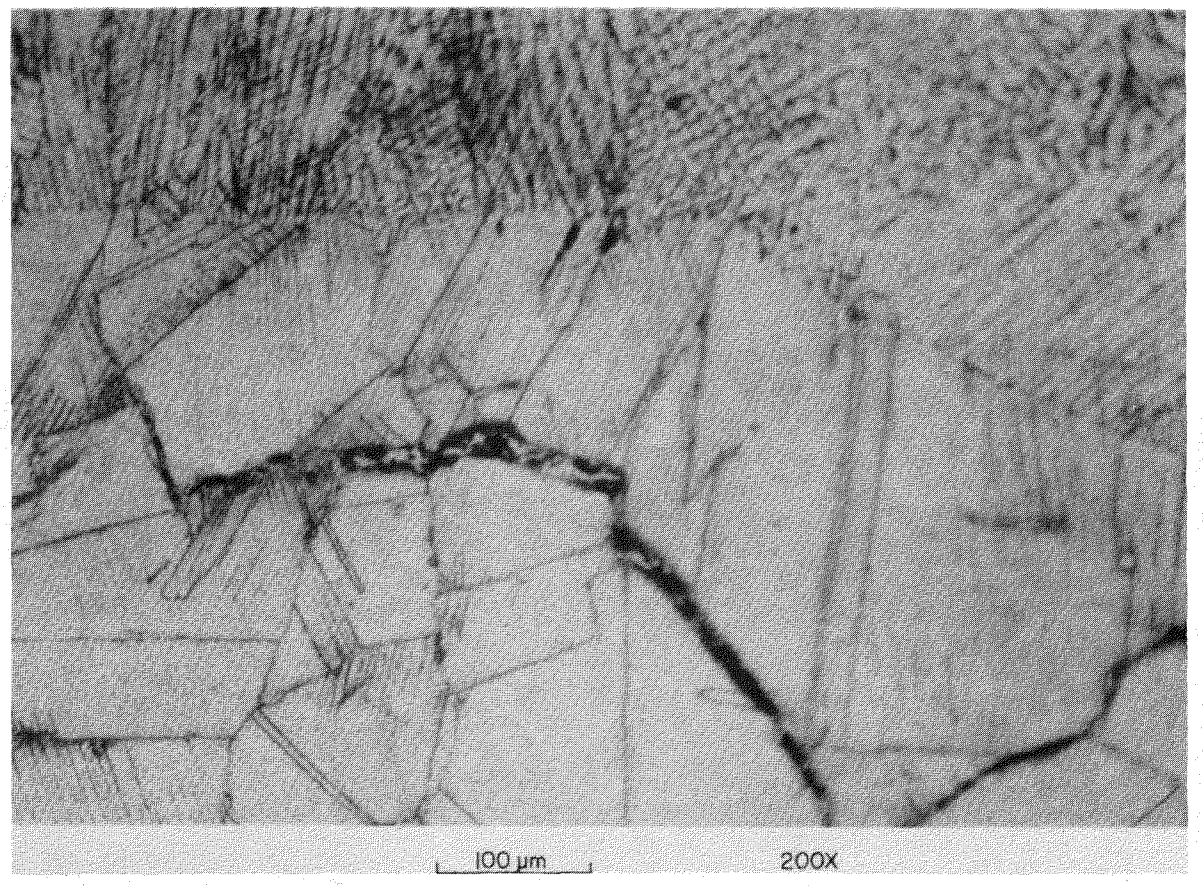


Fig. 40. Circumferential crack in the HAZ of weld "C" of specimen WCCT-2 after 8085 h of testing.

Table 7. Ratios of the predicted base metal rupture times to weldment visible cracking and rupture times

| | Visible cracking | Rupture |
|---|---|---|
| WCPT-5 | 2.2 | 0.26 |
| WCPT-7 | ≥1.0 | |
| WCCT-1 | 2.6 | 1.8 |
| WCCT-2 | 2.2 | 0.52 |

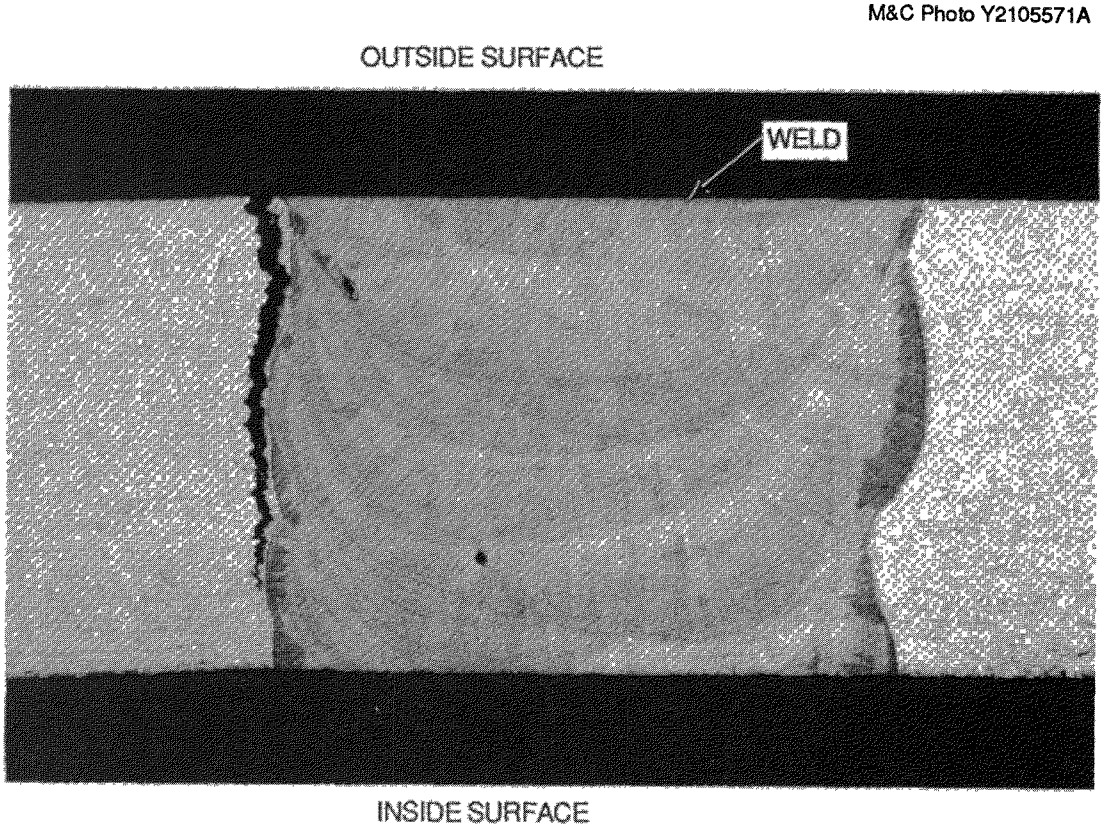


Fig. 41. Posttest examination results of through-the-wall crack of weld "A" of specimen WCCT-2.

ORNL PHOTO 8874-87

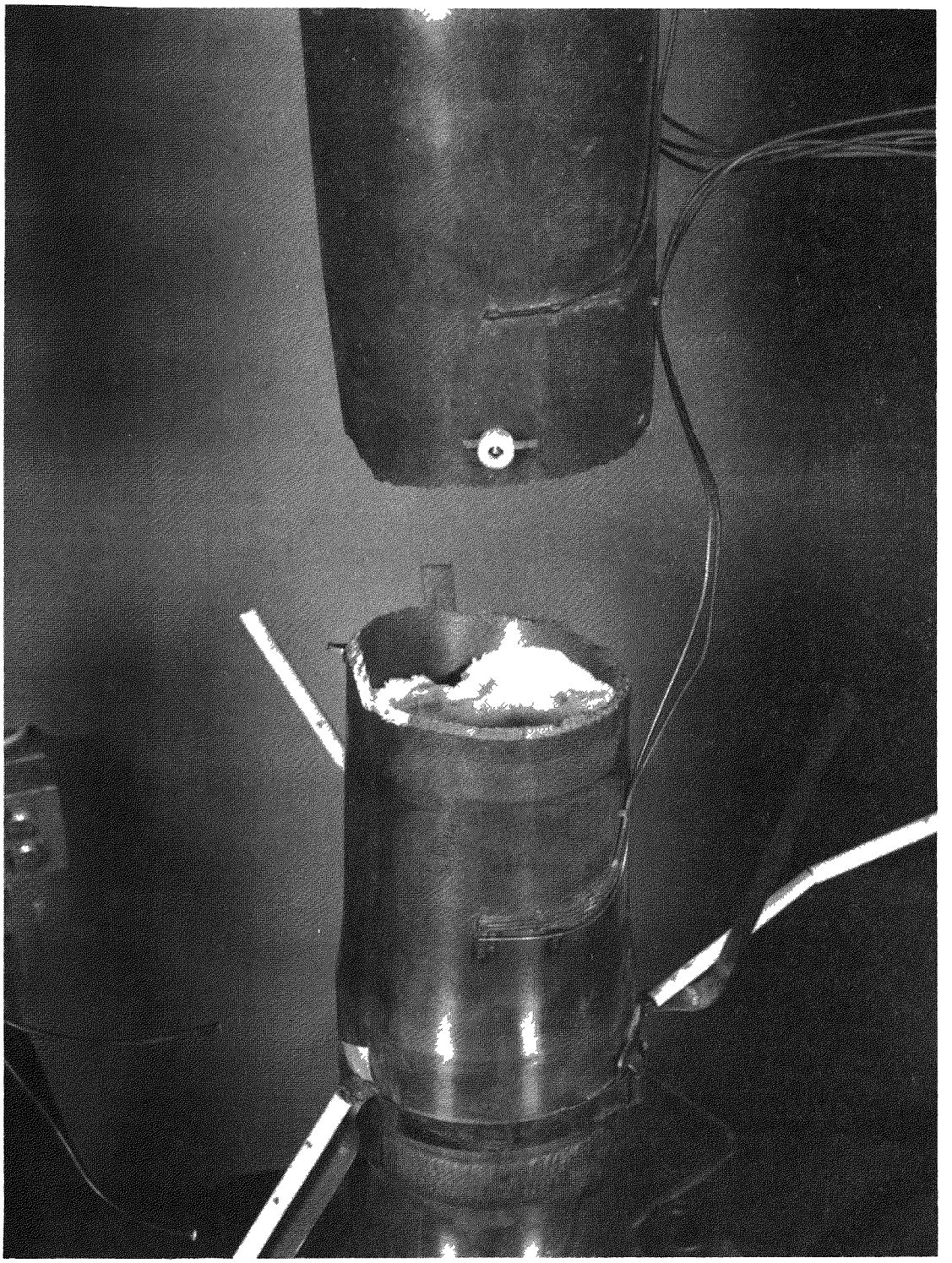

Fig. 42. Creep-rupture failure of welded cylinder specimen WCCT-2.

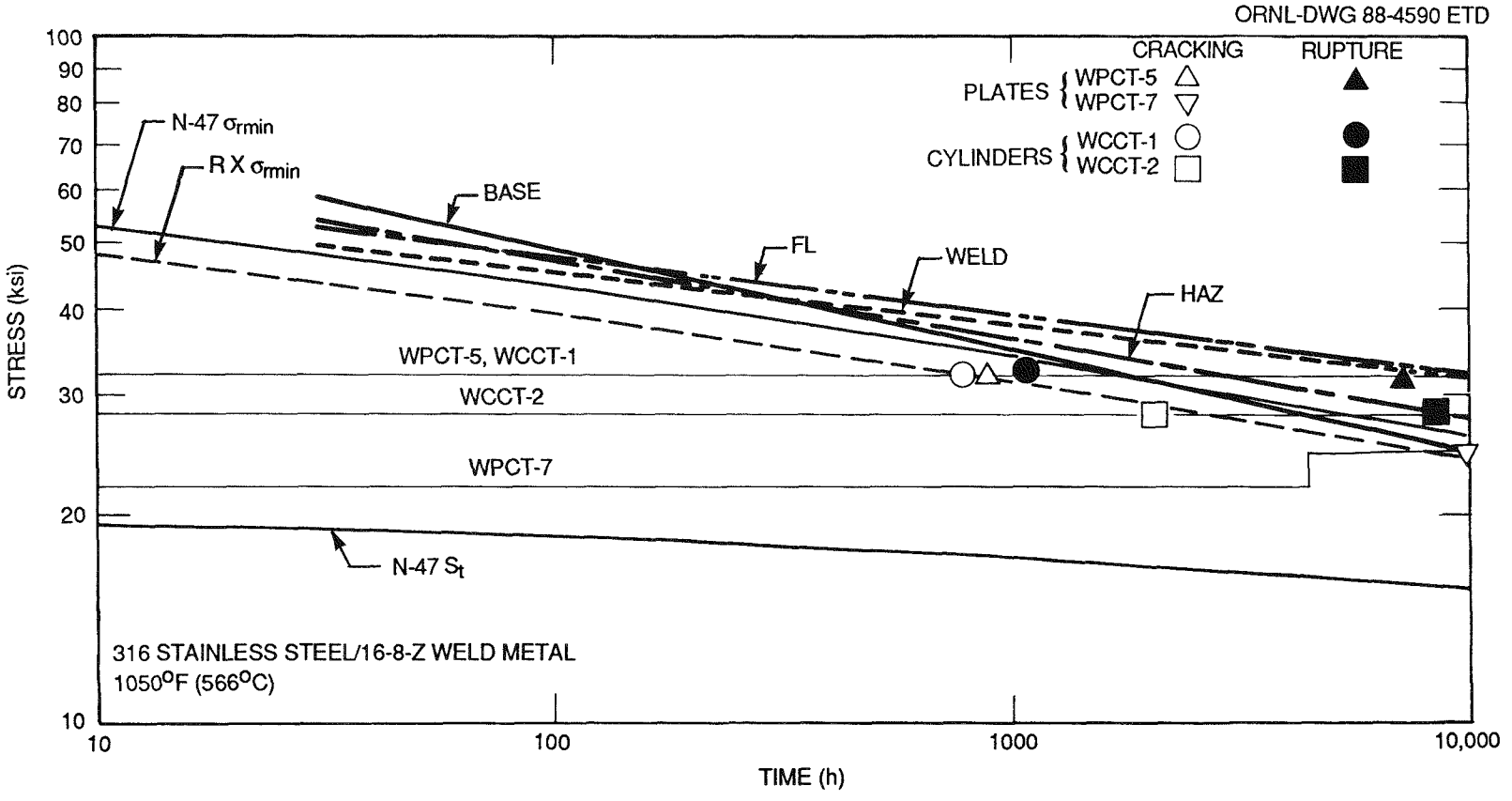


Fig. 43. Comparison of four sets of structural weldment test results with material rupture curves and Code Case N-47 allowables (1 ksi = 6.895 MPa).

# 6. COMPARISON OF TEST RESULTS WITH PREDICTIONS

## 6.1 Measured and Predicted Strains

### 6.1.1 Plate specimens

The inelastic model was used to predict the strains during the initial load-up phase when the response would be expected to be elastic-plastic only (no creep). Figure 44 shows a comparison between the predicted and measured initial loading results for WPCT-5. The bilinear

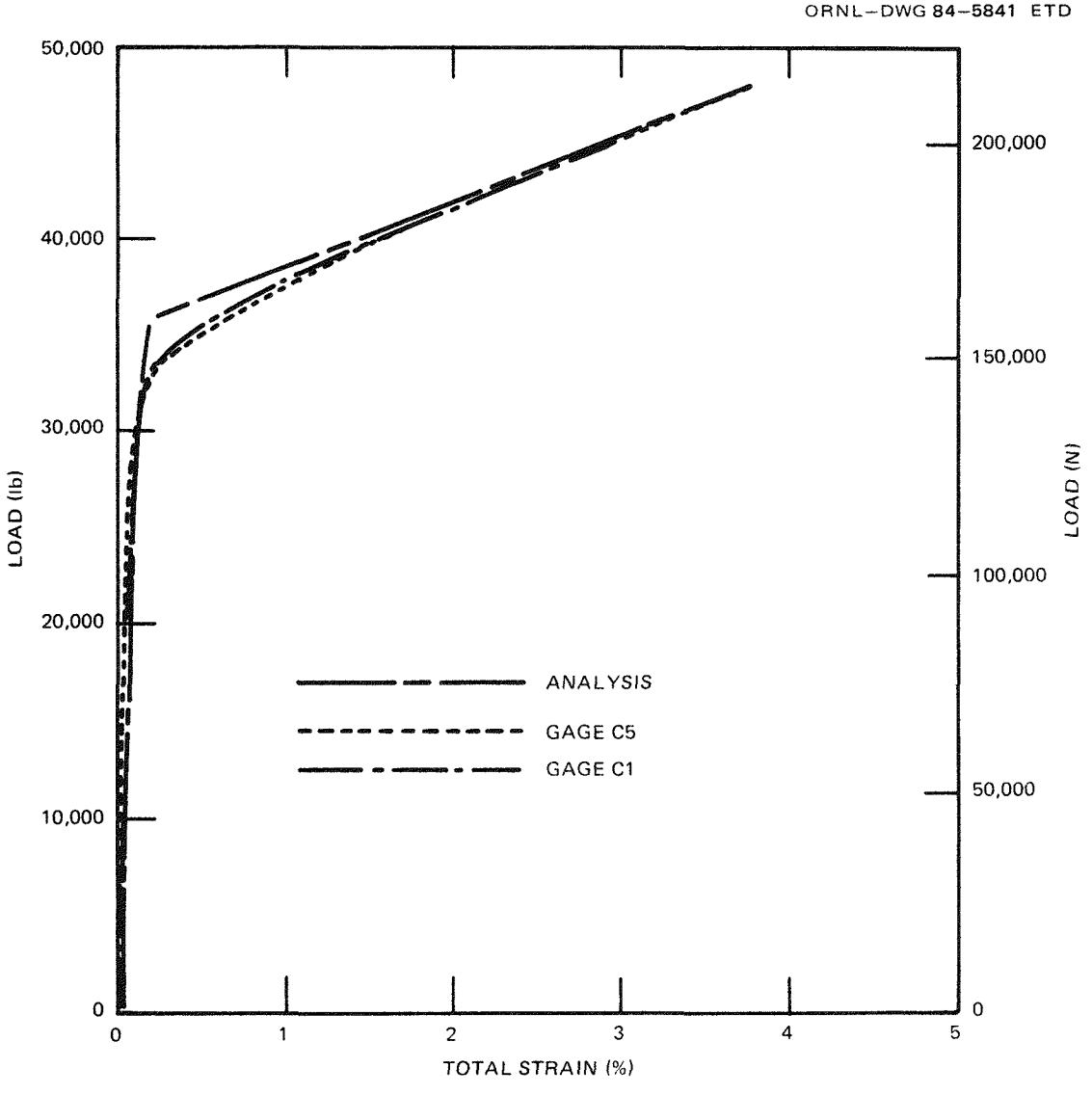


Fig. 44. Comparison of predicted and measured load vs total strain of WPCT-5 for initial load-up phase.

model gives excellent correlation with the measured results near the end of this loading phase, even though the weldment zones had large differences in the deformation properties. The total predicted longitudinal strain time history, including the elastic-plastic deformation of the previous plot, is compared with the experimental results for WPCT-5 in Fig. 45. This figure shows good correlation between test and analysis for the first 4000 h, at which time the test data show an unexplained divergence. However, at the test conclusion, after nearly 7000 h, the predicted and measured results were still within 10% of one another. The total transverse strain predictions are compared in Fig. 46 with the results of the single transverse strain gage available on WPCT-5. While the test showed more primary strain, the overall comparison of transverse strain is considered to be good.

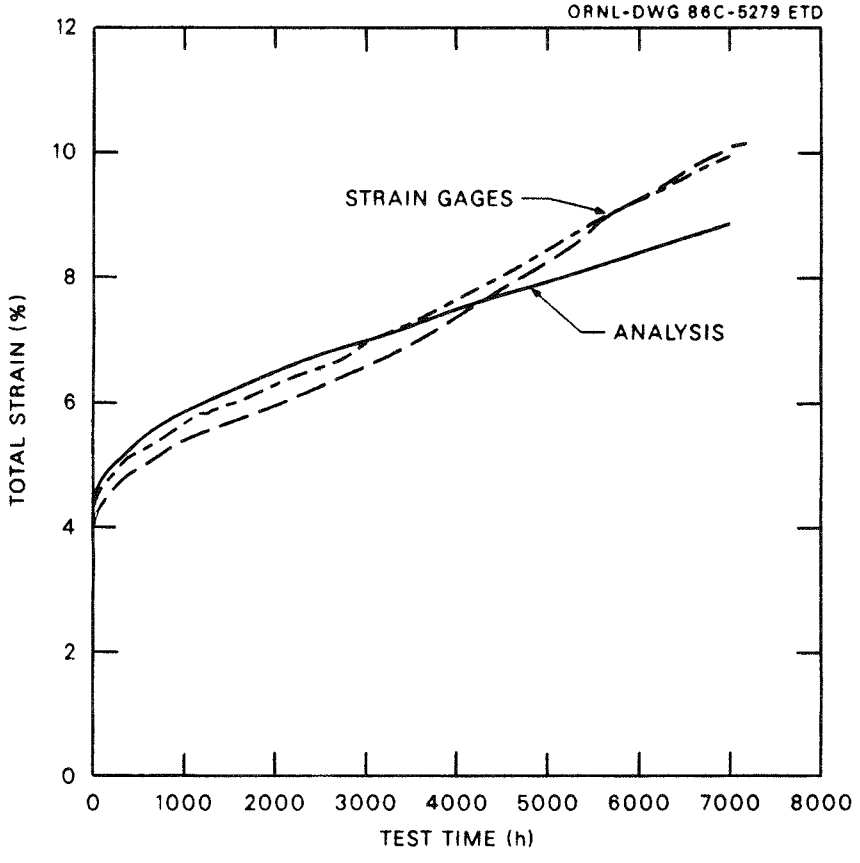


Fig. 45. Comparison of predicted and measured total axial strain for welded plate creep-rupture test WPCT-5.

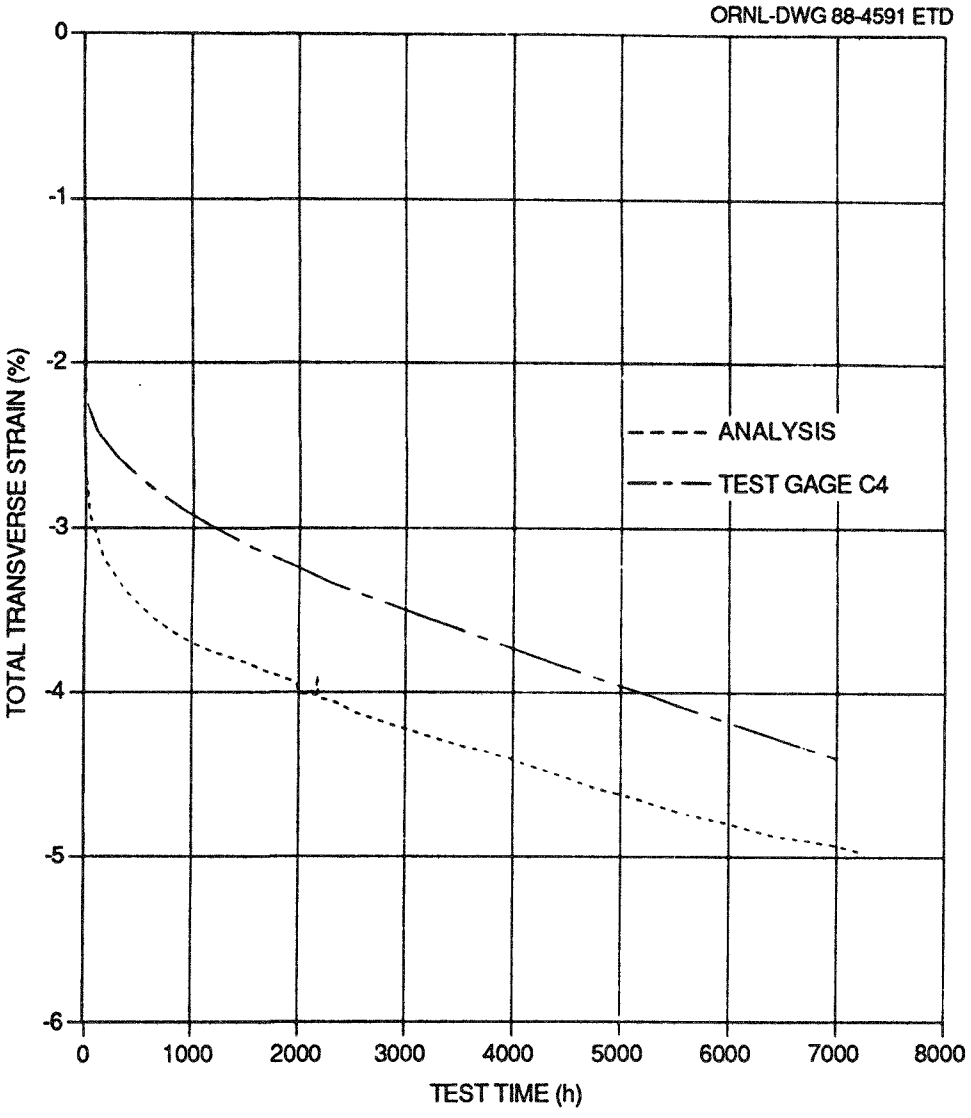


Fig. 46. Comparison of predicted and measured total transverse strain for welded plate creep-rupture test WPCT-5.

The initial loading and the transverse strains were not measured for plate test WPCT-7. Consequently, Fig. 47 shows only the creep strain comparison for this test. At about 4400 h the grips failed, requiring a rework of the test specimen as described in Sect. 3.2. The rework to a smaller cross section resulted in a larger percentage of weld material and consequently provided a different interaction between zones. Material properties identical to those used in the WPCT-5 analysis were used in the WPCT-7 analysis along with the original WPCT-7 cross-sectional

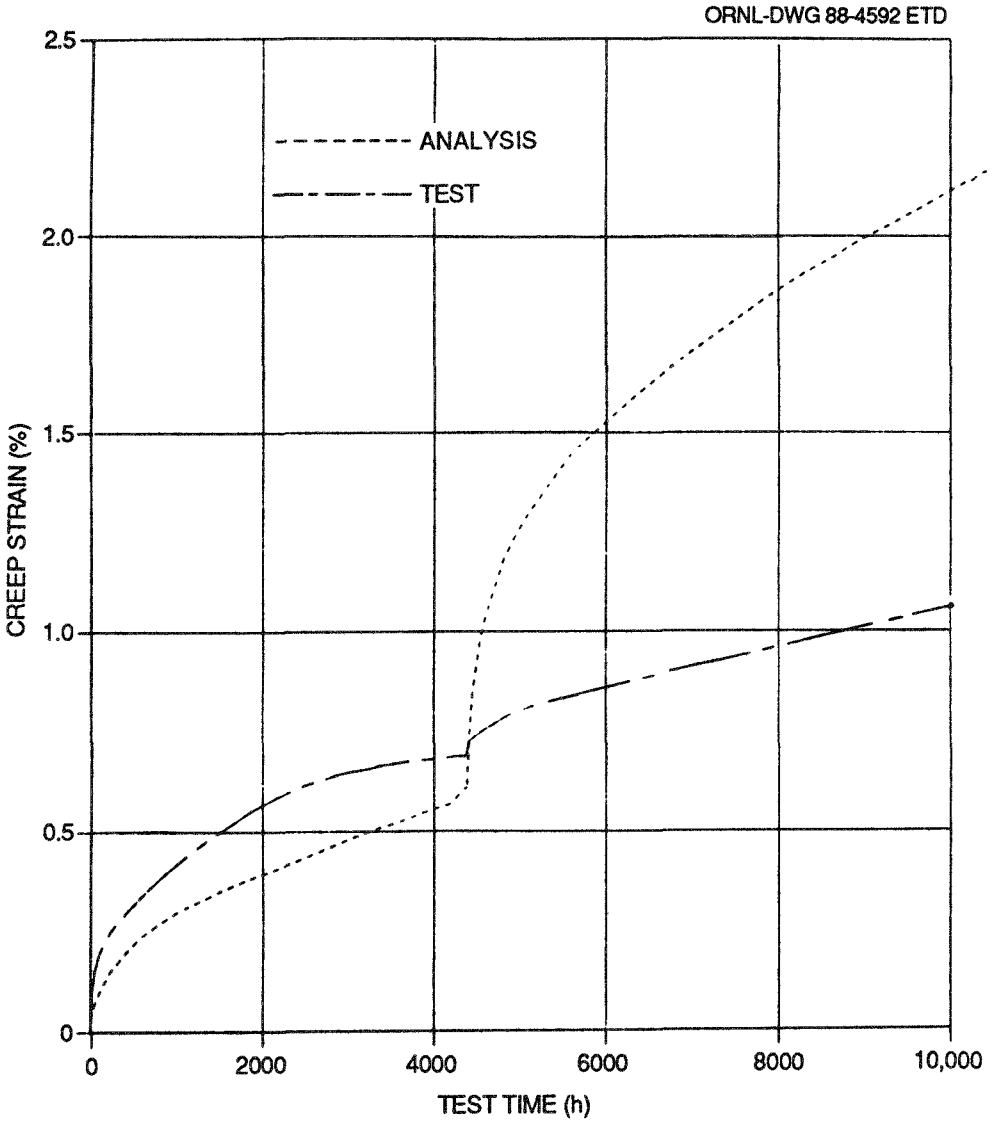


Fig. 47. Comparison of predicted and measured axial creep strain for weldment creep-rupture test WPCT-7.

area. Load changes were made analytically to represent the 152-MPa (22-ksi) stress for the first 4400 h and 171 MPa (24.8 ksi) for the last 6000 h. The analysis overpredicted the primary and secondary creep on the increased stress level compared with the test data. However, the test contained a larger percentage of weld material with lower creep characteristics. Also, a complex and severe bending load occurred on the test article during grip failure, and this event may have had an effect on subsequent response.

### 6.1.2 Cylinder specimens

The inelastic analyses for the cylinder weldment specimens, WCCT-1 and -2, followed the simplified (idealized) histograms shown in Figs. 48 and 49, respectively. The normal inspection shutdowns and reloadings

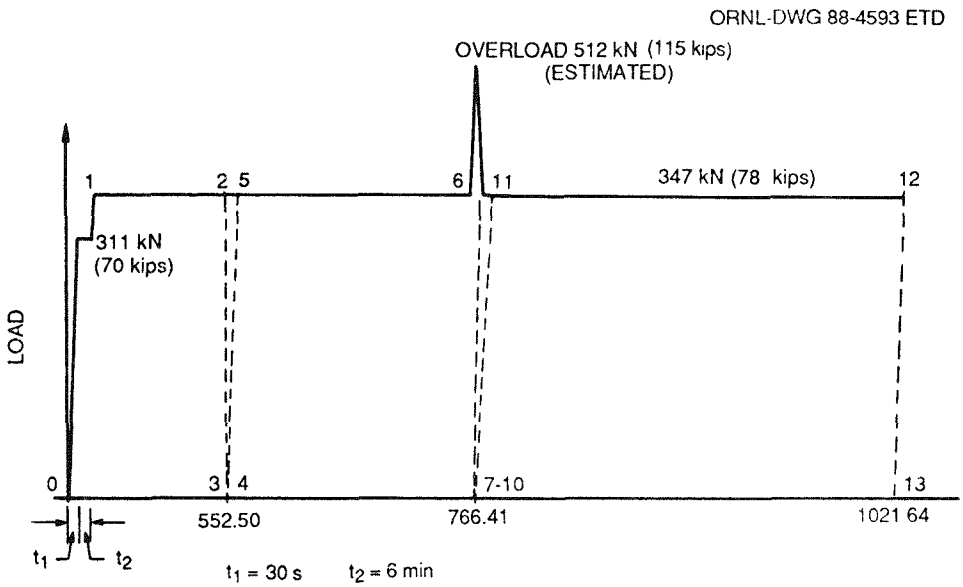


Fig. 48. Idealized histogram for WCCT-1. Dotted lines indicate inspection shutdowns and reloadings ignored in analysis.

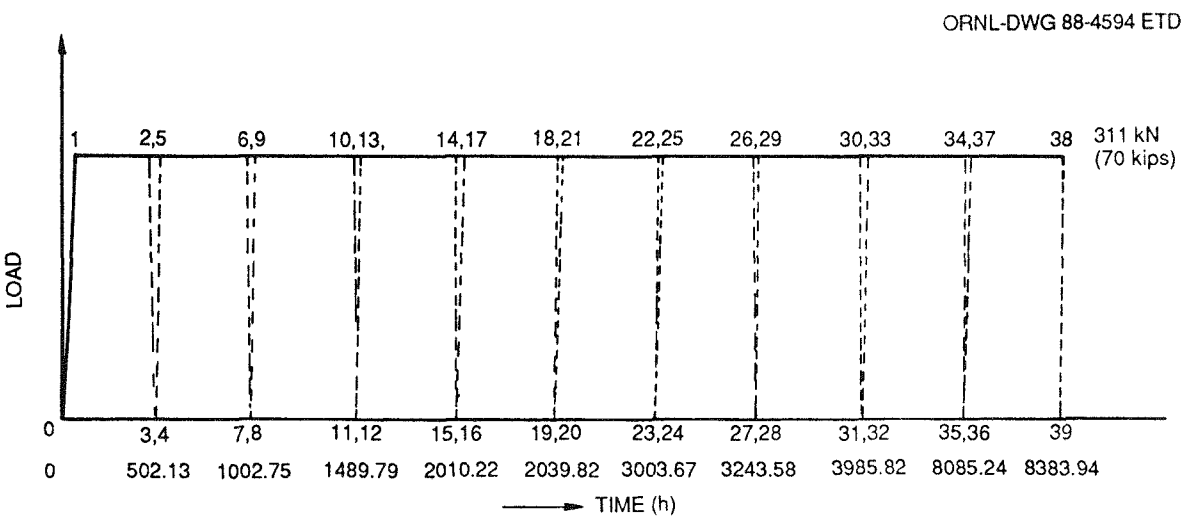


Fig. 49. Idealized histogram for WCCT-2. Dotted lines indicate normal inspection shutdowns and reloadings ignored in analysis (311 kN = 70 kips).

steps were ignored in the analyses. Recall that an accidental instantaneous overload occurred after histogram point 6 in the WCCT-1 test. The exact magnitude of the overload could not be determined. However, judging by the capacity of the loading apparatus, an overload to 512 kN (115.0 kips) was estimated and used in the analysis.

The analysis results indicate that the weldments developed significant plastic loading strains in the initial loadings. Figure 50 shows the measured and predicted initial loading strains in the various weldment zones for WCCT-1, while Fig. 51 shows these comparisons for specimen WCCT-2. All of the measured gage responses are shown in Figs. 50 and 51. Refer back to Fig. 15 for the gage locations. Gages AB2 and B4 were circumferential gages, and the signs have been reversed for these gages in the figures. The analysis results plotted in Figs. 50 and 51 are for finite-element grid points near the locations of the designated strain gages. Thus, for example, the analysis labeled B1 should be compared with the B1 gage result.

A maximum initial loading strain of 8% was recorded by gage B2, located in the fusion zone of WCCT-1. As can be seen from Fig. 50, the fusion line of WCCT-1 exhibited the most strain, then the base metal, followed by the weld metal, and finally the HAZ (the least strain). These results contradict what would be expected based on the material properties characterization test data. There the base metal exhibited the most creep strain, then the HAZ, weld metal, and fusion line. A plausible explanation of this discrepancy is the somewhat different manufacturing and welding processes used in the test specimen preparation.

For specimen WCCT-1, the predicted initial base metal loading axial strain (gage AB1) and circumferential strain (gage AB2) and the axial weld metal loading strain (B1) are in good agreement with the measured results. In other zones, the predicted initial loading strains are quite different from the experimental data, as indicated by the measured and predicted results for the HAZ (gages B3, A3).

The initial loading strain predictions for WCCT-2 are compared with the strain gage measurements in Fig. 51. Here the experimental results

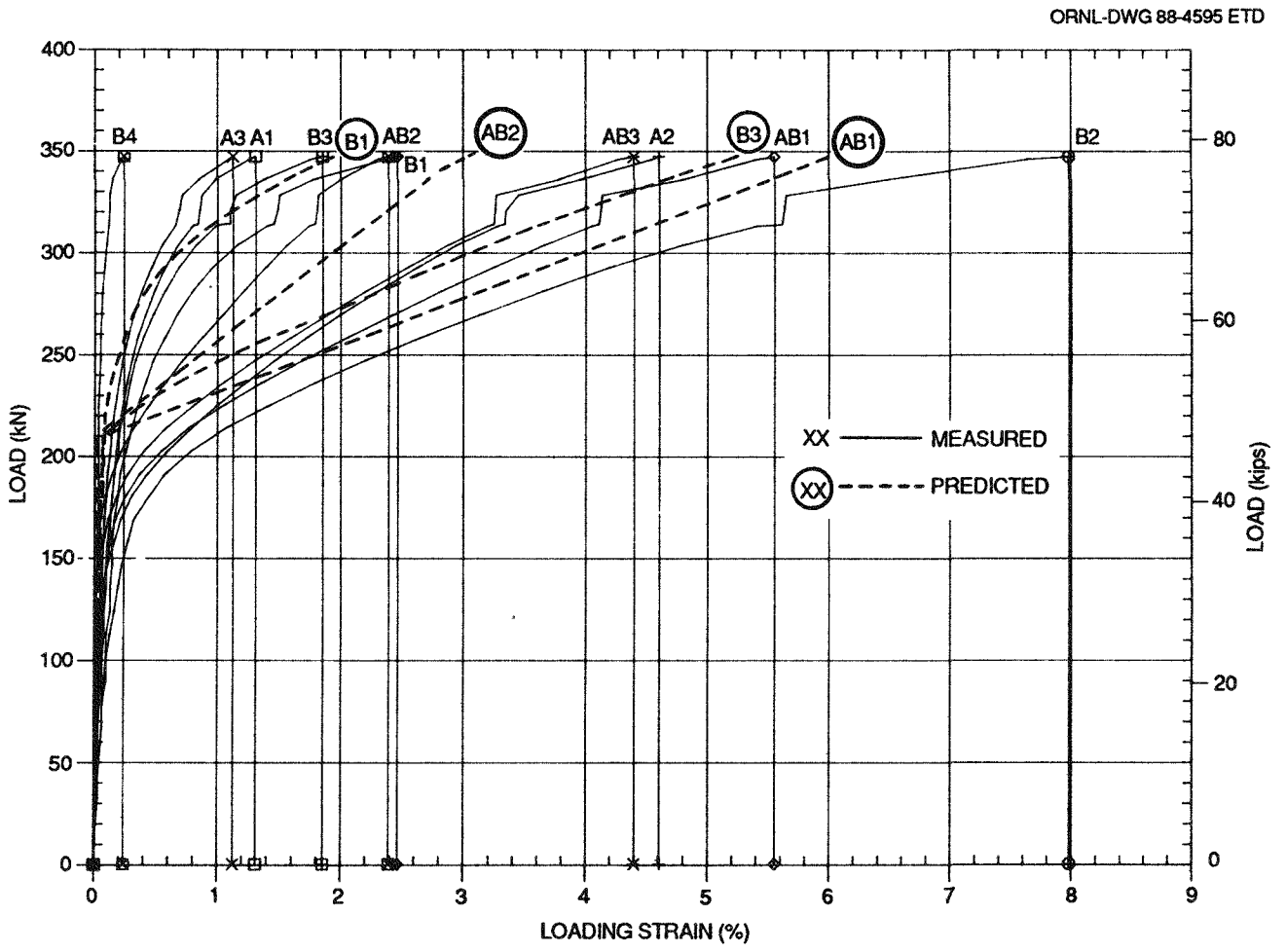


Fig. 50. Comparisons of predicted and measured initial loading strains in various material zones of WCCT-1.

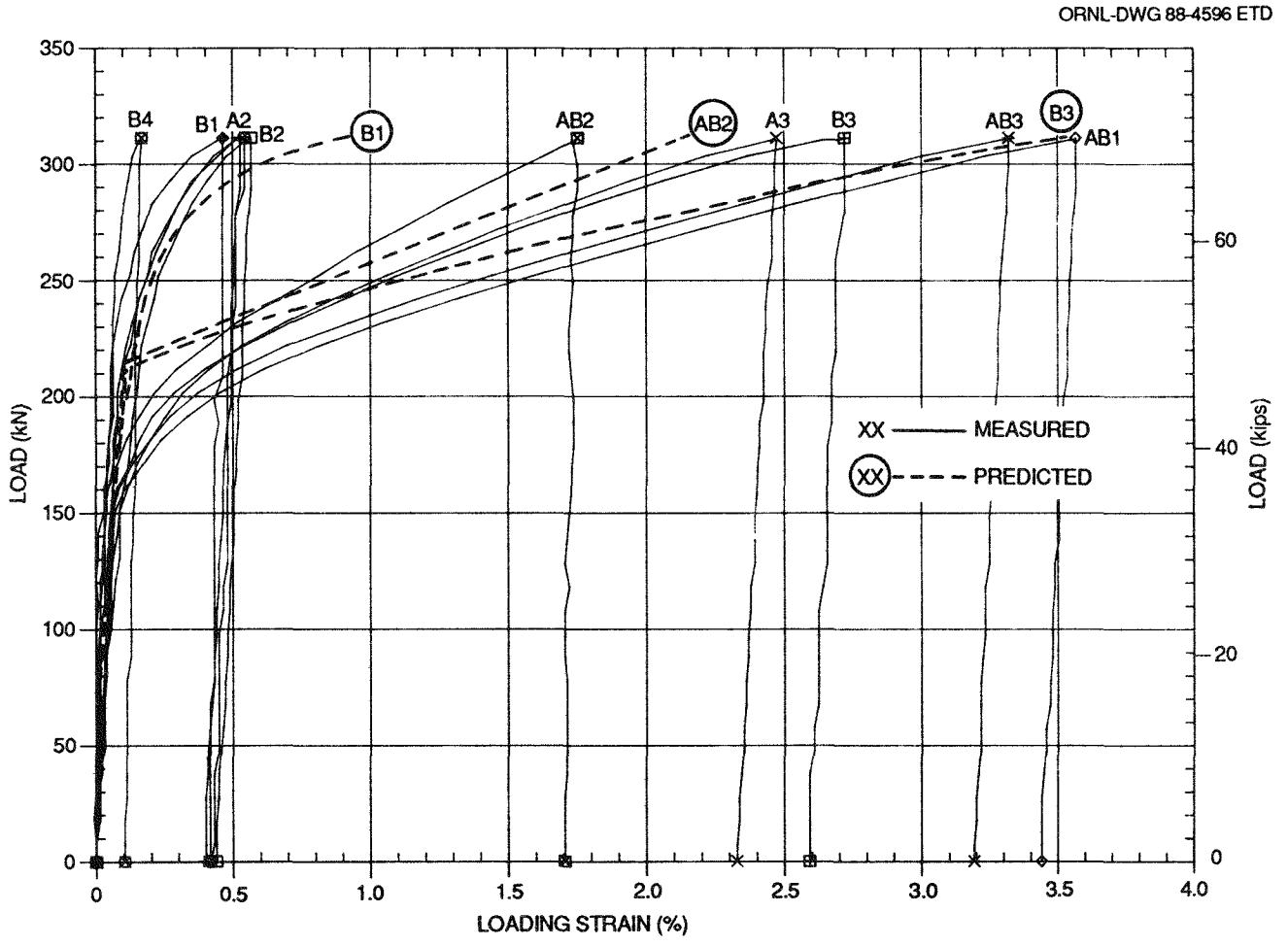


Fig. 51. Comparisons of predicted and measured initial loading strains in various material zones of WCCT-2.

for the various zones are consistent with those obtained from the material properties characterization tests. The analytically predicted strains were, however, consistently somewhat larger than those measured.

Figures 52–54 show the comparisons of predicted and measured creep strains in the weld metal, fusion line, and HAZ, respectively, of the WCCT-1 specimen during the constant load hold periods. The analysis predicted the general trends of the primary and secondary creep strains. Both analysis and test results indicated increased creep strain rates after the overload occurred at 766 h. Overall, however, the comparisons were only fair between the predictions and measured results. The measured results themselves varied from weld to weld. Similar conclusions apply also to the creep strain responses of WCCT-2 as depicted in Figs. 55–57.

## 6.2 Failure Predictions Compared with Test Results

### 6.2.1 Plate specimens

Creep damage was computed from the time fraction approach described in Sect. 4.3.4, and when D = 1 for any zone, the failure criterion for cracking was considered to be met. Visible cracking occurred in the FL/HAZ of the WPCT-5 test article in about 860 h, which compares reasonably well with a prediction of 1300 h from D = 1 being met in the HAZ. In the second plate test (WPCT-7), the analysis predicted failure at 13,000 h, and the specimen had some small cracks at the conclusion of the test (10,400 h) although inspections were not made at regular intervals to determine the exact time that specimen cracking occurred.

It is instructive to examine the computed distributions of stresses and damage across the plate weldment specimens. Upon initial loading, the equivalent stress is much higher in the weld than in the base metal. However, with time the stresses tend toward a more uniform distribution. Table 8 lists both the equivalent stresses and the damage in the various weldment zones of the two plate specimens at the point of computed initial cracking. These results illustrate the interactive effects of the deformation and failure properties of the zones.

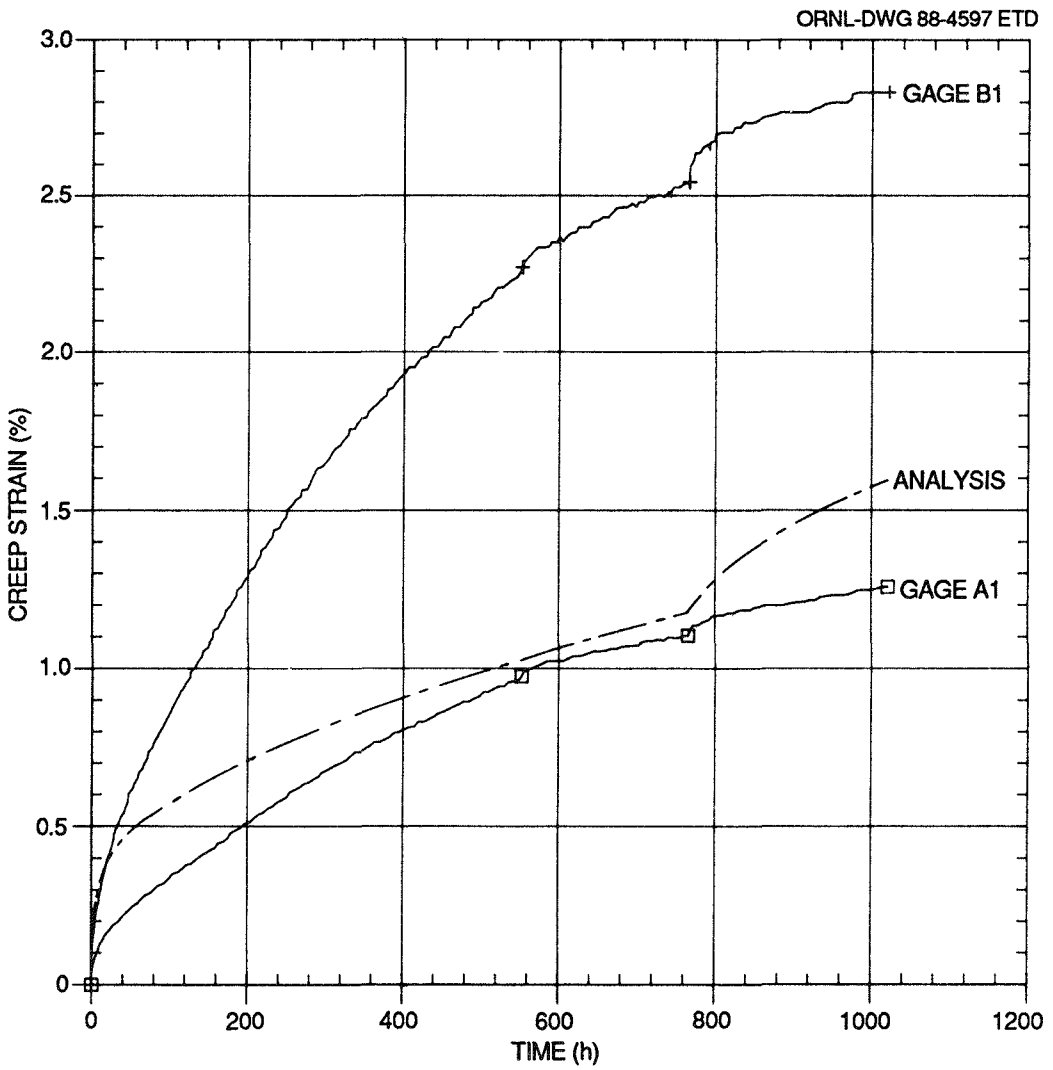


Fig. 52. Comparison of predicted and measured creep strains in the weld metal of WCCT-1.

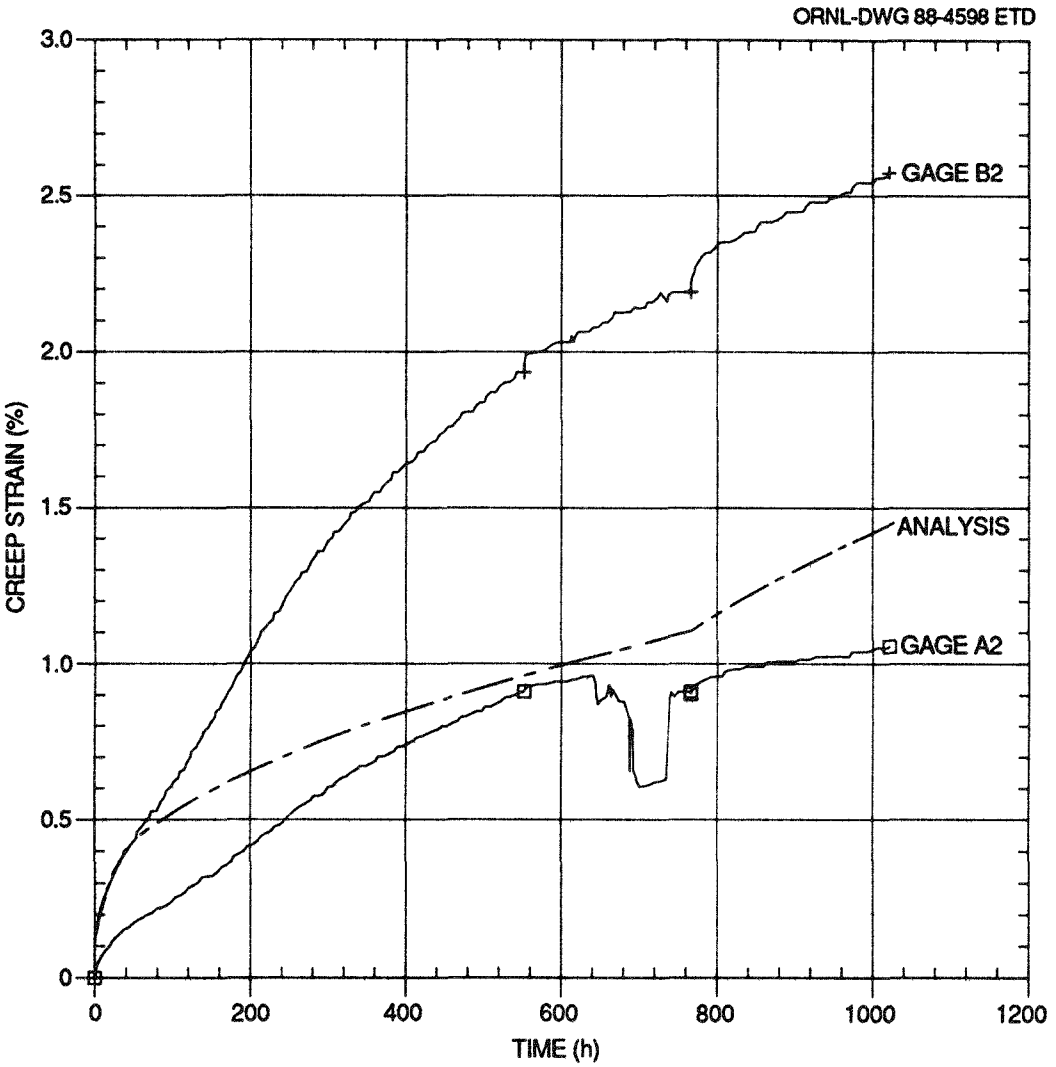


Fig. 53. Comparison of predicted and measured creep strains at the fusion line of WCCT-1.

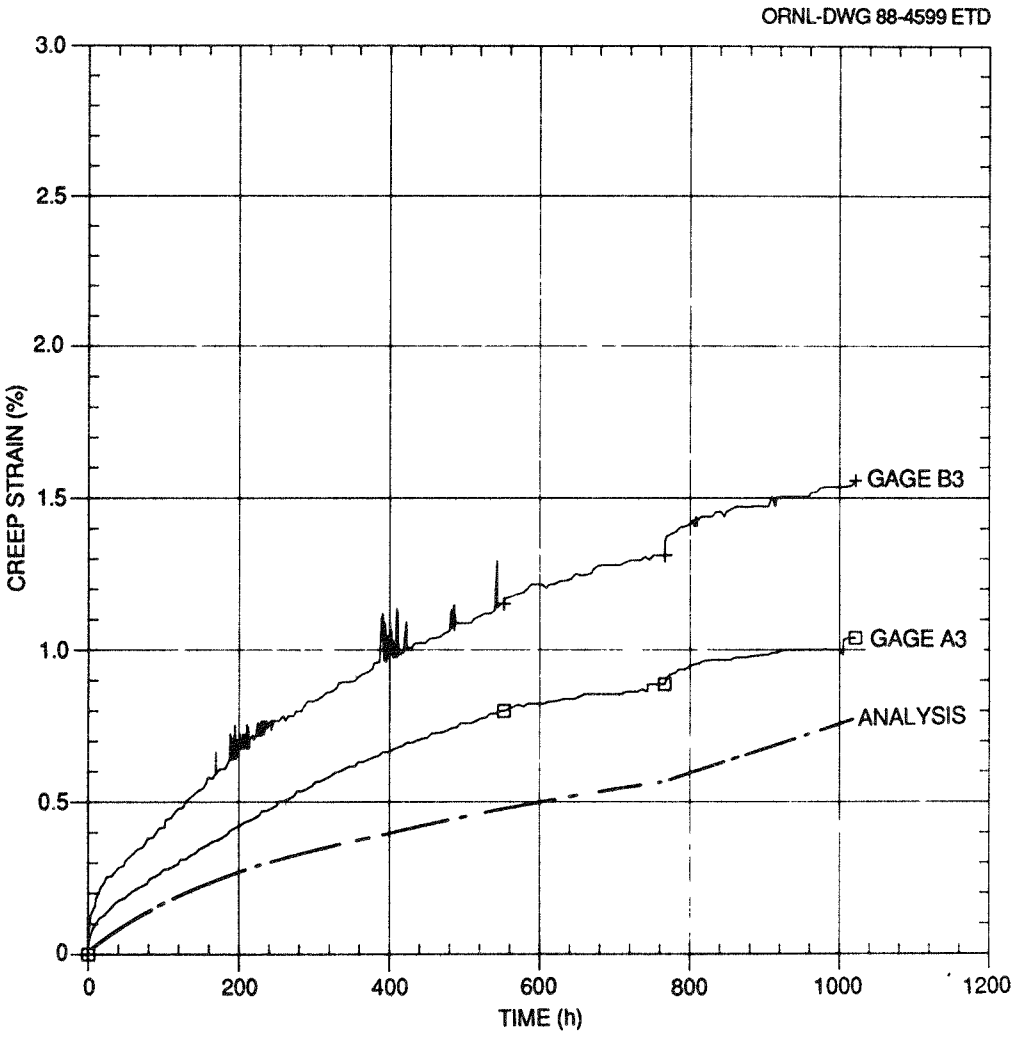


Fig. 54. Comparison of predicted and measured creep strains in the HAZ of WCCT-1.

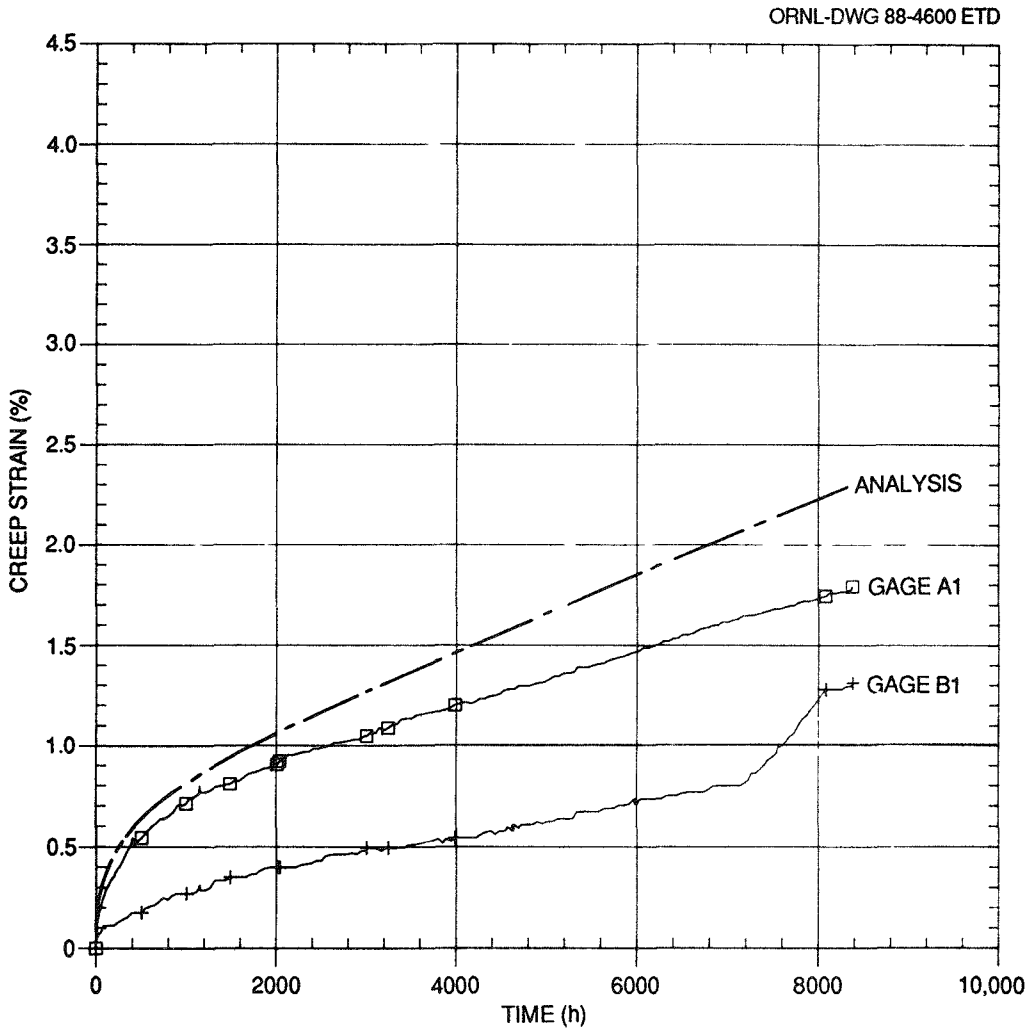


Fig. 55. Comparison of predicted and measured creep strains in the weld metal of WCCT-2.

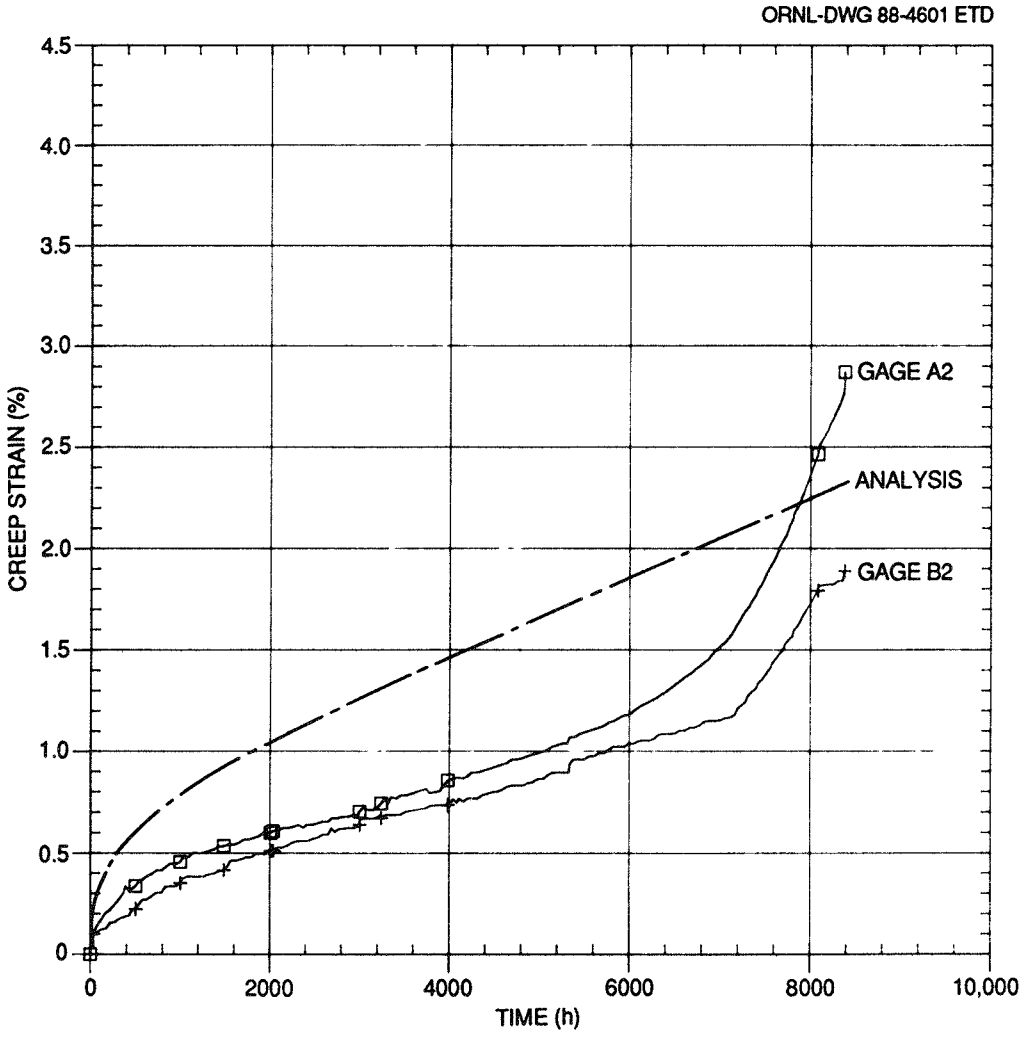


Fig. 56. Comparison of predicted and measured creep strains at the fusion line of WCCT-2.

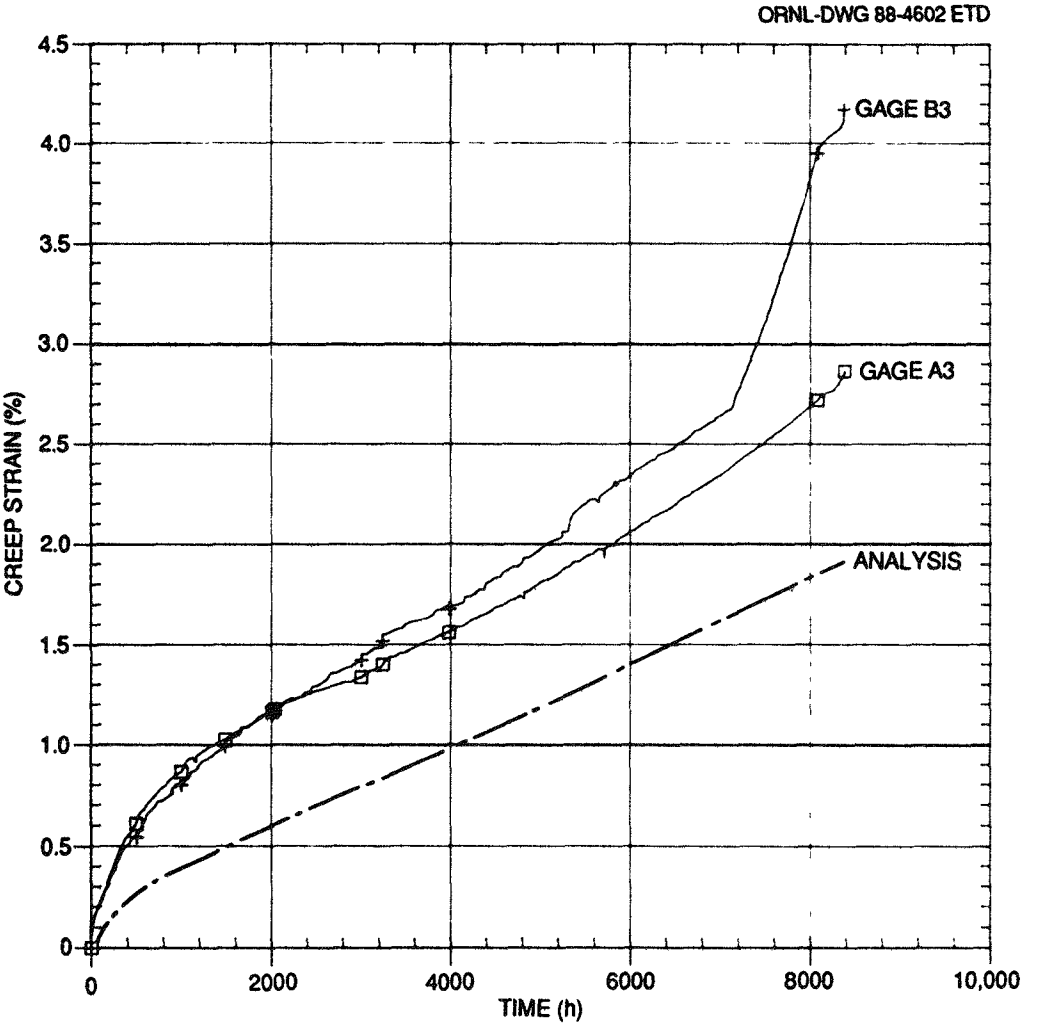


Fig. 57. Comparison of predicted and measured creep strains in the HAZ of WCCT-2.

Table 8. Equivalent stresses and damage levels in welded plate tests at indicated times

| Weldment zone | WPCT-5 (1,300 h) | | WPCT-7 (13,000 h) | |
|---|---|---|---|---|
| | $\sigma_e$ (ksi)[a] | D | $\sigma_e$ (ksi)[a] | D |
| W | 34.6 | 0.80 | 30.7 | 1.0 |
| FL | 36.8 | 0.60 | 31.3 | 0.78 |
| HAZ | 33.8 | 1.0 | 26.5 | 0.72 |
| BM | 30.5 | 0.30 | 20.9 | 0.15 |

[a]1 ksi = 6.895 MPa.

### 6.2.2 Cylinder specimens

In the case of the cylinders, the equivalent stress $\sigma_e$ (see Sect. 4.2) was almost uniform across the various weldment zones and equal to the applied axial stress. As an illustration, the calculated equivalent stresses are tabulated in Table 9 at an arbitrary, but representative, time in each test. Although the fusion line stresses are somewhat higher, as they were in the plates, cracking should be dictated largely by the respective creep-rupture curves.

Table 9. Equivalent stresses at given times in welded cylinder creep tests

| Weldment zone | $\sigma_e$ (ksi)[a] | |
|---|---|---|
| | WCCT-1 at 766 h | WCCT-2 at 8384 h |
| W | 32.9 | 30.0 |
| FL | 34.3 | 31.6 |
| HAZ | 32.0 | 27.8 |
| BM | 32.0 | 28.0 |

[a]1 ksi = 6.895 MPa.

The failure (D = 1) predictions are summarized in Table 10 along with the damage levels in all of the weldment zones at the time of fracture.

Table 10. Predicted failure times, locations, and relative damage in the weldment zones of WCCT-1 and -2

| Weldment zone | WCCT-1 | WCCT-2 |
|---|---|---|
| W | 0.63 | 0.48 |
| FL | 0.72 | 0.67 |
| HAZ | 0.75 | 0.65 |
| BM | 1.0 (1525 h) | 1.0 (5000 h) |

Both specimens actually ruptured in the base metal; the rupture time for WCCT-1 was 1022 h, whereas the time for WCCT-2 was 8384 h. First visible cracking was not monitored in the base metal. However, visible cracking in the HAZs occurred at 776 h for WCCT-1 and at 2015 h for WCCT-2. Overall, the comparisons are thought to be reasonable.

# 7. SUMMARY AND CONCLUSIONS

The latest revision of the *ASME Boiler and Pressure Vessel Code Case N-47* (Ref. 1), which governs the design of elevated-temperature nuclear components, contains explicit creep-rupture and fatigue-strength-reduction factors for weldments. A single but significant life-reduction factor is used for fatigue. A previous ORNL report[7] describes the basis for the fatigue factor and provides experimental validation of that basis. This report focuses on the creep-rupture strength reduction factors, their basis, and further experimental validation.

The Code creep-rupture strength-reduction factors are given as time- and temperature-dependent tables of the ratio of weld metal creep-rupture strength to the corresponding base metal creep-rupture strength. The ratios are used to reduce both the primary stress allowables at weldments and the allowable creep damage in creep-fatigue assessments. Usually the reductions are relatively small, and this finding is consistent with the fact that of the results of some 40 creep-rupture tests found in the literature, none was below the Code expected minimum creep-rupture strengths of the respective base metals. The factors do add some additional design margin at weldments, and in addition, the tables, which are for specific weld filler metals and processes, limit the weld metals and processes that are allowed.

The purpose of the four tests and associated analyses described in this report was to substantiate the logic of the Code factors and to enhance understanding of what leads to early creep-rupture cracking in weldments. The test specimens and loadings were chosen to examine two fundamental situations. In the first, represented by the two axially loaded and axially welded flat plates, the applied stress is parallel to the weld. The axial strain across the weldment must be constant (generalized plane strain) so that the difference in the deformation properties of the various weldment zones (weld metal, fusion line, HAZ, and base metal) results in significantly different stresses in the zones. These differences play a significant role in determining the time and location of failure. The second situation was represented by the axially loaded cylinders with circumferential welds. Here, each zone must carry the

applied stress so that, except for a small interaction, the equivalent stress is constant through the weldment. In this situation, failure time and location is largely governed only by the creep-rupture properties of the various weldment zones.

The base material of the four specimens was 316 stainless steel (reference heat 8092297), and the filler metal was 16-8-2 wire. Either the normal gas tungsten arc process or the hot wire gas tungsten arc process was used to prepare the various weldments. The weldment properties were determined by cutting uniaxial specimens from the various zones of sample weldments. Both stress-strain and creep (including rupture) data were generated for the four weldment zones at 566°C (1050°F), which was the temperature of the four structural weldment tests. The relative values of the measured properties are summarized next.

| | Yield and flow stress | Creep strain | Creep-rupture time* |
|---|---|---|---|
| Lowest | BM | FL | BM |
| ↓ | HAZ | W | HAZ |
| | FL | HAZ | W |
| Highest | W | BM | FL |

An inelastic failure analysis using multiproperty zones was performed for each of the four structural weldment tests, and the predicted deformations and failures were compared with the test observations. The analysis and test results together help to enhance understanding of weldment creep-rupture behavior. Key observations are listed below.

- A grip failure in plate test WPCT-7 resulted in an altered test specimen, thus affecting subsequent results. Likewise, a short-term overload occurred in cylinder test WCCT-1, thus altering subsequent response somewhat.
- The cylinder test WCCT-1 exhibited fairly large weld-to-weld variability, and the relative strain response of some of the weld zones

*The creep-rupture curves cross at a stress level of about 276 MPa (40 ksi). The order shown is for stresses below that level.

was inconsistent with the mechanical properties data. This inconsistency did not exist in the second cylinder test, WCCT-2.

- Taken as a whole, the inelastic loading and creep strains in the weldments were fairly well predicted, particularly for plate test WPCT-5 and cylinder test WCCT-2.
- The predicted time to failure for both plates agreed closely with the observed times to visible (1/32-in.) cracking.
- Cracking in the cylinders was overpredicted by a factor of about 2 (3 or 4 if it is considered that observed initial cracking was in the HAZ). Although larger than for the plates, the differences between measured and predicted lives for the cylinders are not considered to be unreasonable. The safety margin on life in Code Case N-47 is much larger than 3 or 4.
- Overall, the tests and analyses help to confirm our understanding of weldment creep-rupture failures.
- Like the results of the 40 tests from the literature, the results of the four tests reported here support the adequacy of the Code Case N-47 allowables and weld strength-reduction factors for handling weldments.

One last point should be made. This report has addressed creep rupture under constant or step loadings that would be classified as primary in the Code sense. Repeated thermal transient loadings of a welded structure and the adequacy of the Code creep-rupture and fatigue-reduction factors for such loadings have not been addressed. In these cases, which are of prime concern in the design of liquid-metal reactor components, the stresses are cyclic and much more complex. Furthermore, the damage is creep-fatigue rather than creep or fatigue alone.

Thermal ratchetting failure tests of welded pipes have been planned for the ETEC to complete the confirmation of the adequacy of the elevated-temperature weldment design approach. The specimen for one of these tests is a companion to those discussed in this report. A 203.2-mm-diam (8-in.) 316 stainless steel pipe with three circumferential welds will be used. The base material is the reference heat, and the weld metal is the same 16-8-2 material as used in the tests reported herein. Although the

test specimen assembly has been fabricated at ETEC, the test has not been conducted. Its completion will add significantly to the validation of an elevated-temperature design methodology for liquid-metal reactor components.

## REFERENCES


1. Case N-47-26, *Class 1 Components in Elevated Temperature Service, Section III, Division 1*, Cases of ASME Boiler and Pressure Vessel Code, American Society of Mechanical Engineers, New York, February 1987.

2. *The Phenix Nuclear Plant After Three Years of Operation*, Centrale Phenix, Bagnols sur Ceze, France, July 14, 1977.

3. F. Conte, M. Sauvage, and J.-F. Roumailhac, "The Intermediate Heat Exchanger Leak on Phenix Plant and Their Report," pp. 291–96 in *Optimization of Sodium-Cooled Fast Reactors*, proceedings of the International Conference in London, Nov. 28–Dec. 1, 1977, British Nuclear Energy Society, London, 1978.

4. R. R. Matthews and K. J. Henry, "Location and Repair of the DFR Leak," *Nucl. Eng.* 13(149), 840–44 (October 1968).

5. *Safety Evaluation Report Related to the Construction of the Clinch River Breeder Reactor Plant*, NUREG-0968, Vol. 1, U.S. Nuclear Regulatory Commission, March 1983.

6. D. S. Griffin, "Elevated-Temperature Structural Design Evaluation Issues in LMFBR Licensing," *Proceedings of Eighth International Conference on Structural Mechanics in Reactor Technology*, Vol. L, Paper L9/1, Brussels, August 1985.

7. D. G. O'Connor and J. M. Corum, *Design Rule for Fatigue of Welded Joints in Elevated-Temperature Nuclear Components and Its Experimental Confirmation*, ORNL-6333, Martin Marietta Energy Systems, Inc., Oak Ridge Natl. Lab., January 1987.

8. W. J. McAfee and Y. L. Lin, *The Effect of Weld-Metal Properties Variations on the Elevated Temperature Deformation and Failure Behavior of Structural Weldments*, ORNL/TM-7767, Union Carbide Corp. Nuclear Div., Oak Ridge Natl. Lab., November 1981.

9. W. J. McAfee, M. Richardson, and W. K. Sartory, *Creep Deformation and Rupture Behavior of Type 304/308 Stainless Steel Structural Weldments*, ORNL-5265, Union Carbide Corp. Nuclear Div., Oak Ridge Natl. Lab., June 1977.

10. B. R. Dewey, C. R. Brinkman, and K. W. Boling, *Creep and Creep-Rupture Behavior of 2 1/4 Cr-1 Mo/ERNiCr-3 Longitudinal Weldments*, ORNL-5929, Union Carbide Corp. Nuclear Div., Oak Ridge Natl. Lab., February 1983.

11. W. J. McAfee, R. L. Battiste, and R. W. Swindeman, *Elevated Temperature (593°C) Tests and Analyses of Type 304/308-CRE Stainless Steel Plate Weldments*, ORNL/TM-9064, Martin Marietta Energy Systems, Inc., Oak Ridge Natl. Lab., May 1984.

12. M. J. Manjoine, *Creep Rupture Tests of Type 304 Stainless Steel Weldments With Central Axial Welds of Type 308 Stainless Steel at 593°C*, WARD-HT-3045-38, Westinghouse Advanced Reactors Division, May 1979.

13. M. J. Manjoine, *Creep Rupture Tests of Type 304 Stainless Steel Weldments With Central Transverse Welds of Type 308 Stainless Steel at 593°C*, WARD-HT-94000-3, Westinghouse Advanced Reactors Division, September 1979.

14. R. Sandström and B. Ivarsson, "Creep in Butt-Welded Tubes of Cold Worked AISI 316 With Internal Pressure," pp. 223–31 in *Proceedings of Third International Conference on Mechanical Behavior of Materials*, Vol. 2, Cambridge, England, Aug. 20–24, 1979, ed. K. J. Miller and R. F. Smith, Pergamon, Oxford, 1980.

15. M. C. Coleman, J. D. Parker, and D. J. Walters, *The Behavior of Ferritic Weldments in Thick Section 1/2 Cr-1/2 Mo-1/4 V Pipe at Elevated Temperature*, Central Electricity Generating Board Report RD/M/1204R81, CEGB Research Division, Marchwood, England, December 1981.

16. Isao Okane and Koji Osumi, "Creep Rupture Properties of Welded Joints of Type AISI 304 and 316 Austenitic Stainless Steels," *Trans. of National Research Inst. for Metals* (Japan) 14(2), 67–74 (1972).

17. W. K. Sartory et al., *Thermal Ratchetting Test of 2 1/4 Cr-1 Mo Steel to Type 316 Stainless Steel Pipe: Test TTT-3*, ORNL-5330, Union Carbide Corp. Nuclear Div., Oak Ridge Natl. Lab., October 1977.

18. S. D. Snyder and B. C. Leslie, *In-Service Inspection of the Dissolver Tank in Solvent-Refined Coal Plant at Wilsonville, Alabama*, ORNL/TM-6277, Union Carbide Corp. Nuclear Div., Oak Ridge Natl. Lab., April 1978.

19. Y. L. Lin and R. L. Battiste, *Elevated Temperature Test and Analysis of 304 SS/308-CRE Welded Beam (WB-1)*, ORNL/TM-10292, Martin Marietta Energy Systems, Inc., Oak Ridge Natl. Lab., February 1987.

20. NE Standard F 9-5T, *Guidelines and Procedures for Design of Class 1 Elevated Temperature Nuclear System Components*, U.S. DOE, October 1986.

21. R. L. Huddleston and J. R. Ellis, *An Improved Creep-Rupture Strength Criterion Based on Experimental, Multiaxial Data for Type 304 and 316 Stainless Steel and Inconel*, ORNL-5964, Union Carbide Corp. Nuclear Div., Oak Ridge Natl. Lab., September 1983.

22. R. L. Huddleston, "Strength Theory Assessments and Development," pp. 4-27 to 4-39 in *High-Temperature Structural Design Program Semiannual Prog. Rep. Dec. 31, 1983*, ORNL/MSP/1.1-84/1, Union Carbide Corp. Nuclear Div., Oak Ridge Natl. Lab.

23. W. K. Sartory, *PLACRE User's Manual*, ORNL/TM-5626, Union Carbide Corp. Nuclear Div., Oak Ridge Natl. Lab., February 1977.

24. W. K. Sartory, "A Geometrically Nonlinear Version of PLACRE," pp. 104–5 in *High-Temperature Structural Design Program Semiannual Prog. Rep. June 30, 1981*, ORNL-5794, Union Carbide Corp. Nuclear Div., Oak Ridge Natl. Lab.

25. J. A. Clinard and W. K. Sartory, "Analysis of a Thick-Wall Pipe (Reference Problem)," pp. 4-109 to 4-114 in *High Temperature Structural Design Technology Program Semiannual Prog. Rep. for Period Ending June 30, 1983*, ORNL/MSP/1.1-83/3, Union Carbide Corp. Nuclear Div., Oak Ridge Natl. Lab.

26. W. K. Sartory, *Revised Analysis of the Transition Joint Life Test*, ORNL/TM-9211, Martin Marietta Energy Systems, Inc., Oak Ridge Natl. Lab., July 1984.

ORNL-6500
Dist. Category UC-538T
and 540T

## Internal Distribution

1. R. L. Battiste
2. J. J. Blass
3. C. R. Brinkman
4. S.-J. Chang
5. J. A. Clinard
6-10. J. M. Corum
11. J. A. Getsi
12. R. C. Gwaltney
13-14. W. R. Hendrich
15. R. L. Huddleston
16. J. E. Jones Jr.
17-18. Y. L. Lin
19. K. C. Liu
20. D. G. O'Connor
21. C. E. Pugh
22. P. L. Rittenhouse
23. M. B. Ruggles
24. W. K. Sartory
25. G. M. Slaughter
26-27. R. W. Swindeman
28. H. E. Trammell
29. G. T. Yahr
30. ORNL Patent Section
31. Central Research Library
32. Document Reference Section
33-34. Laboratory Records Department
35. Laboratory Records (RC)

## External Distribution

36-37. Director, Office of Technology Support Programs, Department of Energy, Washington, DC 20545

38. Office of Assistant Manager for Energy Research and Development, DOE, ORO, Oak Ridge, TN 37831

39-65. Given distribution as shown in DOE/TIC-4500 under categories UC-538 (LMFBR: Structural Materials and Design Engineering); UC-540 (LMFBR: Components)